Universiteit Antwerpen

This item is the archived peer-reviewed author-version of:

Multiscale modeling of plasma–surface interaction : general picture and a case study of Si and SiO_2 etching by fluorocarbon-based plasmas

Reference:
Vanraes Patrick, Parayil Venugopalan Syam, Bogaerts Annemie.- Multiscale modeling of plasma–surface interaction : general picture and a case study of Si and SiO_2 etching by fluorocarbon-based plasmas
Applied physics reviews / American Institute of Physics - ISSN 1931-9401 - 8:4(2021), 041305
Full text (Publisher's DOI): https://doi.org/10.1063/5.0058904
To cite this reference: https://hdl.handle.net/10067/1832870151162165141

uantwerpen.be
Institutional repository IRUA

Multiscale modeling of plasma-surface interaction – general picture and a case study of Si and SiO_2 etching by fluorocarbon-based plasmas

Patrick Vanraes[1], Syam Parayil Venugopalan[2], Annemie Bogaerts[1]

[1]*PLASMANT, Department of Chemistry, University of Antwerp, Universiteitsplein 1, 2610 Wilrijk-Antwerp, Belgium*

[2]*ASML, De Run 6665, 5504 DT Veldhoven, Netherlands*

Abstract

The physics and chemistry of plasma-surface interaction is a broad domain relevant to various applications and several natural processes, including plasma etching for microelectronics fabrication, plasma deposition, surface functionalization, nanomaterial synthesis, fusion reactors, and some astrophysical and meteorological phenomena. Due to their complex nature, each of these processes are generally investigated in separate subdomains, which are considered to have their own theoretical, modeling and experimental challenges. In this review, however, we want to emphasize the overarching nature of plasma-surface interaction physics and chemistry, by focusing on the general strategy for its computational simulation. In the first half of the review, we provide a menu card with standard and less standardized computational methods to be used for the multiscale modeling of the underlying processes. In the second half, we illustrate the benefits and potential of the multiscale modeling strategy with a case study of Si and SiO_2 etching by fluorocarbon plasmas, and identify the gaps in knowledge still present on this intensely investigated plasma-material combination, both on a qualitative and quantitative level. Remarkably, the dominant etching mechanisms remain the least understood. The resulting new insights are of general relevance, for all plasmas and materials, including their various applications. We therefore hope to motivate computational and experimental scientists and engineers to collaborate more intensely on filling the existing gaps in knowledge. In this way, we expect that research will overcome a bottleneck stage in the development and optimization of multiscale models, and thus the fundamental understanding of plasma-surface interaction.

TABLE OF CONTENTS

1. INTRODUCTION
2. PLASMA-SURFACE INTERACTION PHYSICS – AN OVERARCHING DOMAIN WHERE SUPERFICIALITY MATTERS
3. GENERAL SIMULATION STRATEGY – EXPERIMENTING *IN-SILICO*
    3.1 Multiscale modeling – coupling classical and quantum matter
    3.2 Four classes of standard simulation methods – choose your weapons wisely
        3.2.1 Class I: time-independent atomistic models – it's a small and steady world
        3.2.2 Class II: time-dependent atomistic models – one small step for an atom
        3.2.3 Class III: mesoscopic models – computational compromise
        3.2.4 Class IV: macroscopic models – the big picture
    3.3 Unconventional simulation methods – a tool box for out-of-the-box thinking
        3.3.1 Less explored methods from the four classes – the need for computational

wanderlust
3.3.2 Application-specific methods – specialize in the impossible
3.3.3 Machine learning – brainstorming by artificial intelligence
3.3.4 Plasma sheath modeling – matter's aura explained
3.4 Multiscale measuring – because nature is still the best simulation tool
4. PLASMA ETCHING – FROM SCRATCHING THE SURFACE TO GOING IN DEPTH
4.1 The multiscale plasma etching model – one example to represent them all
4.1.1 The need for a bottom-up approach – message in a bottleneck
4.1.2 Hybrid Plasma Equipment Model – example of a hybrid macroscale method
4.1.3 Plasma sheath module – example of a semi-analytical sheath method
4.1.4 Surface kinetics module – example of a deterministic description
4.1.5 Monte Carlo Feature Profile Model – example of a kinetic Monte Carlo method
4.1.6 Experimental benchmarking of the working principle – examples of multiscale measuring
4.1.7 Reactor geometry and operating conditions – example of a case study
4.2 How to implement the surface processes – example of atomistic modeling and measuring data
4.2.1 Elementary plasma-surface mechanisms – simplicity is the ultimate sophistication
4.2.2 Design of the surface chemistry set – a mosaic of quantum data
4.3 Benchmarking the simulation model – bringing uncertainties to the surface
5. SUMMARY AND FUTURE OUTLOOK – LOOKING TOWARDS, BENEATH AND BEYOND THE SURFACE

1. INTRODUCTION

Plasma commonly contacts a material surface in various astrophysical systems and laboratory setups. Therefore, the study of plasma-surface interaction is as old as plasma physics itself. Research on this topic is largely driven by various applications aiming at synthesizing or modifying a surface, a material or a contacting gas, or, on the contrary, striving to prevent plasma reactor wall erosion. Next to that, it is important for a detailed understanding of plasma-based chemical analysis and several natural phenomena. Accordingly, a large number of reviews has been published on the interaction of plasmas with materials, usually focused on a specific application. Most of them do not deal with the elementary mechanisms at the material surface, or only discuss them briefly. That is, any discussions in scientific literature on the fundamental processes at the plasma-material interface either remain qualitative in nature, or only consider a limited number of individual interactions between a specific plasma species and the surface. A more profound and detailed description on the fundamentals can be found in a few interesting and recommended review papers [1-12], often with respect to the modeling and simulation of the plasma-surface interactions. Also these papers are generally restricted in their scope, e.g. to specific plasma species, surface materials, applications or computational techniques. In other words, the fundamental study of plasma-surface interaction remains largely scattered across the separate experimental, computational and literature investigations, published in the diverse sub-disciplines of plasma physics. On the one side, this makes a tutorial overview desirable on the most recommended investigation strategy for plasma-surface interactions across all these sub-disciplines. On the other side, it underlines the need for a comprehensive quantitative assessment of the underlying interaction mechanisms.

The present review addresses these issues with a threefold purpose: (i) to provoke a higher awareness of the high potential and wide applicability of multiscale modeling as an overarching strategy in the

study of plasma-surface interactions (Section 2), (ii) to provide a comprehensive reference work and tutorial on the connectable simulation methods, for scientists and engineers regardless of their experience level (Section 3), and (iii) to demonstrate the quantitative implementation of individual particle-surface interactions in a multiscale model, by means of a plasma etching case study, in order to reveal the current knowledge, as well as the remaining knowledge gaps (Section 4). By zooming in on a plasma etching example with original computational research benchmarked with experiments, the latter part is more technically oriented than the former two, for readers who wish to dive deeper into the details of individual particle-surface interactions. Plasma etching lends itself for this purpose in a straightforward manner, due to the large amount of quantitative data available in literature on specific interactions of the corresponding plasma species with the substrate to be etched. However, as we will demonstrate, several gaps in fundamental knowledge also prevail in this well-established technology.

Although the plasma etching example is especially interesting for experts working on microelectronics manufacturing, it also serves as a practical guide for researchers dealing with other applications where individual particle-surface interactions play a crucial role, such as surface functionalization, nanomaterial synthesis, plasma catalysis and fusion reactors. As we will highlight in Section 2, this includes research on certain meteorological and space plasmas as well. Readers whose interest lies outside the atomistic details are perhaps better served by skipping through Section 4. This may be the case for researchers who limit their study of the plasma-material interface down to effects on the mesoscale, e.g. surface amorphization, material restructuring, pore formation, phase transitions and associated surface deformations. However, atomistic mechanisms can be relevant to any study on plasma-surface interaction, so we want to motivate researchers to familiarize themselves at least on a high level with the simulation methods used to describe the atomistic scale, as further discussed in Section 3. We have structured the present review in a tutorial-like fashion, where the reader is free to choose which parts to focus on and which reference works to examine for a more specialized investigation.

This review thus starts with two general main Sections 2 and 3, followed by a more specific and applied Section 4 on the plasma etching example. In Section 2, we present plasma-surface interaction physics as an overarching research domain, by mapping its relevance to several natural phenomena, laboratory processes and a multitude of plasma applications. Section 3 presents a general simulation strategy applicable to each of these processes, in order to gain a deeper fundamental understanding and to optimize the related applications. This strategy relies on multiscale modeling, which couples the effects on the atomic scale, mesoscale and macroscale (Section 3.1), by means of various standard simulation methods that we will distinguish into four classes (Section 3.2). Afterwards, we discuss the importance of less conventional methods (Section 3.3) and how experiments can contribute to this simulation strategy (Section 3.4). In Section 4, we present a case study based on original research for Si and SiO_2 etching by fluorocarbon-based plasmas. After introducing the model developed by the Kushner group and used for this case study (Section 4.1), we scrutinize the basic surface processes in Section 4.2.1. Next, we demonstrate how a surface interaction set can be designed with a bottom-up approach by means of quantitative literature data on the individual interactions of each plasma species for every surface group in Section 4.2.2. In this design process, we had to make several strategic choices and assumptions on the surface mechanisms, which are discussed in detail.

Our design methodology corresponds to a bottom-up approach. It stands in contrast with the conventional top-down approach, where only the supposedly main interactions are included into the surface interaction set, and benchmarked directly by trial-and-error. The latter procedure usually relies on experimental data of the overall plasma treatment process, rather than on the individual

interactions of plasma species with the material. Although the bottom-up approach is more time-consuming and restricted by the available data on individual species interactions, it produces surface interaction sets of a superior quality and transparency. To our knowledge, the bottom-up benchmarked set presented in this review is the first of its kind, underlining the novelty of our work. After its construction, we reveal how the set allows to study the influence of the distinct surface interaction mechanisms on the overall treatment process, and a straightforward top-down benchmarking of the computational model (Section 4.3). In Section 5, we conclude the review with a summary of the obtained insights and recommendations for future experimental and computational investigations.

2. PLASMA-SURFACE INTERACTION PHYSICS – AN OVERARCHING DOMAIN WHERE SUPERFICIALITY MATTERS

Before elaborating on the simulation strategy for plasma-surface interaction, it is useful to chart the various natural phenomena, laboratory processes and applications where this type of interaction plays a decisive role. This is the purpose of the current section. Although it does not lie in our ambition to list all of the possible examples in a fully-comprehensive manner, we will attempt to provide a concise overview, evidencing the overarching character of plasma-surface interaction physics. All research in this overarching domain can benefit from the multiscale modeling strategy, due to the distinct time and length scales of the involved physical and chemical processes. However, the extent to which atomistic and even mesoscale mechanisms are implemented in a multiscale model largely depends on the desired level of accuracy and, of course, the knowledge available on these processes.

In astrophysics, the plasma state of matter is ubiquitous, appearing as, for instance, stars like the Sun, solar corona and solar wind, accretion discs, the Io-Jupiter flux tube and planetary lightning, as well as the interplanetary, interstellar and intergalactic media, and the interstellar nebulae. Plasma-surface interaction is realized when these plasmas come in contact with a solid body, such as a cosmic dust particle, comet, meteoroid, asteroid, moon or planet. Comets, for instance, can interact with solar wind and, when approaching close enough towards the Sun, with solar corona [13]. Likewise, solar wind also directly interacts with asteroids or planets in absence of an atmosphere and intrinsic magnetic field. The best-known example is the interplay between the solar wind and the Moon [14, 15]. Also in the direct surroundings of the Earth, several kinds of natural plasmas exist, such as the magnetosphere, plasmasphere, ionosphere and the polar auroras. In all of these atmospheric regions, dust particles are present, mainly originating from extraterrestrial matter [16, 17]. Additionally, objects from space typically enter the atmosphere with a hypersonic speed, generating a plasma on their own through the friction with the surrounding air [18, 19]. Closer to the surface of the Earth, electrical discharges remain a relevant topic for meteorologists, with lightning as a famous example, but also various forms of transient luminous events (TLEs) [20, 21]. Aerosols consisting of dust particles or water droplets often play a crucial role in the appearance of these discharges. All these phenomena therefore give rise to certain forms of plasma-surface interaction. Accordingly, their study forms an integral part of meteorology and astrophysics, in the quest to obtain a solid understanding of the weather and the universe, applicable to space travel in particular.

In the laboratory and industrial applications, plasma-surface interaction often plays a crucial role, either beneficial to the desired effect or counteracting it. As an illustration of the latter, the contact between the plasma and the reactor wall poses one of the main theoretical and engineering challenges in nuclear fusion [2, 4, 22, 23]. From a practical perspective, the detrimental wall erosion is even expected to remain such a bottleneck in the final application of fusion reactors that liquid walls

are currently considered as an attractive alternative [24, 25]. This brings us to plasma-liquid interaction, another subdomain to be included in the field of plasma-surface interaction physics, with applications ranging from water treatment, analytical chemistry, nanomaterial and chemical synthesis, to the currently heavily investigated areas of plasma agriculture and plasma medicine [26-30]. As should be noted in this context, laser-matter interaction also often involves the generation of a gaseous plasma in contact with the material, with or without a phase transition into liquid taking place [31].

Plasma-surface interaction can lead to curious effects, many of which are universal in nature and common to all types of plasma-surface interaction. Examples of such common surface effects are plasma-induced etching, deposition, functionalization and heterogeneous chemistry in general, as well as the formation of an electrical double layer, called the plasma sheath. Various applications have been based on these mechanisms. They are therefore sometimes subdivided into four types of applications: plasma etching [10-12, 32], plasma deposition [10, 11, 33], plasma functionalization [34, 35] and plasma catalysis [36, 37]. The former three have the purpose to modify the surface, while the latter is overall meant to transform the gas. Regardless of this subdivision, all four elementary surface processes are often relevant to an application. A fundamental insight into them is therefore helpful across the entire discipline dealing with plasma-surface interaction.

Microelectronics fabrication is one of the interesting applications that includes each of the aforementioned surface mechanisms [10-12]. This especially counts for plasma etching in a polymerizing chemistry, where deposition processes and the interplay between neutral species and the surface compete with physical sputtering and ion-induced etching reactions. For this reason, we will present simulations on SiO_2 etching with CHF_3/Ar plasma in the second half of this review, i.e. Section 4, as a representative case study for the multiscale modeling of plasma-surface interaction. Note that this process does not entail certain mesoscale and macroscale effects crucial to some other plasma-surface applications or phenomena, such as extreme heat fluxes onto the surface, resulting in melting or other types of phase transitions. Such differences may be expected, in particular relative to high-temperature plasmas. In general, these effects may be considered supplementary to the heterogeneous surface chemistry, which is a phenomenon common to all cases of plasma-surface interaction. However, their relative importance varies as a function of the plasma and material properties. For instance, in situations where melting and hydrodynamics dominate at the plasma-material interface, the surface chemistry might only play a minor role. Likewise, when mass transport into the plasma mainly results from evaporation or boiling, considering sputtering effects can be superfluous. For studies involving such conditions, individual particle-surface interactions may be disregarded to a good approximation, making the insights and analysis from Section 4 less applicable.

Even so, we want to emphasize that this relative importance of surface mechanisms rather depends on the specific plasma and material parameters than on the research domain. For example, individual interactions between a plasma species and a surface group can play a central role in certain meteorological and space plasmas. A clear illustration is given by the interplay between the lunar surface and solar wind, which produces an emitted particle flux by Moon material sputtering [15, 38-40] and neutralized solar wind backscattering [38, 41, 42]. By measuring the emitted particles, astronomers can obtain valuable information on the solar wind and the Moon surface. This methodology was put into practice in India's SARA experiment [15, 38, 41-44], and in NASA's Interstellar Boundary Explorer (IBEX) [44-46]. The particle fluxes emitted from a crater bottom on the Moon as compared to a crater wall depend on the energy and angular distributions of the incident solar wind particles, which are regulated on their turn by the plasma sheath. Since this process strongly resembles the one at a wafer surface in a plasma etching reactor, the insights obtained in Section 4

are directly applicable to these space experiments. Similarly, the contact between atmospheric plasma and meteoric smoke involves a collection of species-surface interactions interesting for various purposes, including cosmochemistry and observational spectroscopy [16]. We therefore believe that the case study of Section 4 can provide insights helpful to all subdomains of plasma physics, but its relevance will largely depend on how big of a role the surface chemistry plays in the considered plasma-material interaction. The reader is accordingly invited to determine this level of relevance for each research topic of interest. In contrast, multiscale modeling forms the core of the general simulation strategy in the overarching discipline of plasma-surface interaction physics, regardless of the plasma and material features. This will be the topic of the first half of this review.

3. GENERAL SIMULATION STRATEGY – EXPERIMENTING *IN-SILICO*

3.1 Multiscale modeling – coupling classical and quantum matter

Where Section 2 gave an overview of the various forms of plasma-surface interaction in nature and in applications, this section presents a general strategy to simulate these processes up to a fundamental level by computational means. It allows to obtain models with a stronger predictive power for the natural phenomena, and to optimize the applications in a straightforward manner. In Section 4, we will illustrate how this strategy can be put into practice, as well as which major obstacles still remain. Although this illustration focuses on the example of plasma etching, the underlying reasoning and its consequences are relevant across all applications.

For now, the comprehensive modeling of plasma-surface interaction on a fundamental level has largely been avoided, due to its complex composite character. It namely involves a multitude of physical and chemical processes on different time and length scales, in a strongly heterogeneous system, possibly far from equilibrium. Next to that, these processes are intricately intertwined in a network of synergies and counteractions. More specifically, each incident plasma particle can modify the surface and the plasma, which in turn determines the subsequent individual interactions. For all of these reasons, plasma-surface interaction cannot be described with a single standard simulation method. As well-known, the most accurate simulation tools today are very computationally demanding, while the faster procedures lack in accuracy. Therefore, a multiscale modeling approach has been proposed as a suitable compromise. This strategy is not new, as numerous of such models have already been developed and applied for different plasma processes [47-54]. Additionally, multiscale modeling of plasma-surface interaction has been discussed on a general level in the mini-review by Schneider and the reviews by Nordlund et al., Neyts and Bogaerts, Marian et al. and Bonitz et al. [1, 2, 4, 37, 55]. In the current section, we summarize this approach.

Most commonly, the standard simulation methods are classified according to the considered physical time and length scales. Figure 1 maps the approximate spatio-temporal scales accessible by several individual computational techniques. As a general trend, methods with a high spatial resolution are often restricted to small time intervals, and a high temporal resolution is at the expense of the simulation space size. Moreover, they cannot easily take into account the overall influence of the plasma medium and synergetic effects of successive impacts, without the prior knowledge of the plasma parameters and surface conditions. On the other hand, standard techniques that access the larger time and length scales lack the accuracy required for the simulation of fast microscopic effects. They allow to treat surface processes through phenomenological parameters, such as sticking coefficients, etch rates, secondary electron emission coefficients and energy dissipation time

constants. However, this requires fundamental knowledge on these processes that is *a priori* unknown.

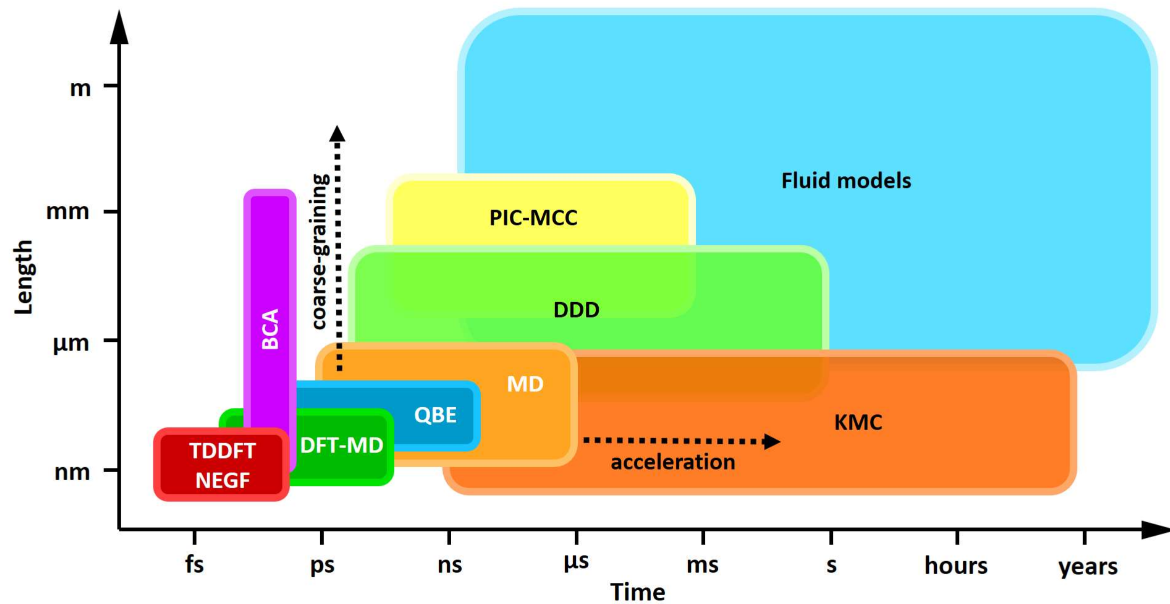

Figure 1. Approximate length and time scales accessible with some of the most common material simulation methods for plasma-surface interaction, in natural processes or applications. The abbreviations stand for time dependent density functional theory (TDDFT), non-equilibrium Green functions (NEGF), DFT- or Born-Oppenheimer MD (DFT-MD), quantum Boltzmann equation (QBE), classical molecular dynamics (MD), particle-in-cell simulations with Monte Carlo collisions (PIC-MCC) and binary-collision approximation (BCA). Adapted by permission from Springer Nature: Frontiers of Chemical Science and Engineering © 2019 from Front. Chem. Sci. Eng. 13, 201 (2019) [1] and adapted with permission of IOP Publishing, Ltd, from J. Phys. D Appl. Phys. 47, 224018 (2014) [4]; permission conveyed through Copyright Clearance Center, Inc.

This poses a problem for the description of plasma-surface interaction, which inherently forms a multiscale process. Laboratory and industrial plasmas, for instance, often have dimensions ranging in the order of 1 mm to 1 m. In the reactor, the plasma sheath thickness at a material surface often lies in the order of 0.1 mm. The surface under treatment can have a roughness spanning over the orders of magnitude of 10^{-8} to 10^{-4} m. In contrast, the isolated interaction of a plasma particle with the surface should be considered at the scale of 10^{-10} to 10^{-8} m. As such, a multiscale modeling approach covering these distinct dimensions appears the most designated strategy. Three standard simulation approaches can be distinguished, according to the considered length scales [37, 56-59]:

- Atomistic models, including density functional theory (DFT) and molecular dynamics (MD), provide detailed insight into individual particle-surface reactions.
- Mesoscale models, such as kinetic Monte Carlo (KMC), trade the computationally expensive atom-based material structure and dynamics for a faster coarse-grained description.
- Macroscale models abandon the coarse-grained details for a continuum mechanical representation of the system. For the sake of convenience, we will also consider Monte Carlo methods limited to the plasma zone as a member of this group.

In principle, this classification should be regarded on the level of methodology, rather than strictly in terms of length scales. Continuum and coarse-grained models may namely also be designed with a mesoscopic and an atomic accuracy, respectively. Reversely, some atomistic methods like classical MD and the binary-collision approximation (BCA) are computationally cheap enough to enable simulations in the mesoscale, illustrating that a certain overlap exists in terms of spatial dimensions. Note that such techniques are sometimes also classified in literature as mesoscale models (see e.g. [1]). However, the above distinction based on atoms, coarse graining and continuum mechanics represents a strong tendency found throughout numerous simulation studies nowadays. We will therefore adopt its terminology for the further discussion.

As should be emphasized, the aforementioned standard methods have a universal character, in the sense that they apply to various surface materials and a wide range of plasma conditions. Their hierarchic combination into a multiscale model has been applied and reviewed for both low-temperature and high-temperature plasmas in contact with diverse materials for miscellaneous purposes, such as plasma etching [47], plasma catalysis [37], plasma medicine [60] and nuclear fusion [2, 4]. This underlines the overarching nature of plasma-surface interaction physics as an individual scientific domain. In this regard, an interesting perspective has been given in the review by Bonitz et al., as illustrated in Figure 2 [1]. According to this perspective, the standard modeling methods can be categorized in three groups corresponding to the main spatial simulation regions:

- The bulk solid is governed by quantum effects due to the high atom and electron densities. To a good approximation, this region resides in internal thermodynamic equilibrium. Consequently, its properties like binding energies and the electronic band structure can be obtained with computational techniques applicable to the material in the ground state or at a finite temperature, as listed in the red box in Figure 2. Similarly, the features of an unperturbed surface can also be calculated, using these methodologies.
- The plasma-solid interface, however, acts as a system out of equilibrium, containing transient excitations of a vibrational or electronic nature. For this reason, time-dependent simulation methods are required, such as the ones presented in the central box of Figure 2.
- The plasma bulk and sheath present a largely classical behavior with relatively low species densities. This allows neglecting the wave character of electrons, photons and excited species as a useful approximation. Therefore, this region is most easily described with macroscale models, in agreement with the blue box in Figure 2.

This classification coincides to a certain degree with the aforementioned ranking based on length scales, although Bonitz et al. recommend both mesoscale and atomistic models for the plasma-solid interface.

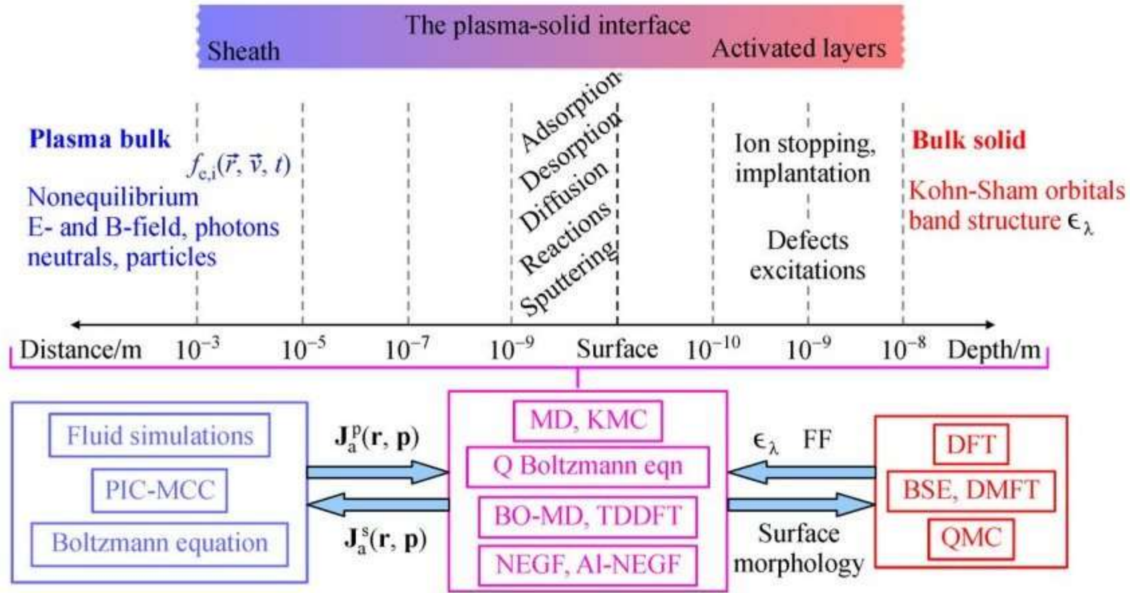

Figure 2. Classification of the standard simulation methods according to the spatial region they describe in plasma-material interaction. Macroscale fluid and kinetic methods (left blue box) mainly apply to the plasma bulk. Mesoscale and non-adiabatic (time-dependent) atomistic methods (central pink box) are feasible to simulate the non-equilibrium surface processes. Time-independent atomistic methods (right red box) provide important information on the bulk solid. The exchange of input and output between the various models is explained in the text. The abbreviations and explanation of the various methods are given in Section 3.2. Reprinted by permission from Springer Nature: Frontiers of Chemical Science and Engineering © 2019 from Front. Chem. Sci. Eng. 13, 201 (2019) [1].

The models in the three regions can then be coupled to one another in a multiscale arrangement by exchanging simulation input and output across the different scales. On the one hand, the macroscale plasma models enable to calculate energy and angular distributions and the fluxes $\mathbf{J}_a^p(\mathbf{r},\mathbf{p})$ of the plasma species incident on the surface, which form useful input data for the interfacial models (see Figure 2). Reversely, the interfacial models reveal the characteristics of the species emitted from the surface during the interaction, such as their fluxes $\mathbf{J}_a^s(\mathbf{r},\mathbf{p})$, which can be included as input for the macroscopic models [1]. With a similar feedback loop, several other effects may be studied, such as electric field enhancement, hot spot formation, micro-discharge generation in pores and variations in the plasma type, e.g. in the case of plasma catalysis [37]. On the other hand, the atomistic equilibrium models for the solid bulk and surface provide information on the material properties, such as the band structure ϵ_λ and reactive force fields (FF), which translates to fundamental parameters for the time-dependent interfacial and plasma models (see Figure 2) [1]. The interfacial models, on their turn, produce surface data useful for the time-independent atomistic methods. Several other feedback loops can be thought of, e.g. between two time-independent solid methods or between time-dependent atomistic and mesoscale interfacial models. In this manner, atomistic methods form an indispensable data source of surface reaction probabilities (including adsorption, desorption, sputtering and photon-induced effects), as well as modified surface properties, like surface group replacement and changes in the work function [37]. For a steady state process, the simulations may be performed separately in time. With strongly changing conditions, however, the different models may need to update each other with their output during the simulation.

3.2 Four classes of standard simulation methods – choose your weapons wisely

Combining the aforementioned length-scale-based and spatial-region-based classifications, we may distinguish four classes of standard simulation methods in the multiscale strategy:

I. time-independent atomistic models for the solid material;
II. time-dependent atomistic models for the plasma-solid interface;
III. time-dependent mesoscopic models for the plasma-solid interface and
IV. macroscopic models for the plasma.

In this section, we give a concise overview of several standard simulation methods belonging to each of these four classes, as well as a few less standardized techniques that are expected to be useful for plasma-surface interactions in particular. It is not in the scope of this review article to provide a fully-comprehensive overview, since there are numerous elaborate and scrutinizing review papers already available on these procedures. Instead, we want to present some crucial computational strategies in a menu card format, to aid astrophysicists, meteorologists, plasma scientists and engineers in selecting the most appropriate approach for their studies. Doing so, we will briefly discuss the main ingredients for each method, and indicate a few relevant modifications or extensions. As we will discuss at the end of this section, many more useful techniques are available or under development. We therefore want to motivate researchers working on processes that involve plasma-surface interaction to explore this multitude of alternative options. For more detailed information on a computational procedure, we refer to the instructive review articles mentioned in the text.

3.2.1 Class I: time-independent atomistic models – it's a small and steady world

Density functional theory (DFT) serves as the most common technique to calculate the electronic ground state structure in physics and chemistry [1, 61, 62]. Two beginner's guides to this computational procedure have been assembled by Capelle and by Morgante and Peverati in their reviews [62, 63]. It is based on two theorems by Hohenberg, Kohn and Sham [4, 61, 62]. The first theorem regards the ground state energy of a non-degenerate electronic state as a unique functional of its density. According to the second theorem, this energy can be determined by varying the density functional with respect to the charge density. The density functionals are, however, partly chosen in agreement with experimental data, making DFT not necessarily a purely *ab initio* method. As an advantage, this approach significantly reduces the required computational time. In its pure form, it only considers the ground state of the system at $T = 0$ K, and therefore neglects any dynamics. Still, extensions can be made to include plasma-induced effects, e.g. by simulating an electric field as an external force [37, 64, 65]. Since core electrons in deeper-lying levels do not contribute a lot to several material properties, such as chemical bonds and magnetic behavior, an approximation can be made where only valence states are taken into account. This so-called pseudo-potential framework strongly simplifies the DFT calculations and therefore knows a wide application [2]. Figure 3 illustrates how DFT can be applied for plasma-surface interaction studies [66]. In this example, the pseudopotential is described with the projector augmented-wave method, a computationally less demanding generalization of the linear augmented-plane-wave method [67].

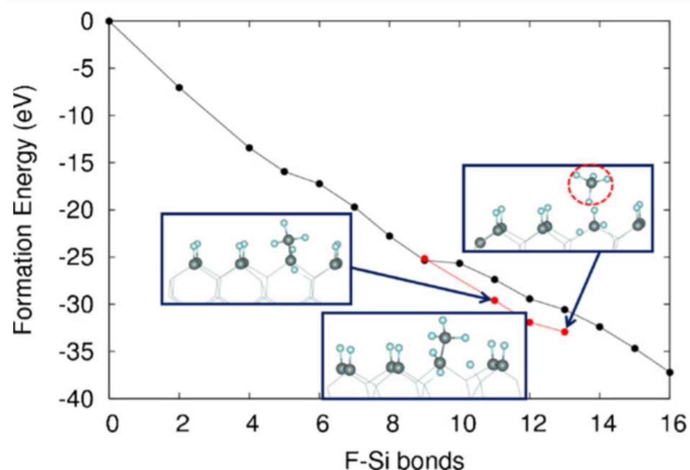

Figure 3. The reaction pathways for the fluorination of a Si(001) surface under exposure to CHF_3 plasma as a function of the number of chemisorbed F atoms or F-Si bonds, according to DFT simulations. The black curve corresponds to the situation where the F atoms are evenly distributed over the surface. The red curve shows an additional pathway, where F atoms are subsequently supplied to the same Si site, leading to SiF_4 formation. The insets show the surface structure in the corresponding successive steps. Blue and grey balls indicate F and Si, respectively. Since the red reaction pathway is energetically more favorable than the black one, the associated SiF_4 formation will take place with a higher probability than the oversaturated fluorination of the surface, in agreement with experiments. Reprinted from Appl. Surf. Sci. 257, 8767 (2011) [66], Copyright 2011, with permission from Elsevier.

Nevertheless, DFT fails to provide realistic results in some cases, especially when strong electronic correlations are present. Strongly correlated materials are a wide class of insulating and electronic compounds in which electrons cannot simply be described as localized or quasi-free. The outer shell electrons reside in an intermediate state, which cannot be described with classical DFT. Currently, the most effective and popular approach to resolve this issue is dynamical mean field theory (DMFT) [68, 69], based on a mapping of the full many-body problem onto a quantum impurity model. More precisely, DMFT translates the many-body system into a bath of uncorrelated electrons embedding a single impurity atom with a small number of quantum degrees of freedom [70, 71]. Subsequently, the hybridization between the impurity and the bath is deduced self-consistently. In this manner, DMFT treats band-like and atomic-like aspects on equal footing, allowing a minimal description for the electronic structure of strongly correlated systems [69, 70]. However, DMFT is blind to chemistry and thus needs to be combined with other methods, to obtain a more realistic picture. As such, it is often combined with DFT or with the local density approximation (LDA) derived from DFT [69, 71-74]. Since this combined approach only accounts for local correlations, several DMFT extensions have been proposed to include the effect of the non-local component (see e.g. [72, 75-77]). For a perspicuous introduction to DMFT, we refer to the review by Paul and Birol [71].

Quantum Monte Carlo (QMC) simulations form another strategy to include electronic correlation effects. This approach encompasses a variety of computational methods for the study of quantum systems, with the use of Monte Carlo algorithms as a common denominator. Most of these algorithms operate by means of random walks, also known as Markov chains [78]. Though computationally expensive, they allow benchmarking and validating output from other methods. For the simulation of the ground state, the most common variants are variational and diffusion Monte Carlo (VMC and DMC). The former relies on the variational principle in quantum mechanics, for which an initial trial

wavefunction is required [78-81]. The latter is a real-space stochastic projector technique that maps the time-dependent many-body Schrödinger equation in imaginary time on a classical diffusion equation [80, 82]. In this way, the trial function is projected to the ground state of the system by propagation in imaginary time [78-83]. Next to that, several QMC methods are available for systems at finite temperatures. Path integral Monte Carlo (PIMC) resembles DMC, but replaces the trial wavefunction with a many-body density matrix, making it a diagrammatic method [80, 82, 83]. As it becomes problematic at lower temperatures, coupled electron-ion Monte Carlo (CEIMC) has been proposed as an alternative, distinguishing between ions and electrons with the Born-Oppenheimer approximation [78, 82]. Another promising QMC method is auxiliary-field Monte Carlo (AFMC), where the many-body ground state wavefunction is translated to the state space of single-particle Slater determinants that are subject to a fluctuating external potential [78, 84, 85]. In other words, it combines stochastic sampling with the machinery of DFT and other standard electronic structure methods in chemistry and physics, and thus can take advantage of years of experience on these algorithmic procedures. A low-threshold and more elaborate introduction to these QMC methods is given in the mini-review by Ceperley [78].

Last, but not least, electronic correlations in many-body systems can also be studied with formulations that include the Bethe-Salpeter equation (BSE) [86-88]. Although this approach is typically applied to electronically excited materials (see e.g. [88, 89]), it can also surprisingly accurately describe the ground state, if it is evaluated within the adiabatic-connection fluctuation−dissipation theorem framework [90, 91].

3.2.2 Class II: time-dependent atomistic models – one small step for an atom

DFT is made time-dependent by means of the Runge-Gross theorem, which brings us to the second class of standard simulation methods. Time-dependent DFT (TDDFT) comes in several versions, depending on the approximations being chosen [1, 92, 93]. The approximation for the exchange-correlation potential strongly determines its limits in applicability. In the adiabatic approximation, for instance, the initial state and memory of the system are neglected. Two tutorials on TDDFT for a non-specialist audience have been compiled by Adamo and Jacquemin and by Ullrich and Yang in their reviews [93, 94]. An outline of the past, present and future of the technique is given by Maitra in her perspective [92]. In order to describe the motion of the ionic cores, as well as the mutual influence between the ions and electrons, TDDFT can be coupled to the less computationally expensive Ehrenfest molecular dynamics (TDDFT-MD). Analogous to time-independent DFT, a cost reduction is possible by means of pseudopotentials [1, 95]. As an example, Figure 4 presents the output of TDDFT-MD simulations of a proton incident on an aluminum cluster with an ionic pseudopotential for the electronic states of the metal atoms [96]. If the mutual influence between the ionic and electronic subsystems may be neglected, one can return to time-independent DFT, to obtain DFT-MD, also known as Born-Oppenheimer molecular dynamics (BO-MD). In this approximation, forces for the ion dynamics are calculated from the DFT ground state density. In other words, the electronic subsystem is assumed to react much faster than the ionic subsystem, in such a way that it remains in its ground state at all times. Whereas the electrons in BO-MD are treated as a quantum system, Car-Parrinello molecular dynamics (CP-MD) maps them onto a classical system, with Newtonian dynamics evolving at the same timescale as the nuclei [97, 98]. The electron dynamics are calculated on-the-fly by assuming a fictitious mass for the electrons [99]. In this way, the time-independent DFT of BO-MD is artificially translated into a time-dependent DFT in CP-MD. Both methods accordingly allow to include a finite temperature and entropic effects into the simulation [37].

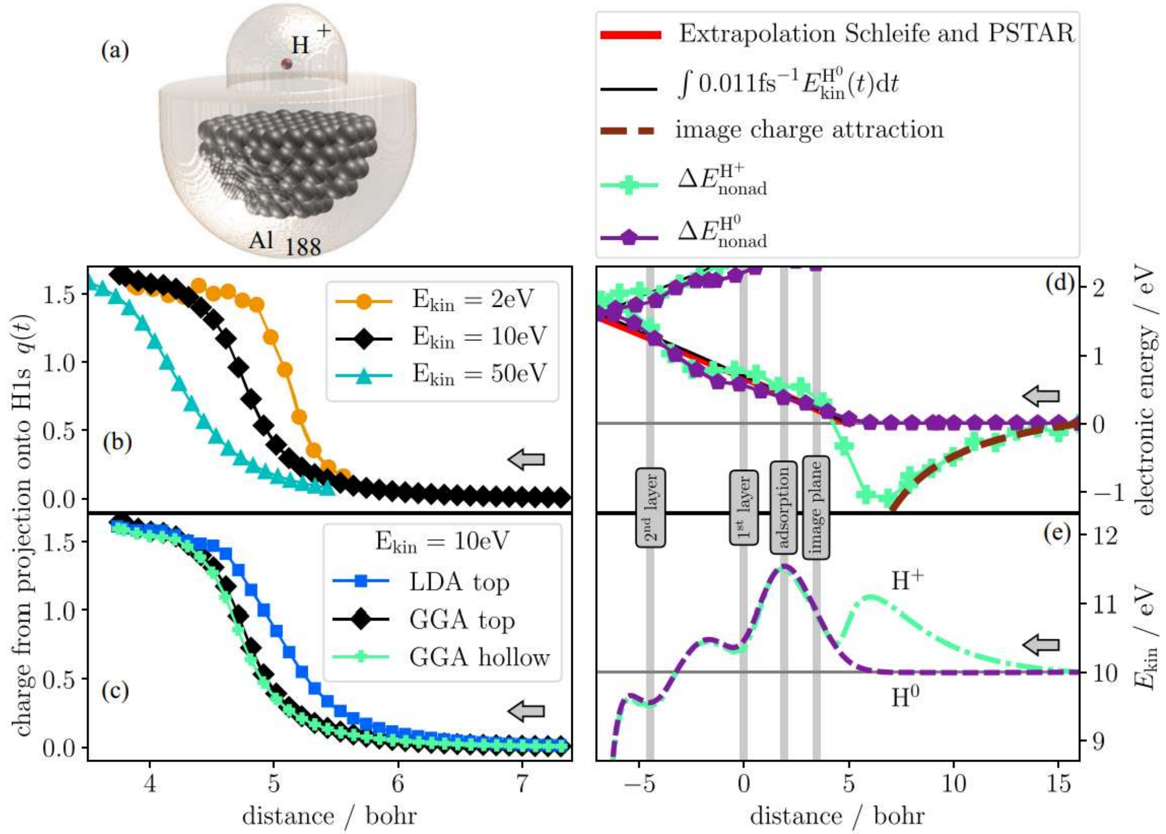

Figure 4. TDDFT-MD simulation output for a proton with a kinetic energy E_{kin} incident on an aluminum cluster. (a) Visualization of the system in the simulation box of a hemispherical cluster with 188 atoms. (b) Charge transfer from the Al(111) target to the H^+ projectile as a function of the distance between them, where 0 bohr represents the uppermost Al-layer. (c) Comparison of the charge transfer between the results from the generalized gradient approximation (GGA) and the local density approximation (LDA) for the hemispherical cluster with H^+ incident on the on-top site and for a modified cluster of 172 atom with H^+ incident on the Al(111) fcc hollow site. (d) Comparison of the electronic excitation energy and (e) the kinetic energy of a H^+ or H_0 projectile incident on the Al(111) fcc hollow-site. The ion experiences an excitation energy reduction and kinetic energy increase before reaching the image plane, due to the charge transfer and image-charge attraction. Next, it decelerates due to Coulomb repulsion, to continue the same energetic pathway in the first two layers of the cluster as the H_0 atom, until it reflects at the third Al-layer. This lies in line with the often made assumption that incident ions and atoms of the same element and with the same kinetic energy have a similar interaction with a target. Reprinted by permission from John Wiley and Sons © 2019 from Contrib. to Plasma Phys. 59, e201800184 (2019) [96].

In comparison to DFT, classical MD is computationally cheap enough to simulate condensed matter over mesoscopic spatial dimensions and relatively long time intervals. The length and time scales of this technique can be dramatically extended using large supercomputers for massive parallelization and dedicated strategies for the acceleration of selected processes (see Figure 1) [1, 100-102]. A MD simulation has, for instance, been reported in Ref. [103] on a system containing 10^{11} atoms, reaching times in the order of a few milliseconds. This semi-classical method operates by means of interatomic interaction potentials that are either empirically derived or obtained with quantum mechanical methods [1, 37, 104, 105]. As such, it does not explicitly consider electronic effects or quantum

dynamics of the nuclei, and should therefore be distinguished from *ab initio* MD, such as BO-MD or TDDFT-MD. Still, it permits the simulation of various surface processes, including diffusion, adsorption, desorption and chemical reactions [1, 37, 106-109]. Effects with a strong quantum mechanical character, such as changes in the work function and surface group activation by UV photons, however, require other computational methods, which explicitly consider the involved quantum mechanisms [4, 37]. Still, classical MD can be extended to account for certain quantum effects, e.g. by implementing a frictional force for electronic stopping, by adding a high-energy repulsive part in the interatomic potentials and by using an adaptable time step for energetic collisional events [4, 110, 111]. In the book chapter by Lorentz and Doltsinis [112], an overview is given on the most widely used MD technology, ranging from the *ab initio* methods, via classical MD up to coarse graining techniques. The latter authors also present a practical guide on how to select and implement the different strategies. The importance of the MD simulation methods for the study of plasma-surface interactions is clearly illustrated by the reviews devoted to this topic, e.g. [3, 7, 113].

In order to reach even larger length scales with an atomistic model, the binary-collision approximation (BCA) can be applied. This approach neglects binding energies, and calculates the passage of an ion in a solid, liquid or gaseous material as a sequence of independent binary collisions. For this purpose, the classical scattering integral is solved for purely repulsive interatomic potentials [4, 114, 115]. Due to its approximate nature, it can only produce physical results for single ions on sub-picosecond time scales. Although BCA cannot accurately determine atomic structural effects related to sputtering, ion implementation and defect formation, it permits to estimate the resulting damage and composition change in the surface [4]. It therefore serves as a valuable tool for the study of surfaces in contact with high-temperature plasmas, as in fusion reactors.

Finally, another type of time-dependent standard atomistic models is based on real-time non-equilibrium Green functions (NEGF). This method enables the description of electronic correlation effects in quantum many-body systems out of equilibrium, e.g. to simulate secondary electron emission, in a way complementary to TDDFT. At present, it namely does not allow yet for a full quantum-mechanical treatment of a projectile incident to a surface [1]. The method may be understood as a straightforward generalization of classical kinetic theory, as for instance predicated on the Boltzmann equation. Like TDDFT, NEGF is computationally very intensive, strongly limiting the accessible time and length scales. From the positive side, it has a very broad applicability, on systems ranging from usual condensed materials to nuclear matter and dense laser plasmas [1, 116]. It is therefore also expected to be feasible for the study of relaxation mechanisms in a surface after excitation by an incident plasma particle. In order to describe a wide range of realistic materials, NEGF can be coupled to a Kohn-Sham basis precomputed by a ground state DFT simulation, to yield *ab initio* NEGF (AI-NEGF). For more detailed information on how to apply this technique, as well as most of the aforementioned atomistic time-dependent models, to plasma-surface interaction, we refer the reader to the highly recommended review by Bonitz et al. [1]. An even deeper dive into the NEGF approach can be taken in the elaborate review by Schlünzen et al [117].

3.2.3 Class III: mesoscopic models – computational compromise

From the NEGF equations, quantum kinetic methods based on the quantum Boltzmann equation (QBE) can be derived, e.g. for the description of secondary electron emission or scattering processes affecting the electronic structure of a projectile-target system [1]. This permits a reduction of the computational intensity, by coarse-graining the solid surface, assuming spatial homogeneity and by using effective mass models. For this reason, the QBE approach may be considered a mesoscale model,

according to the definition we adopted. However, it remains computationally heavy in comparison to other mesoscopic models, restricting the accessible spatial and temporal dimensions of the system. It also fails in resolving ultra-short length and time scales of the surface, as it does not treat electron dynamics and correlations in the material [1].

Among the other mesoscopic models in the third class, kinetic Monte Carlo (KMC) forms the most popular approach. It is sometimes also referred to as dynamic Monte Carlo, and has been discussed more extensively in several review articles [2, 4, 100, 118, 119]. This method does not explicitly treat the quantum dynamics involved in the process. Instead, it applies a stochastic algorithm to propagate the ensemble of reacting species through discrete jumps from state to state, by means of a custom-made reaction catalogue with predefined probabilities. In the case of plasma-surface interaction, the ensemble consists of incident plasma species at the one hand and surface groups at the other. In order to reduce the simulation time, it often considers super-particles for the plasma, i.e. computational particles representing a collection of real, physical plasma species. Surface groups are merged in an analogous manner. Every reaction between a plasma and a surface species is discretized as a single and sudden event, with one or more possible outcomes, each of which with a probability defined in the custom-made reaction set. With these simplifications, KMC can simulate processes with a duration up to several minutes and length scales of some centimeters. Nevertheless, its accuracy is limited by the amount of elementary knowledge on the underlying surface reactions. In Section 4, we will demonstrate how to assemble a reaction set based on such fundamental data, retrieved from experiments and atomistic models, for the case of plasma etching. With an accurate fundamentally benchmarked surface chemistry set, KMC becomes a powerful tool to predict the evolution of a plasma-material interface. In the absence of quantitative knowledge on basic surface processes, however, errors in the set are extremely hard to identify.

Another powerful strategy to simplify many-body problems in quantum mechanics relies on the introduction of quasiparticles [120-122]. Here, we adopt the broad definition of a quasiparticle, i.e. encapsulating both dressed fermions and bosonic collective excitations [123, 124]. Similar to real particles, quasiparticles behave as a thermodynamic ensemble with quantum behavior at the microscopic scale, which can be approximated with semiclassical and classical models for simulations at a larger scale. Even at the microscopic scale, the translation from a real atomistic model to a quasiparticle formulation is generally associated with a simplification on a supra-atomic level, because multiple real particles contribute to the identity of a single quasiparticle. This implies a type of coarse-graining, providing access to larger time and length scales. However, the development of quasiparticle models for plasma-surface interaction is still in its infancy, as no studies have applied this strategy yet, to our knowledge. Inspiration can be taken from the two-temperature models frequently used to investigate electron-phonon coupling in laser-excited matter [125-127]. The so-called multi-plasma model (MPM) has recently been proposed as a generalized extension of these models, with the addition of plasmons, excitons and optionally molecular excitations [31]. This conceptual description has been designed for all vibrationally and electronically excited condensed matter systems. It may therefore prove to be a useful universal framework for the investigation of the excitation and relaxation dynamics at a plasma-material interface, which is not possible with other mesoscopic models. As a somewhat related mesoscale approach, discrete dislocation dynamics (DDD) simulates the behavior of dislocations by means of connected line segments that represent a dislocation line and that interact via their strain fields [4, 57, 128-133]. By giving the segments a fictitious mass and realistic interaction strength, their motion is solved with the same basic principles as in classical MD [4, 57]. In this way, plasma scientists can computationally determine the mechanical response of materials to plasma contact.

3.2.4 Class IV: macroscopic models – the big picture

Finally, the fourth class contains the macroscopic models for the plasma bulk and the plasma sheath. Due to the fluid nature of plasmas, computational fluid dynamics (CFD) has become a popular approach for this purpose [100]. For non-equilibrium low temperature plasmas, this technique relies on a set of differential equations, obtained by taking velocity moments of the Boltzmann equation [100, 134]. More specifically, this equation set describes the electrons, ions and neutral species as distinct subsystems of the fluid. The electrons and ions are coupled through Maxwell's equations or Poisson's equation, while ions and neutrals are usually assumed to have the same temperature [100, 134]. A further simplification can be made for the electrons with the well-known two-term approximation, by assuming homogeneous and stationary conditions [36, 100]. Since ions and electrons are consumed at the boundaries, this particle loss needs to be compensated by including an ionization rate [100]. The differential equation set can be solved by means of finite element, finite difference, finite volume or spectral methods. Which of these methods is selected, depends on the requirements and preferences in terms of computational time and memory usage, as well as simulation stability and accuracy [135, 136]. In practice, however, the finite element method is rarely used, most likely because it is computationally heavier and requires special care to ensure a conservative solution [136]. Despite these disadvantages, its performance is much more stable than, for instance, the finite volume method [136, 137], which may be crucial for certain applications. As an example, Figure 5 presents the output of a finite volume method with an unstructured triangular mesh, describing the plasma treatment of a polymeric textile [49].

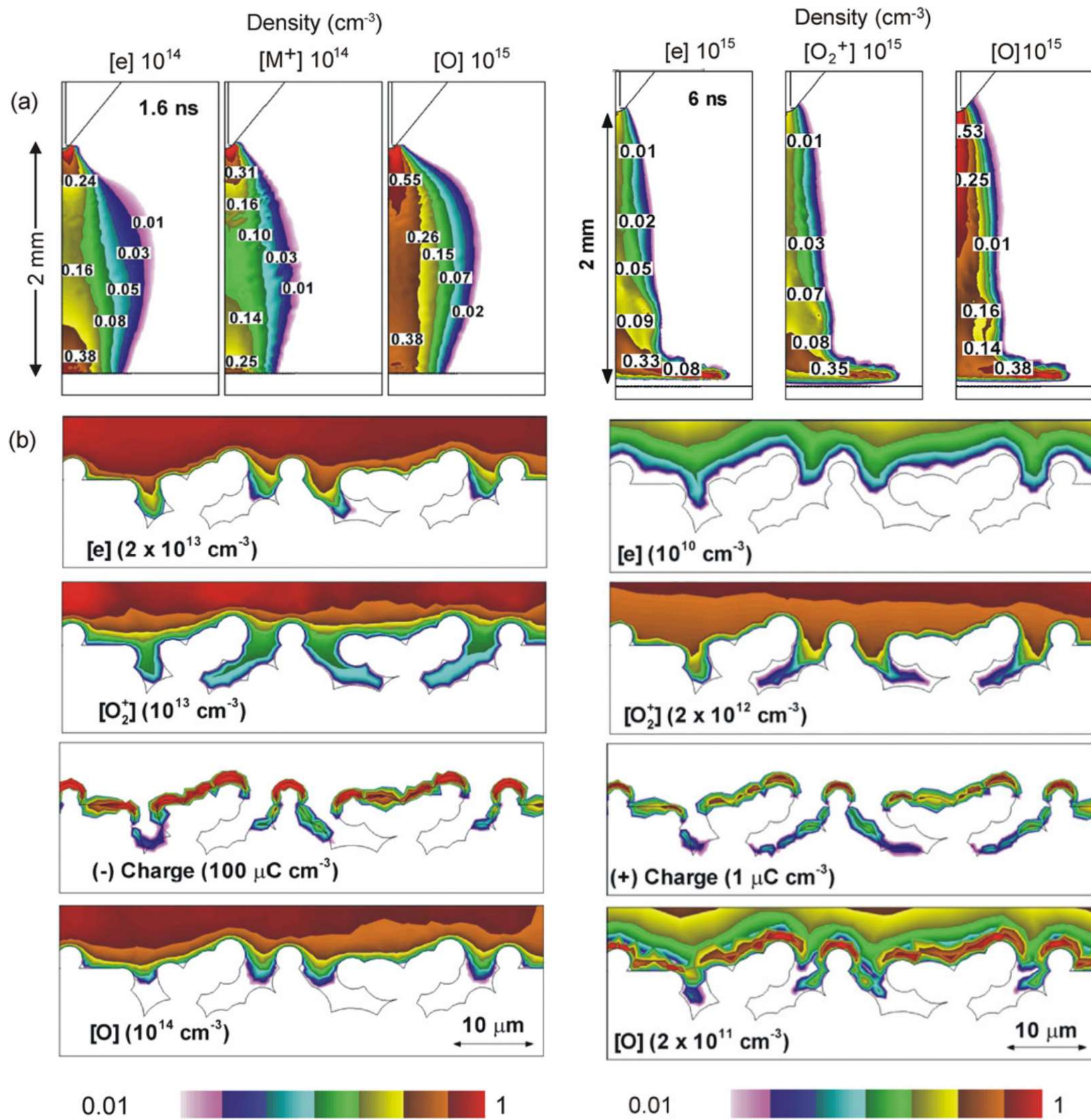

Figure 5. Simulation output of a two-dimensional plasma hydrodynamics model integrated with a deterministic description for the surface kinetics, applied to repetitively pulsed atmospheric pressure corona treatment of a rough and porous polypropylene surface. The plasma properties after the first breakdown pulse are shown for (left) a negative and (right) a positive humid air discharge, with (a) the densities of electrons, positive ions M^+ or O_2^+ and oxygen atoms between the corona electrode and the polymer sheet, and (b) the densities of electrons, O_2^+, negative or positive surface charge and O atoms in the vicinity of the surface. The contour labels are fractions of the maximum density, which are noted in each figure. The results explain the macroscopic higher and microscopic lower uniformity in treatment for the positive discharge, due to the spreading of the discharge along the surface and the poorer plasma penetration into the surface features, respectively. Republished with permission of IOP Publishing, Ltd, from Plasma Sources Sci. Technol. 17, 035024 (2008) [49]; permission conveyed through Copyright Clearance Center, Inc.

A higher accuracy can be obtained with Monte Carlo methods, where the super-particles exclusively represent plasma species. These kinetic techniques should be distinguished from QMC and KMC, because they do not treat solid particles or surface groups. A traditional approach is given by direct

simulation Monte Carlo (DSMC), which considers the collisions between two simulation particles [138, 139]. In contrast, the Monte Carlo collisions (MCC) method assumes the collision of the computational particles with a fixed target cloud, which strongly simplifies the implementation and reduces the simulation time [140, 141]. Such Monte Carlo procedures can be coupled in a straightforward way to the particle-in-cell (PIC) method, as the latter also makes use of super-particles. The name of this method originates from its working principle, where typically around 100 computational particles or more reside in a mesh cell. The PIC method tracks these particles in continuous phase space, while the electric field and charge densities are calculated on the mesh points [100]. Collisions between the particles can be included with the Monte Carlo methods. These approximations provide an efficient framework for an accurate description of low-density plasmas [100]. This explains, for example, the popularity of particle-in-cell with Monte Carlo collisions (PIC-MCC) simulations for non-equilibrium low temperature plasma simulations.

These macroscopic simulation techniques also apply to high temperature plasmas and astrophysical plasmas, but with some restrictions and modifications. More specifically, the influence of the magnetic field is often crucial in these systems, so the theoretical framework and thus the underlying differential equations need to be adjusted. Such a general framework is formed by magnetohydrodynamics, describing the plasma as a single fluid, based on approximations for large spatial scales and low frequencies [142-145]. In order to obtain a higher accuracy, a multi-fluid variant can be used. These approaches are feasible to simulate full-scale systems in a so-called global model, in contrast with local models meant for simulations at a smaller scale [143]. Next to that, plasma turbulence effects in magnetized plasmas are often investigated with gyrokinetics as a theoretical framework [144, 146, 147]. In considering microtubulence, the Boltzmann equation is replaced with the collisionless Boltzmann equation, also called Vlasov equation. Several extensions into gyrokinetic magnetohydrodynamics have been developed as well [148-150]. Analogous to the case with low temperature plasmas, these frameworks are implemented in fluid and kinetic models, or possibly a combination of both [146, 147, 151-153]. The PIC-MMC method is, for instance, a suitable technique to study gyrokinetics [154].

In practice, non-identical macroscopic fluid and kinetic methods are often combined in a single computational code, resulting in a so-called hybrid model [47, 100, 134]. This strategy differs from multiscale simulation, because the combination is implemented on the same macroscale. The ions, electrons and neutrals in a multifluid model may, for instance, be treated individually with different algorithms, which are coupled through the differential equations. In Section 4.1, this principle will be illustrated with the Hybrid Plasma Equipment Model (HPEM) developed by the Kushner group for the simulation of plasma etching [47]. In addition to the fluid or super-particle representation of a macroscopic system, the reactions between the plasma particles are frequently accounted for with a chemical kinetics model [100]. In isolated form, the latter type is also referred to as a global model (not to be confused with the aforementioned full-scale magnetohydrodynamic treatment), or a 0D model, since it can be used to calculate the spatially averaged plasma chemistry. Such method operates by means of the particle and energy rate-balance equations for the main plasma species, defined in a plasma gas chemistry set. Coupled to a fluid or kinetic method, a 0D chemical kinetics model is extended into a plasma chemical model of higher dimensionality.

Up to now, we only discussed how macroscale models present the plasma phase. A material in contact with the plasma is usually simplified as a homogeneous metal or dielectric. First of all, its presence influences the plasma due to its role in the electric circuit of the system, as well as its contribution to the electric and magnetic field effects dictated by Maxwell's equations or Poisson's equation. Secondly, the plasma-surface interaction affects the particle transport across the interface through

surface reactions, species deposition and emission back into the plasma [155]. This surface chemistry is similar to the one considered in KMC. However, it cannot be treated in terms of computational particles colliding with individual surface groups, because the surface is no longer resolved in such groups. As a solution, the surface composition can be expressed with the surface group fractions. This allows the deterministic calculation of the species emission from the surface into the plasma [47]. Accordingly, this methodology is sometimes called a deterministic description (DD), and may be understood as a coarse-grained version of KMC [118, 119]. The model of Figure 5, for instance, employed this strategy.

3.3 Unconventional simulation methods – a tool box for out-of-the-box thinking

3.3.1 Less explored methods from the four classes – the need for computational wanderlust

As should be noted, the aforementioned methods of the four classes include several popular standard simulation techniques, as well as some promising additional strategies, for plasma-surface interaction, but this list is not exclusive. As a rule of thumb, the methods of the four classes are universally applicable, i.e. not restricted to the plasma-surface interaction physics, or any of its specialized subdomains. Many more of such universal computational techniques have been developed independent from the plasma-surface interaction problem, which may aid its multiscale modeling strategy. On the atomic scale, for instance, the quantum many-body problem can also be treated with various alternative procedures, such the Hartree-Fock method [79, 156-158], perturbation theory [158], configuration interaction techniques [158], and semi-empirical methods [157, 159]. The potential use of these methods for the study of plasma-surface interaction needs to be emphasized, which is the purpose of the present Section.

On the macroscopic scale, the lattice Boltzmann method (LBM) presents itself as a promising, but largely unexplored plasma simulation approach. LBM is a relatively new computational fluid dynamics tool [160, 161], known for its remarkable flexibility and performance. Unlike the traditional CFD methods, it models the fluid as an ensemble of fictive particles, similar to the PIC technique. These particles move over a discrete lattice mesh, where they consecutively propagate between nodes and perform collision processes at the location of the node. Due to this working principle with local dynamics, LBM has several advantages over other fluid simulation methods, such as the straightforward parallelization of the algorithm [162, 163], easy description of complex boundaries [164-168], incorporating microscopic interactions [169, 170] and multiphase flows [168, 171]. Moreover, it is readily combined with a Monte Carlo procedure, to enable accurate simulation output, analogous to PIC-MCC, at a strongly reduced computational cost [172-175]. LBM can also be understood as a discrete representation of the Boltzmann transport equation [176]. All of these features make it an attractive alternative for plasma simulations, especially in situations where the discharge contains aerosol particles or is in contact with a complicated surface.

Nonetheless, LBM has only sporadically been applied to plasma systems up to now, e.g. in [177-179]. Similar remarks can be made about the vortex-in-cell (VIC) method for magnetized plasmas, where the support of the flow vorticity is approximated by a discretized vortex system [180]. We therefore want to motivate astrophysicists, meteorologists, plasma scientists and engineers to explore these alternative techniques, in order to facilitate the computational description, as well as the fundamental study, of plasmas and plasma-surface interaction in particular. For this purpose, the literature review of accelerated CFD simulation methods by Hosain and Fdhila in [181] can serve as valuable source of inspiration, as displayed in Figure 6. Note that such CFD methods also apply to the implementation of

quasiparticle models, which lend themselves more for descriptions on the mesoscale (see class III). They may therefore also be useful to include collective excitations and quantum effects, in the plasma, in the condensed phase or in the interface between them. This approach is especially interesting for the study of long-range correlations or any other quantum processes at the plasma-material interface, which are currently inaccessible in terms of length or time scales by atomistic models.

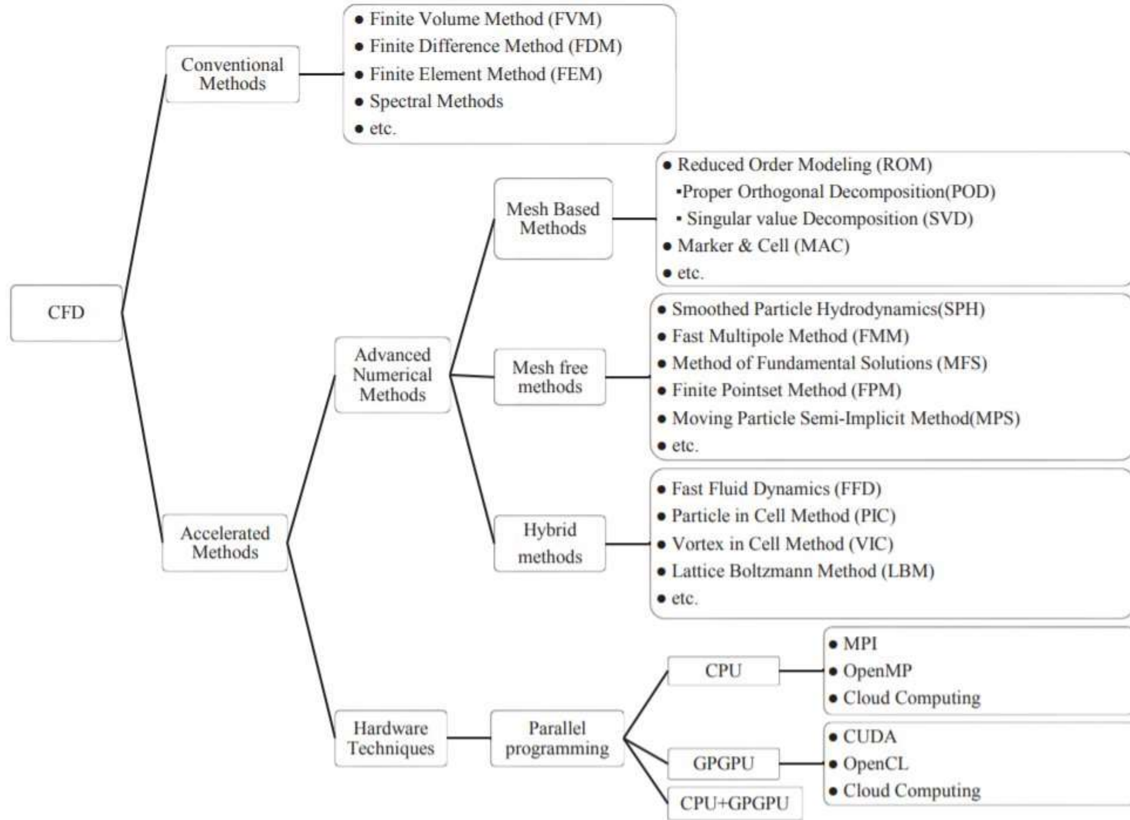

Figure 6. Hierarchical classification of various CFD methods applicable to plasma simulation. Next to the conventional procedures, numerous accelerated techniques have been developed in CFD, based on enhanced hardware utilization and advanced numerical algorithms. The latter can be distinguished into mesh based, mesh free and hybrid methods, depending on whether they rely on the Eulerian approach (i.e. using a mesh with fixed coordinates), the Lagrangian approach (i.e. representing the fluid with a large number of computational particles) or both, respectively. Hybrid methods in this context should not be confused with the hybrid models discussed elsewhere in this review, since the latter refer to models that combine non-identical methods for different plasma components. Reprinted from Energy Procedia 75, 3307 (2015) [181], Copyright 2015, with permission from Elsevier.

3.3.2 Application-specific methods – specialize in the impossible

The standard and unconventional simulation methods belonging to the four classes are universal in nature, meaning that they apply to a wide range of plasmas, materials and their interaction. Depending on the application or the process under study, more specialized computational methods can be included in a multiscale modeling strategy. Such application-specific techniques are especially expected on the mesoscale. For example, the evolution of the surface roughness, nano- and microstructure forms an essential aspect in many applications, such as plasma etching for

microelectronics fabrication, polymer treatment and plasma catalysis (see Section 2). If, for a certain purpose, this evolution needs to be calculated in shorter computational times than accessible with KMC, geometric methods that only consider the surface shape can be a practical alternative. These simplified methods are tailored to rapidly predict the surface deformation without an explicit treatment of the underlying physics and chemistry. A first step in their design consists of collecting surface shape data from more accurate methods like KMC or experiments. Based on this data, a geometric method can subsequently be benchmarked through manual parametrization or trained through machine learning, to rapidly simulate the surface evolution.

3.3.3 Machine learning – brainstorming by artificial intelligence

Also in the broader context of multiscale modeling, machine learning has a high potential to become one of the most popular computational strategies. The synergetic integration of multiscale modeling and machine learning has been discussed in a few recent review papers, for applications in material, biological, biomedical, and behavioral sciences [182-186]. Both strategies are seen as complementary to each other, where machine learning permits to analyze and interpret large data sets, while multiscale modeling provides insight on a fundamental level. Moreover, machine learning can also process the large quantity of complex output data from an individual standard simulation method, for multiple purposes [183, 187, 188]:

- to calibrate, augment or correct the simulation results,
- to make the complex output data human comprehensible,
- to reveal hidden relationships between, for instance, the structure and properties of a material, or between the plasma and surface features, and their interaction,
- to make studies more targeted, by interfacing their discovery and design objectives,
- or even to partly or completely replace the simulation method.

Figure 7 shows an example of an artificial neural network successfully used by Krüger et al. in the context of plasma-based sputter deposition for the supervised learning of statistically disturbed data sets [189]. This network was proven able to accurately approximate the relationship between the energy distribution of an incident plasma species and the energy and angular distributions of the species sputtered from the surface upon its impact. Another example has been investigated by Xiao and Ni for the optimization of a plasma etch process, where recurrent neural networks were applied to approximate a KMC and fluid multiscale model [50]. More elaborate discussions on the aforementioned functions of machine learning are given in a review by Schleder et al. regarding DFT [183], a perspective by Wang et al. regarding MD [188] and a review by Haghighatlari and Hachmann regarding molecular modeling [187]. Accordingly, we expect machine learning to become a multifunctional tool in the multiscale modeling strategy of plasma-surface interaction, both for fundamental scientists and engineers.

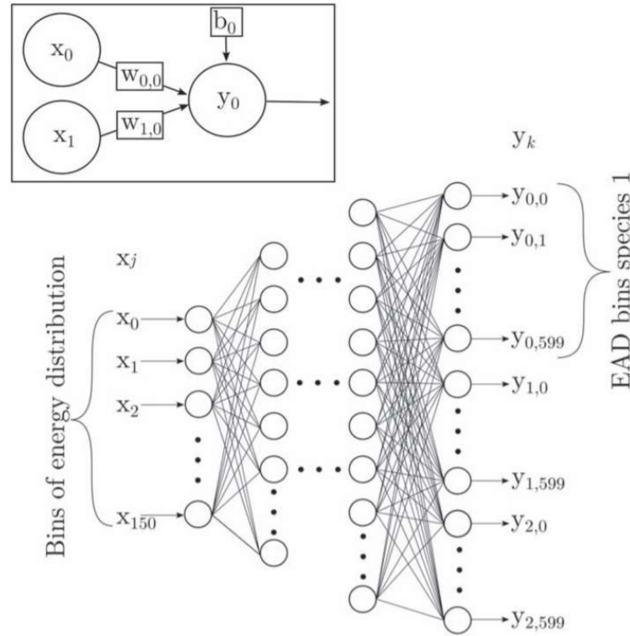

Figure 7. Conceptual schematic of an artificial neural network that couples the energy distribution of plasma ions incident on a surface, denoted as the input x_j, with the energy and angular distributions (EADs) of the correspondingly sputtered species, denoted as the output y_k. As shown in the inset, single nodes with inputs x_j and outputs y_k are indicated with circles, whereas weights $w_{j,k}$ and biases b_k with rectangles. The layers between input and output layer are commonly referred to as hidden layers. Using this working principle, the relationship between the input and output can be approximated in general without programming any task-specific rules. Reprinted from [189], F. Krüger, T. Gergs, and J. Trieschmann, Plasma Sources Science and Technology Vol. 28(3), 2019; licensed under a Creative Commons Attribution (CC BY 4.0) license.

3.3.4 Plasma sheath modeling – matter's aura explained

Electrons have a much lighter mass than ions, by a factor of 2000 or more, depending on the plasma gas. Next to that, the electron temperature is generally much higher than the ion temperatures. Accordingly, electrons display a significantly higher mobility and will more rapidly reach a nearby plasma boundary. If this plasma boundary consists of condensed matter, the plasma electrons can get trapped in electronic levels below the vacuum level, such as surface states, the conduction band or unoccupied valence orbitals. In this way, an initially unbiased material submerged in a plasma will almost instantly obtain a negative surface charge. Simultaneously, a positive space charge region is formed above the surface, due to the extraction of the electrons from this region, as well as the Coulomb repulsion of plasma electrons by the negative surface. Such an electrical double layer is widely known as a plasma sheath, a term which has been introduced already in the late 1920's by Langmuir. More specifically, the above description refers to an ion sheath, the best known example of a plasma sheath.

During the past century, different variants have been reported in literature, depending on factors like the plasma conditions, the surface geometry and the bias voltage applied to the material. The experimental geometry namely controls the global current balance in a way that constrains the sheath type that is possible. Strikingly, this role of the geometry has only been realized recently [190, 191].

Moreover, although ion sheaths are often considered to be well understood, certain controversies remain on their theoretical description, as discussed further below. Figure 8 displays the electrostatic potential profile of five plasma sheath types, including an ion sheath, an electron sheath, a double sheath, an anode glow and a fireball. Whereas ion sheaths are usually described using a local analysis of a boundary interacting with an infinite plasma, other sheath types often depend on global features of the plasma and the confinement chamber [190]. This dependency on non-local physics of global plasma self-organization emphasizes the relevance of multiscale modeling for the study of plasma sheaths. Considering the theoretical difficulties in describing ion sheaths, this relevance may be generalized to all types of sheaths.

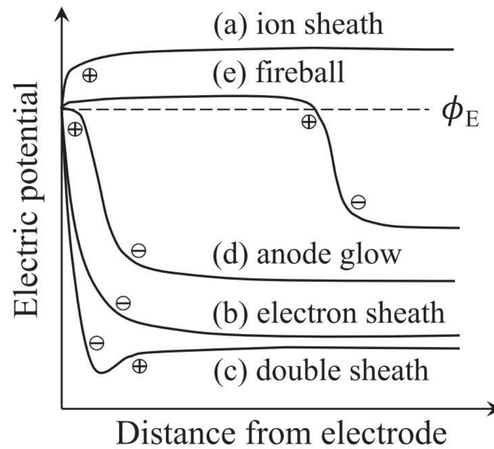

Figure 8. Sketch of the electrostatic potential profile of various plasma sheath types that can form at a biased electrode. Regions of positive and negative space charge are denoted by plus and minus signs, respectively. Republished with permission of IOP Publishing, Ltd, from Plasma Sources Sci. Technol. 29, 053001 (2020) [190]; permission conveyed through Copyright Clearance Center, Inc.

Reversely, multiscale modeling of plasma-surface interaction strongly relies on an accurate account of the present plasma sheath. The surface processes and the sheath are namely closely intertwined for various reasons. On a macroscopic level, the sheath determines the boundary conditions between the plasma and the material surface, such as the deposition and emission of charges and specific plasma or surface species. Electron emission, for instance, often has a decisive influence on the plasma properties. The plasma sheath governs electron emission through multiple effects. Depending on the bias voltage on the surface, the sheath potential accelerates ions or electrons towards the material, which result in secondary electron emission. Energetic neutrals produced from accelerated ions or chemical reactions can contribute in a similar way [192, 193]. As should be noted, the secondary electron emission coefficient is very sensitive to the surface conditions, which can be modified by the plasma interaction. More precisely, the coefficient can vary over two orders of magnitude, starting from a dirty surface and evolving into a clean surface after plasma sputtering [193-195]. Next to that, the plasma affects the surface roughness, which regulates the local field enhancement and thus the possibility for field emission of electrons [37, 196, 197]. An interesting and more elaborate discussion on secondary electron emission in plasma-surface interaction is given in the review by Bonitz et al. [1].

On a microscopic level, the plasma sheath dictates the charge and mass bidirectional transport, as well as the local chemistry. The transport is straightforwardly influenced by the strong electric field, which accelerates charged particles and indirectly alters the velocity distributions of neutral species through subsequent collisions. The sheath chemistry differs from the bulk plasma chemistry for several reasons. First of all, the non-zero space charge in the sheath implies a different electron

density, ion density or both, shifting the chemistry accordingly. Secondly, etching and sputtering of the surface bring material species into the gas phase, with a higher prevalence nearby the surface than in the bulk. This results in chemistry shifts in a similar manner. Thirdly, a strong electric field may influence gas phase and surface reactions, by orienting reactants along the field and correspondingly favoring certain reaction pathways over others. An overview of such field effects has been presented in two recent tutorial review articles [198, 199]. Fourthly, the sheath properties are closely related to the surface charge collected on the material, which may also assist specific surface reactions and thus alter the species emission.

The distinct sheath chemistry determines the local densities of reactive species, which are more likely to interact with the surface than species originating from the plasma bulk. According to a one-dimensional fluid simulation study by Liu et al. on a radio-frequency atmospheric-pressure He-O_2 plasma between two solid boundaries [200], the particle fluxes onto the walls were found to originate from a 3 to 300 μm thin boundary layer contacting each electrode. This was only a fraction of the sheath thickness of 472 to 489 μm. In other words, the species incident on the surface were supplied by the sheath chemistry, in contrast to the plasma bulk chemistry as often assumed. Although this conclusion is based on a case study and therefore cannot be generalized to all plasma and sheath conditions, it illustrates the importance of the sheath chemistry to the surface processes. However, sheath chemistry has received remarkably little attention up to now in research on plasma-surface interaction. We therefore want to motivate more studies on plasma sheath modeling, with the sheath chemistry in particular, both as an integral part of the multiscale modeling strategy, and as a fundamental research topic in plasma-surface interaction science.

A plasma sheath can be implemented in a macroscale model in four different ways:

A. as a highly resolved domain at a surface in a macroscopic model;
B. as a separate mesoscale sheath model;
C. as an analytical or semi-analytical sheath model;
D. or as a simplified method, which neglects the sheath while ensuring the current passage across the surface.

In principle, method A is a special case of method B, where the former restricts the simulation of the sheath to the same standard method as the macroscopic model. In contrast, the latter permits the mesoscale sheath model to operate with a different algorithm than the macroscopic model it is coupled to. The mesoscale nature of such a separate sheath model simply refers to the relatively small thickness of the sheath relative to the plasma dimensions. Both fluid and kinetic models have been developed for this purpose, including PIC methods. A detailed review on these techniques has been made by Robertson in [201]. As their main disadvantage, they can become computationally expensive, especially when a fine mesh size is required to obtain a sufficient accuracy and stability. To reduce this computational cost, macroscopic models are often coupled to analytical, semi-analytical (method C) or strongly simplified sheath models (method D). The difference lies in the way the sheath is treated. Analytical sheath models rely on one or more analytical expressions, based on several assumptions related to the sheath properties, but without the need for *a priori* knowledge on the plasma (see e.g. [202]). Semi-analytical models also operate by means of one or more analytical expressions, but require plasma parameters as input and therefore have to be integrated into a macroscale model (see e.g. [203] and Section 4.1). Simplified sheath models, as in method D, ensure a current passage across the surface by placing the mesh boundaries of the plasma zone away from the electrode sheath, by assuming an increased electrical conductivity of the plasma at the surface, or by imposing simplistic (non-analytical) boundary conditions (see e.g. [204-207]).

In a multiscale model, the plasma and sheath will generally be described by individual methods, which requires a choice on how to join the corresponding solutions. This problem can be dealt with *via* two approaches: matching and patching [208]. The method of matched asymptotic expansions has played an essential role in the past for the theoretical analysis of the plasma-surface problem. However, its successful application in analytical and numeric modeling is complicated by its mathematical complexity, as illustrated by the heated discussion that has revolved around the often applied Bohm criterion (see e.g. [201, 202, 209-214]). According to this criterion, the ions leave the quasi-neutral plasma and enter the sheath with a velocity equal to or exceeding the ion sound velocity. Assuming that this point of entrance coincides with the sheath edge, i.e. the boundary between the plasma and the sheath, as is often done, leads to inconsistencies and misconceptions [202, 210, 211]. Riemann formulated a solution for this problem by introducing a transition region between the plasma and the sheath [214-216]. Sternberg and Godyak, on the other hand, propose patching as a more practical approach, to approximate the solution of the plasma-wall problem without the need for a transition layer [208, 209]. Patching has the main purpose to obtain continuity by forcing the values of the two solutions together at a chosen location, the so-called patching point. In principle, smoothness is also possible, by forcing several derivatives together as well [208]. For more detailed information on plasma sheath models, we recommend the reviews [190, 201, 202, 214, 217].

3.4 Multiscale measuring – because nature is still the best simulation tool

Although this review mainly deals with computational methods for the study of plasma-surface interaction, a brief discussion of the experimental techniques is necessary, because they play a crucial role in the multiscale modeling too. First of all, they provide the most reliable reference systems for the benchmarking of the computational methods. Correspondingly, it makes sense to distinguish them into four classes similar to the ones proposed in Section 3.2:

I. *ex situ* and *non-operando* surface diagnostics for the material microstructure before and after plasma contact;
II. particle beam experiments to investigate the effect of individual plasma species on the surface;
III. *in situ* and *operando* mesoscale measurements to obtain the concentration of plasma species and surface groups at the plasma-material interface; and
IV. conventional plasma diagnostics.

Each class of measurement techniques can be utilized to verify and benchmark the numerical models of the corresponding computational class. We will show an example of this methodology in Section 4.2.1 for the bombardment of Si with F^+ ions. Secondly, this classification allows to evaluate the accuracy of the simulated data exchanged between the models from different classes. Accordingly, a multiscale model may be experimentally verified in a transparent way, on different levels. Section 4.1.6 demonstrates how this has been accomplished during the past decades for the Hybrid Plasma Equipment Model developed by the Kushner group for plasma etching reactors. Thirdly, if simulation data from one class is not available for practical reasons, the experimental data acquired in the associated class can serve as input for the other parts of the multiscale model, making it semi-empirical. Several examples of this practice will be given in Section 4.2.2 in the design of a surface chemistry set for Si and SiO_2 etching with fluorocarbon plasmas.

The experimental classes I and IV are widely used and known by the plasma community, due to their ease of use and general importance in the field. Classes II and III, on the other hand, are less common,

yet of extreme interest to the study of plasma-surface interaction. They therefore deserve an additional explanation. Class II encompasses all types of experiments where the interaction between a material and a particle beam, corresponding to a single plasma species, is investigated. In order to be representative for the plasma-surface interaction, the beam properties need to be tuned to approximate the local conditions, such as the flux and the kinetic energy of the particles incident onto the surface. Likewise, the surface may need a special pretreatment to correspond to the specific conditions under plasma contact. Such particle beam experiments can offer valuable information on several effects, such as the amorphization and functionalization of the surface, deposition and etching rates or more specified reaction probabilities, scattered and emitted particle distributions, including secondary electron emission coefficients, data on energy dissipation channels and time scales, and so on. Moreover, particle beams directed under a varying incident angle with the surface enable the measurement of the angular dependence of these effects. In principle, any type of plasma particles can be considered, i.e. ions, electrons, radicals, metastables, molecules and photons. Although not strictly a particle beam, a gas of radicals interacting with a surface may be included in this class of experiments. As should be noted, atomic layer etching and atomic layer deposition often occur under similar controlled conditions [218-221], helpful to the multiscale modeling strategy. In Section 4.2, various examples of experimental studies from class II in the scientific literature will be discussed and used for our case study.

The experimental class III relates to the current trends towards *in situ* and *operando* surface and sub-surface characterization techniques, to unravel elementary mechanisms at the plasma-material interface on the atomic scale. The applicability of *in situ* Fourier transform infrared (FTIR) spectroscopy for the investigation of plasma-surface interactions has, for instance, been elaborately discussed by Shirafuji et al. a while ago [222]. More recently, Allain and Shetty discussed many other complementary surface-sensitive techniques in their review, which we highly recommend [9]. In clear analogy with the conventional classification of the computational methods (see Section 3.1 and Figure 1), they categorized the experimental techniques according to the captured spatio-temporal scales. Similar to the perspective given by Bonitz et al. [1] (see Section 3.1 and Figure 2), they additionally proposed to organize the measurement methodology in three groups, corresponding to the probed spatial regions at the plasma-solid interface (see Figure 9). Note the resemblance with Figure 2. Next to that, *in situ* surface diagnostics are also growing in popularity for scrutinizing the synergetic mechanisms that underlie plasma catalysis [223]. This evidences the parallels between the modern trends of multiscale measuring and multiscale modeling for the investigation of plasma-surface interaction.

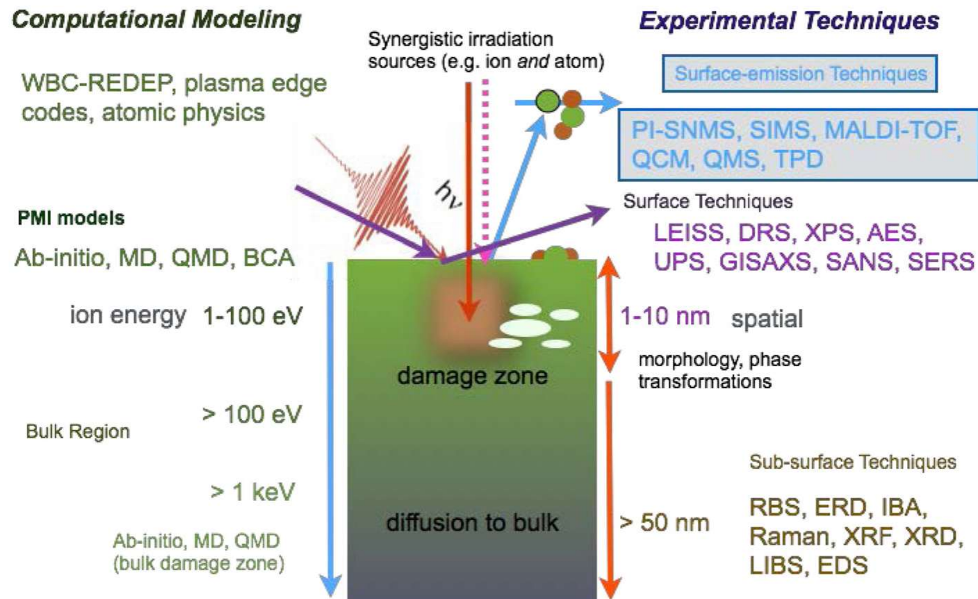

Figure 9. Scheme of the three regions considered by Allain and Shetty for (right) the classification of *in situ* and *operando* spectroscopy-based experimental techniques for the study of the plasma-surface interaction, (left) in comparison with computational methods. The energy and length scales indicate where the corresponding plasma-extracted ions implant and induce variation of the material atomic structure. The surface-emission techniques capture the emitted plume of ion-induced desorbed particles: post-ionization secondary neutral mass spectrometry (PI-SNMS), matrix-assisted laser desorption/ionization (MALDI-TOF), quartz crystal microbalance (QCM), quadrupole mass spectrometry (QMS), and temperature programmed desorption (TPD). The surface techniques examine only the upper layer of the solid material: low-energy ion scattering spectroscopy (LEISS), direct recoil spectroscopy (DRS), x-ray photoelectron spectroscopy (XPS), Auger electron spectroscopy (AES), ultraviolet photoelectron spectroscopy (UPS), grazing-incidence small-angle x-ray scattering (GISAXS), small-angle neutron scattering (SANS), and surface-enhanced Raman spectroscopy (SERS). The sub-surface techniques probe deeper towards the material bulk: Rutherford backscattering spectroscopy (RBS), elastic recoil detection (ERD), ion-beam analysis (IBA), Raman spectroscopy, x-ray fluorescence (XRF), x-ray diffraction (XRD), laser-induced ablation spectroscopy (LIBS), and energy dispersive spectroscopy (EDS). Republished with permission of IOP Publishing, Ltd, from J. Phys. D Appl. Phys. 50, 283002 (2017) [9]; permission conveyed through Copyright Clearance Center, Inc.

4. PLASMA ETCHING – FROM SCRATCHING THE SURFACE TO GOING IN DEPTH

4.1 The multiscale plasma etching model – one example to represent them all

4.1.1 The need for a bottom-up approach – message in a bottleneck

This Section illustrates the simulation strategy presented in Section 3 by means of the Hybrid Plasma Equipment Model (HPEM) and the associated Monte Carlo Feature Profile Model (MCFPM), both developed by the Kushner group for plasma etching and deposition. Although this illustration focuses on the example of plasma etching, the underlying reasoning and its consequences are relevant across all studies on plasma-surface interaction. More precisely, an accurate description of plasma-surface interaction requires both a macroscale analysis of the plasma and fundamental knowledge on the surface mechanisms. Up to now, simulations often omit the surface processes or treat them phenomenologically through trial-and-error procedures in a top-down approach. Such practice can be useful for initial estimations and in a first stage of numerical model optimization. However, at a certain point, a bottleneck may be expected in the modeling accuracy, where progress is hampered by a lack of fundamental insight on the surface mechanisms. A profound understanding of the fundamentals becomes inevitable at some point for further development. We believe that many plasma-surface interaction models, including these for plasma etching, are approaching that bottleneck stage. Throughout this Section, we demonstrate how the trial-and-error procedures in the top-down approach can be replaced with the careful implementation of quantitative microscopic data in a bottom-up approach, in order to overcome the bottleneck. Following this recommended strategy, computational models can be built with a superior predictive power. These models additionally allow a detailed analysis of the individual surface mechanism effects. Section 4.3 will evidence this with the example of SiO_2 etching by a CHF_3/Ar plasma.

Figure 10 displays the plasma etching process for microelectronics fabrication in a capacitively coupled plasma (CCP) reactor. The plasma is generated by applying RF power on a plane-parallel electrode system, where the wafer to be etched is placed on the bottom electrode. Depending on the wafer material, etching gas and operating conditions, various surface processes take place on the interface between the plasma and the wafer, as further discussed in Section 4.2. The ions play a decisive role in this surface chemistry, because they permit the anisotropic removal of wafer material, a highly preferred effect for microelectronics manufacturing. Deep trenches with a high aspect ratio can namely be formed this way, by covering parts of the wafer surface with a protective and less reactive mask. For this reason, plasma etching is preceded by a photolithography step, where a pattern is printed on a photoresist mask. The interdependence between the photolithography and plasma etching steps has become increasingly important in the race towards ever smaller dimensions of layered nanopatterns in microelectronics [224, 225]. Incorrectly aligned layers may lead to erroneous interlayer connectivity, resulting in yield loss. As such, the overall nanopatterning accuracy strongly depends on the wafer alignment, a critical metrology step during the lithographic procedure. Wafer alignment is done by measuring the position of alignment marks and overlay marks. These marks, however, get affected by the successive plasma etching stage. Since plasma etching has only been optimized for the product features, it performs sub-optimally for the mark patterns, which usually have a different size. This leads to mark asymmetries, which on their turn can cause substantial alignment deviations and interlayer overlay errors in the next lithographic step. To gain a deeper insight into the origin of the mark asymmetries induced by the plasma etching, we applied the multiscale modeling strategy on SiO_2 etching by a CHF_3/Ar plasma in a CCP reactor, using HPEM and MCFPM.

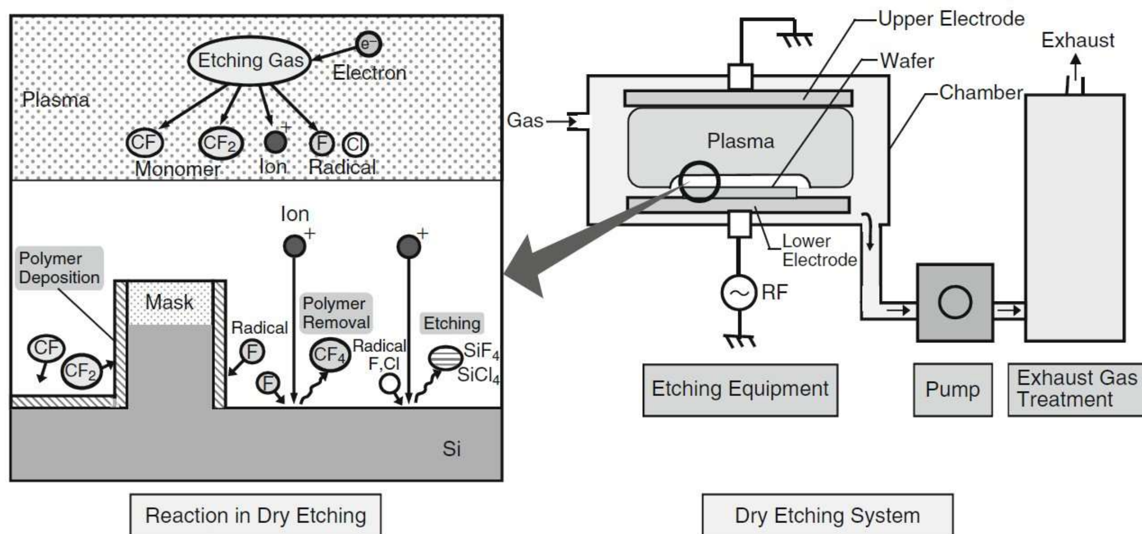

Figure 10. Overview of the plasma etching process in a CCP reactor. (left) Schematics of the surface chemistry at the substrate in a fluorocarbon plasma. (right) Reactor scheme with the active plasma gas. Reprinted by permission from Springer Nature: Springer eBook from Dry etching technology for semiconductors by K. Nojiri (2015) [226] © 2015.

4.1.2 Hybrid Plasma Equipment Model – example of a hybrid macroscale method

The working principle of HPEM has been thoroughly reviewed by Kushner in [47]. Hence, we will only give a brief summary. As a hybrid model (see Section 3.2.4), HPEM is composed of several modules, each of which deals with a certain aspect of the plasma. The three most essential modules are

- the electromagnetics module (EMM), where the electromagnetic fields are calculated from Maxwell's equations, e.g. based on the coil currents, material properties and plasma conductivity in the case of an inductively coupled plasma (ICP) reactor;
- the electron energy transport module (EETM), where the electron energy distribution function is obtained by solving Boltzmann's equation or its moments; and
- the fluid kinetics-Poisson module (FKPM), where the densities, momenta and temperatures of neutral and charged species are produced, as well as the electrostatic potential and field.

The FKPM provides the input data for the EEM and the EETM, and vice versa. Further, the plasma chemistry Monte Carlo module (PCMCM) is required to generate the input data for MCFPM, which operates as a separate KMC method (see Section 3.2.3 and further below) and which is thus used to simulate the etching progress on a mesoscale level. The input data for MCFPM consists of the fluxes and energy and angular distributions of the plasma species interacting with the wafer surface. In practice, the PCMCM is often activated only in the last iterations, since it is computationally intensive. All other modules are optional and their activation depends on the operational conditions, the desired accuracy and the available computational time.

Each module operates independently from how its necessary input data is produced. As such, the HPEM provides a flexibility to the user on how to calculate the different parameters. In the case of the EETM and the FKPM, for instance, the pressure is a decisive factor on the simulation procedure, as illustrated in Figure 11. At a pressure above 10 mTorr, the electron energy distribution can be

calculated in the EETM by means of a fast Boltzmann solver. This solver, however, is more likely to fail at lower pressures. Therefore, the electron Monte Carlo method is recommended below 10 mTorr, but it requires a much longer computational time. In the present study, only the latter setting was used, to obtain the highest accuracy.

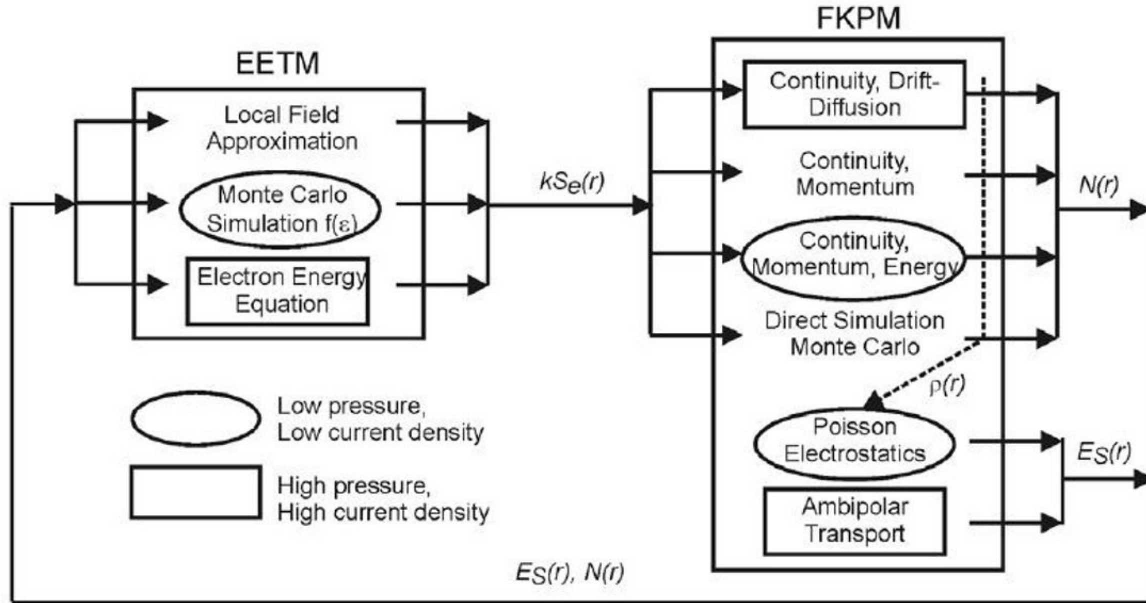

Figure 11. Paths through the EETM and the FKPM for (ellipses) a case operating at low pressure with low current density and (rectangulars) a case operating at high pressure with high current density. Republished with permission of IOP Publishing, Ltd, from J. Phys. D Appl. Phys. 42, 194013 (2009) [47]; permission conveyed through Copyright Clearance Center, Inc.

4.1.3 Plasma sheath module – example of a semi-analytical sheath method

Apart from the above mentioned essential modules, we also activated the analytical sheath module (ASM) in our simulations. Without it, a simplistic default sheath model is applied for the space charge region at the wafer surface, where the sheath thickness is approximated to be 5 times the Debye length. The ASM, on the other hand, replaces this default with a more realistic semi-analytical model (see Section 3.3.4 and Figure 12). These models produce output that is subsequently used in the EETM, in order to obtain a more accurate electron energy distribution. If none of them were implemented in the code, the sheath would namely be unresolved, causing an under- or overestimation of the sheath thickness at the different points in time during a voltage cycle (see Figure 12; the sheath thickness λ would then be taken equal to the cell width Δx). This leads to an artificial error in the electron heating as calculated by the EETM, resulting in an overestimated electron temperature [203]. The default sheath model with the thin sheath approximation partly compensates this error, but only to a limited degree, due to its simplicity. The analytical sheath model, in contrast, was proven to give a satisfactory agreement with experiments for usual conditions in an ICP reactor [203]. This is realized by adding a potential jump $\Delta\Phi_b(t)$ (i.e. the potential difference across the plasma sheath; see also ΔV in Figure 12) to the Poisson's equation in the FKPM at the plasma boundary, with $\Delta\Phi_b(t)$ obtained by the ASM based on the local plasma properties [47, 203]. As should be noted, each of the mentioned sheath models assumes a collisionless sheath, which generally is a fair approximation for usual etching conditions at pressures below 100 mTorr [227] and which offers a fast computational solution.

Realistic plasma sheaths are always collisional to a certain degree though, but their analytical assessment is generally not required under the usual operational conditions in plasma etching reactors [228]. More detailed information on the ASM can be found in [203].

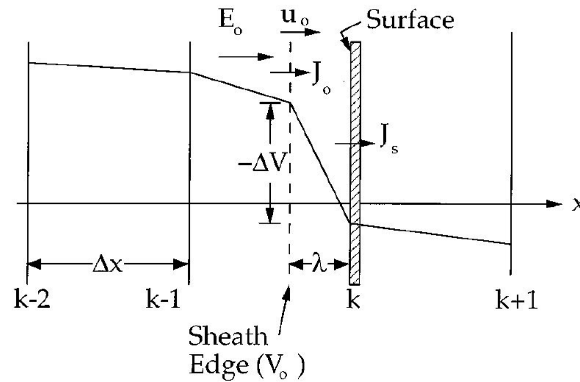

Figure 12. Schematic of the semi-analytical sheath model geometry in HPEM, where a potential jump ΔV is located over the sheath with thickness λ, which is thinner than the grid resolution defined by the cell width Δx. Values at the sheath edge are denoted by the subscript "0" and values at the wall surface by the subscript "s". Reprinted from J. Appl. Phys. 81, 569 (1997) [203], with the permission of AIP Publishing.

The sheath properties are not only crucial to the calculations of the electron energy distributions in the plasma volume, but also to the calculation of the ion energy and angular distributions (iEADs), that serve as input for MCFPM. Ions that leave the plasma volume through the sheath edge (see Figure 12) namely get accelerated by the sheath potential, which significantly alters their energy and angular distribution. Neutral species, on the other hand, are transported from the plasma to the wafer through diffusion. Next to that, the transport through the sheath is assumed not to change the particle fluxes.

4.1.4 Surface kinetics module – example of a deterministic description

Another optional module relevant to our case study is the surface kinetics module (SKM). This module simulates the particle exchange between the plasma volume and the wafer, i.e. the deposition and emission of plasma species, by means of a deterministic description (see Section 3.2.4). More precisely, it enables a first estimation of etching and deposition rates, and allows also to include the species originating from the wafer surface in the plasma gas chemistry. In this way, HPEM can make a more detailed account of the chemical processes in the plasma volume, as well as the boundary conditions at the wafer surface. For its operation, the SKM requires a user-defined surface chemistry set for the reactions at the wafer surface. In practice, this is often the same surface chemistry set as the one used in MCFPM, or alternatively a reduced version of it. More detailed information on the SKM can be found in [229].

4.1.5 Monte Carlo Feature Profile Model – example of a kinetic Monte Carlo method

MCFPM simulates the etched profile at a radial location on the wafer on the mesoscale. The wafer is subdivided in small blocks, each filled with a certain material. In this case study, the 2D version of MCFPM has been used, with a cell size of 0.5 nm x 0.5 nm. For comparison, the cubic Si unit cell

containing 8 atoms has an edge length of 0.543 nm. In other words, the MCFPM simulations are performed close to the atomic limit. MCFPM uses the following input:

- the fluxes, as well as the energy and angular distributions (EADs) of the gaseous neutral and ionic species bombarding the wafer, i.e. HPEM output;
- a user-defined surface chemistry set, including all surface and gas species; and
- a user-defined initial feature shape.

Its working principle is depicted in Figure 13. During every iteration, a user-defined number of super-particles is released towards the wafer surface (see Section 3.2.3). The number of real particles in a computational particle is chosen equal to the mesh cell content in our simulations. The identity of each super-particle is determined by the code in a pseudo-random manner, based on the relative ratios of the fluxes. The computational particle is released with an energy and under an angle corresponding to its EAD given in the input file. When the super-particle reaches a cell filled with material, the orientation of the surface plane of the material is calculated, depending on which of the neighboring cells is filled with material or not. Accordingly, the code obtains the incident angle, which is required to calculate the reaction probability with the interacting surface group. By means of the surface chemistry set, the code decides whether the particle reflects, adsorbs, etches the surface group away or replaces it with another group. Depending on the outcome, the feature shape is updated and new super-particles may be emitted from the surface. In the case of reflection beyond a critical angle, the emission angle is specular. Other reflected particles, as well as desorbed or etched species, on the other hand, are released symmetrically according to a modified Lambertian angular distribution, which agrees with thermal desorption. The modified Lambertian distribution prevents emission under an angle beyond a user-defined value, in order to account for surface roughness and non-thermal desorption effects. As should be noted, the modified Lambertian distribution is symmetric around the surface normal. This simplification contradicts the observed ion-induced inclined species emission observed in several fundamental studies (see e.g. [230-233]). This may induce deviations in the etched feature profile, but even so, MCFPM has shown good agreement with experiments under usual plasma etching conditions (see Section 4.1.6). After each interaction, new super-particles are released and the algorithm is repeated until all iterations have been finalized.

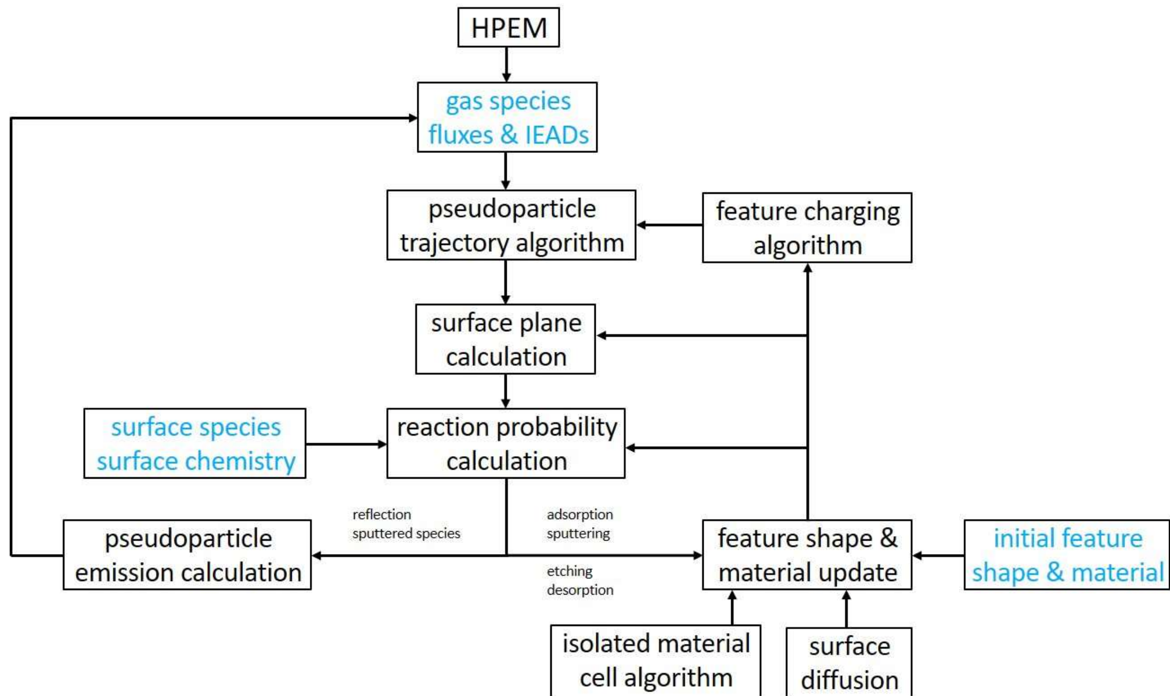

Figure 13. Overall MCFPM structure and principle, as explained in the text. Input data is indicated in blue. The isolated material cell algorithm removes or relocates cells which do not have any surrounding material. The surface diffusion algorithm simulates the diffusion of certain groups over the surface. The feature charging algorithm modifies the trajectory and energy of charged gas species according to the electric field from the deposited charge on the surface. The latter two were disabled in the case study of Section 4.3.

4.1.6 Experimental benchmarking of the working principle – examples of multiscale measuring

Both HPEM and MCFPM have a broad applicability, as they can simulate the etching or deposition process for a wide range of operating conditions, including different gas mixtures and wafer materials. Moreover, their various settings provide a high flexibility in the use of their algorithms. The development of the models by the Kushner group can be traced back to the early 1990's [234], which enabled the extension and optimization of the code, as well as its benchmarking with multiple experimental investigations. For these reasons, the models have found a widespread application in plasma etching and deposition studies. As should be noted, the experimental benchmarking can be performed on the level of the user-defined gas and surface chemistry sets, as well as on the level of the general codes. The first option will be illustrated in Section 4.3 for SiO_2 etching by CHF_3/Ar plasma.

The second option corresponds to verifying the general working principle of the models, independent of possible errors or inaccuracies in the chemistry sets. Ideally, this could be realized by directly comparing the energy and angular distributions of the ions incident on the wafer surface between the simulations and the experiments. These distributions are namely relatively insensitive to the used chemistry sets, in contrast to, for instance, the incident particle fluxes and the etch or deposition rates. In the early years of HPEM, such benchmarking was indirectly performed by means of the etched profiles. However, the ion energy distributions cannot readily be verified in this way, since the surface chemistry set translates them into etch yields that can be manipulated by the user. On the other hand, the ion angular distributions determine the average etching direction and thus the slope of etched

trenches, in a rather independent manner from the user-defined gas and surface chemistry sets. Such manifestations of etch asymmetry therefore form an elegant benchmarking criterion for the HPEM and MCFPM codes. The investigations by the Kushner group in [235-237] indeed demonstrate that the combination of HPEM and MCFPM can reproduce asymmetries in the etched profiles to a satisfying degree.

In the past decade, the Kushner group continued the experimental benchmarking of HPEM in a more direct way. In a first study using a capacitively coupled discharge in hydrogen [238], the normalized ion energy distribution function of H_3^+ was experimentally obtained and compared with the HPEM simulation output (Figure 14(a)). Although the results did not permit a conclusive interpretation, the experimental energy distribution curve agreed well with the curve of the HPEM simulation restricted to the incident ion angular interval between -15° and +15°. In a second study on capacitively coupled discharge in argon [239], a satisfactory quantitative agreement was found between the simulated Ar^+ energy distributions and the ones experimentally obtained from ion current profiles with respect to discrimination potential, as measured with a Semion radio frequency ion energy analyzer in an independent investigation [240] (Figure 14(b)-(c)). In a third study on an Ar/O_2 inductively coupled plasma, simulated and experimental Ar^+ energy and angular distributions were compared over a full RF cycle, as shown in Figure 15. A remarkable qualitative correspondence can be noted, for both the energy and angular components. This confirms that the HPEM is based on assumptions that describe the underlying physics very well.

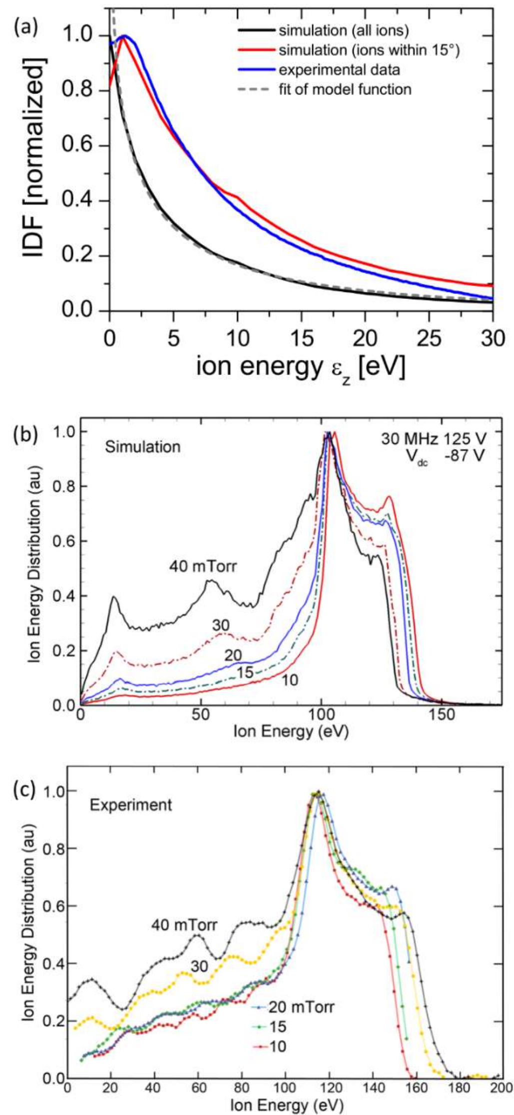

Figure 14. Simulated and experimental incident ion energy distributions in two CCP reactors. (a) Normalized ion energy distribution function of H_3^+ obtained experimentally, by the HPEM simulation, and in an analytical model. In the simulation, the entire angular distribution function (black curve) or all ions within an incident angle of 15◦ (red curve) are evaluated. The pressure was 200 Pa and the applied voltage 200 V. (b) Simulated and (c) experimental energy distributions of Ar^+ for an Ar CCP with pressure varying from 10 to 40 mTorr. Power was varied to provide a constant DC self-bias voltage of -87 V for each condition. The experimental distributions were obtained from ion current profiles with respect to the discrimination potential, as measured with a Semion radio frequency ion energy analyzer. (a) Republished with permission of IOP Publishing, Ltd, from Plasma Sources Sci. Technol. 23, 015001 (2013) [238]; permission conveyed through Copyright Clearance Center, Inc. (b) Reprinted from Low Temperature Plasma Etching Control through Ion Energy Angular Distribution and 3-Dimensional Profile Simulation by Y. Zhang (2015) [239] with permission from Dr. Yiting Zhang. (c) © 2014 IEEE. Reprinted, with permission, from IEEE Trans. Plasma Sci. 42, 1880 (2014) [240].

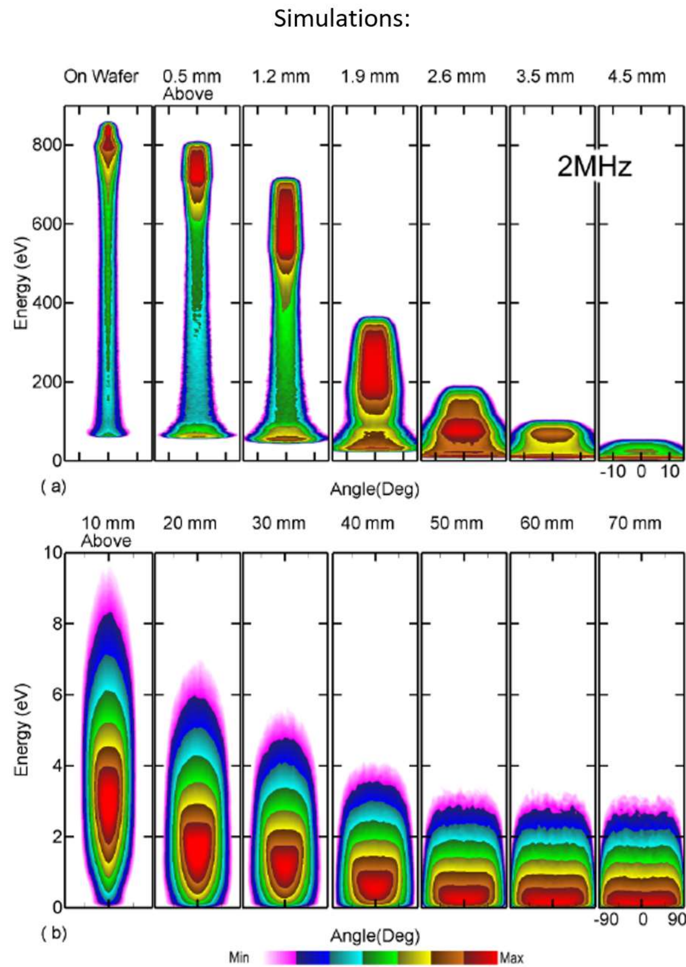

Experiments:

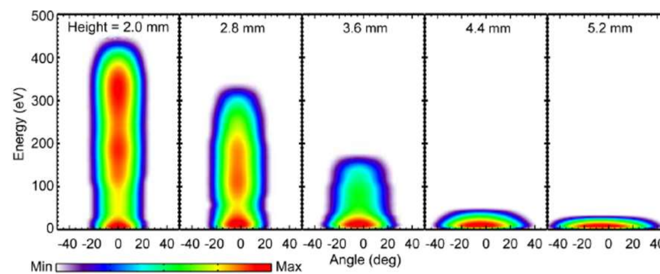

Figure 15. (top) Simulated and (bottom) experimental energy and angular distributions for Ar^+ integrated over a full RF cycle, in an Ar/O_2 inductively coupled plasma at a gas ratio of 80/20. The experimental distributions were measured by means of laser induced fluorescence of Ar^+. The operational conditions are slightly different for the computational and experimental results (computational: 2 mTorr, 480 W, with a frequency of 2 MHz, RF bias of 500 V and DC bias of -400 V; experimental: 0.5 mTorr, 480 W, with a frequency of 2.2 MHz, RF bias of 300 V and DC bias of -300 V). Reprinted from Low Temperature Plasma Etching Control through Ion Energy Angular Distribution and 3-Dimensional Profile Simulation by Y. Zhang (2015) [239] with permission from Dr. Yiting Zhang.

4.1.7 Reactor geometry and operating conditions – example of a case study

In our case study, a CCP reactor scheme was developed, based on a Leybold F2 reactor from TU Delft (see Figure 16), used for the experimental benchmarking of the surface chemistry set in Section 4.4. This is a single frequency 13.56 MHz reactive ion etching (RIE) reactor with a chamber diameter of 36 cm, an upper electrode diameter of 25 cm, a lower electrode diameter of 20 cm, a lower ring diameter of 25 cm and an interelectrode distance of 7.5 cm. Next to that, a $CF_4/CHF_3/Ar$ gas chemistry set was constructed based on the Ar chemistry presented in Table S1 of the Supplementary Material with rate coefficients from [241] and the $CF_4/CHF_3/H_2$ reactions of a complete $CF_4/CHF_3/O_2/H_2/Cl_2/HBr$ set that was previously developed in PLASMANT [242]. Since Ar is an inert species, no additional cross-reactions were taken into account. The operating parameters applied in the experiments and simulations are listed in Table I.

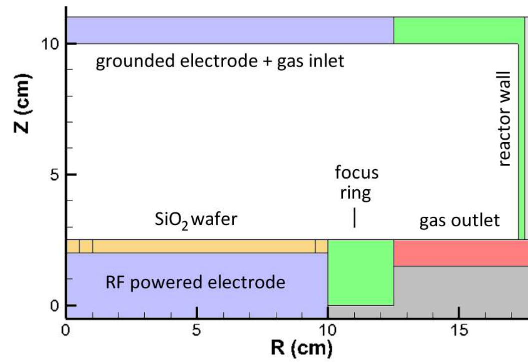

Figure 16. Reactor scheme of the axisymmetric Leybold F2 reactor, where the Z-axis serves as the symmetry axis.

Table I. Operating conditions of the Leybold F2 reactor used for the experiments and simulations of the case study.

Parameter	**Value**
Applied power (W)	75
Frequency (MHz)	13.56
Self-bias voltage (V)	700
Pressure (mTorr)	22.5
Gas ratio CHF_3/Ar	15/45
Wafer temperature (K)	293
Gas flow (sccm)	60
Relative permittivity of focus ring	3.6

4.2 How to implement the surface processes – example of atomistic modeling and measuring data

4.2.1 Elementary plasma-surface mechanisms – simplicity is the ultimate sophistication

Plasma-surface interaction is a complicated phenomenon, hosting a multitude of contributing processes. These processes can be distinguished into two groups: single particle interactions and mesoscale effects of a more collective nature. The first group consists of individual events involving one incident plasma particle, such as sputtering, implantation, adsorption, desorption, or another type of surface reaction. Examples of the second group are surface amorphization and nanoscale pore formation, phase transitions and associated surface deformation, as well as secondary processes like the diffusion of surface species or their drift under influence of Coulomb interactions. Under usual conditions in plasma etching, these collective effects play a minor role and therefore may often be disregarded in a first approximation. Melting can only take place when a large enough heat flux is delivered to the material by the plasma, relative to the melting temperature and heat conductivity. This requires intense ion bombardment, with ion fluxes and energies atypical for plasma etching reactors. The diffusion and drift of surface species, as an exception, can be important for processes relevant to plasma etching, depending on several factors, including the type of adsorption taking place (chemisorption versus physisorption), the porosity of the surface, the species under consideration, the surface conditions and the local electric field [243-245].

Surface amorphization might take place already at relatively low ion energies. Ar^+ ions, for instance, induce an amorphous layer in Si with a depth of two monolayers at 125 eV, which grows to a depth of 1 nm at 250 eV [246]. In contrast, a GaAs surface does not lead to amorphization under the same circumstances, illustrating the strong material dependence of this effect. Although amorphization appears a complicating and undesirable effect on first sight, it actually allows a useful simplification in the multiscale modeling strategy. It namely diminishes any anisotropy in the upper layer of the surface material, eliminating the need to take this anisotropy into consideration. For a surface with a crystalline structure, the lattice orientation namely strongly determines the reaction probabilities for many incident plasma species [247, 248]. When ions amorphize the surface, on the other hand, the underlying lattice does no longer influence the surface interactions. A universal set of single particle interactions can then be developed for the surface material, irrespective of the initial atomistic structure orientation. The elemental composition and bonds in the upper surface layer, however, regulate the interaction outcome. For this reason, single particle interactions may be understood as a reaction between the plasma particle and a specific surface group. With each interaction, the surface group can be modified, removed or covered, leading to another group being exposed to the incident plasma species.

Using this description, we will distinguish five types of elementary plasma-surface interaction mechanisms, as illustrated in Figure 17:

- physical sputtering, where inert ions remove surface groups without adding new elements to the surface,
- direct reactive ion etching, where reactive ions both remove surface groups and add new elements to the surface,
- chemical etching, where reactive neutrals bind to the surface and subsequently form volatile molecular species to be emitted into the gas phase,
- deposition, where plasma particles bind to the surface without autonomously forming volatile species, and
- ion-assisted or ion-enhanced chemical etching, where neutral species first attach to the surface and an incident ion subsequently aids in the removal of surface material.

More detailed information on these mechanisms can be found in a few reviews and several other papers, e.g. [10-12, 249-252]. In the following, we will focus on a few important aspects.

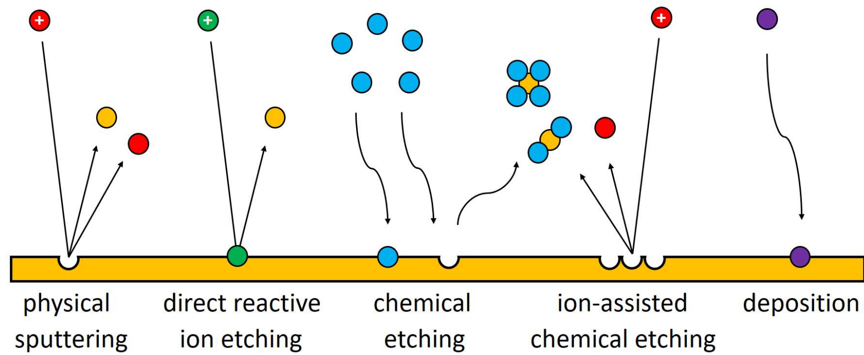

Figure 17. Illustration of the five main elementary surface processes considered in the case study.

The interaction of an energetic ion or hot neutral with the surface is often described with the hot spot model. According to this model, the kinetic particle deposits its energy in a small area of the surface, causing a local, rapid, extreme and short-living temperature increase. This high temperature enables surface reactions with a high activation energy, which do not take place or only very slowly under standard conditions. This explains the underlying physics of ion-assisted chemical etching. A stable molecular species can, for instance, first attach to the surface by physisorption and afterwards react with the surface under influence of an ion. This reaction may produce new volatile molecular species, containing surface material, which can be readily emitted into the gas phase. This physico-chemical effect has been confirmed for ion-assisted chemical etching of GaN with and without a Cl-adsorbed layer by incident Ar^+ ions in a series of MD simulation studies by Harafuji and Kawamura (see e.g. Figure 18) [253-257]. The hot spot model can also explain direct reactive ion etching. However, we believe that the latter is an often misunderstood mechanism, due to its inherent complexity.

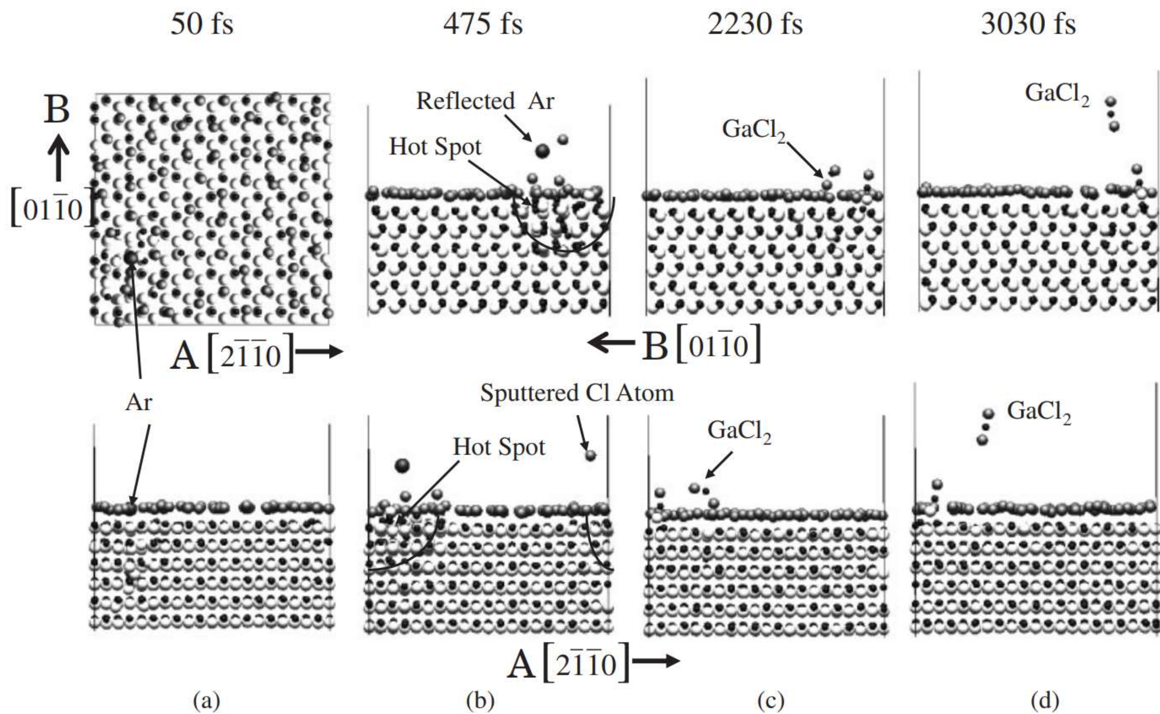

Figure 18. Snapshots of the top and side views of the interaction between an Ar^+ ion with 150 eV energy and a GaN substrate with a layer of adsorbed Cl atoms, at normal incidence for (a) 50, (b) 475, (c) 2230, and (d) 3030 fs after the first contact. The interaction causes Cl sputtering, hot spot formation

and the emission of a $GaCl_2$ molecule. The last frame also shows another Ga-Cl product attempting to leave the surface, but unable to overcome the surface barrier. Reprinted with permission of IOP Publishing, Ltd, from Jpn. J. Appl. Phys. 49, 08JE03 (2010) [253]. Copyright 2010 The Japan Society of Applied Physics.

As an example, consider direct reactive ion etching of Si by means of an F^+ ion beam. F^+ ions simultaneously sputter and fluorinate a Si surface, resulting in a higher etch yield. Figure 19(a) compares their etch yield with the one of Ne^+ ions. Ne^+ ions are inert and have a mass similar to F^+, which makes their etch yield representative for the physical sputter component in the one of F^+. In other words, the difference between the etch yield of F^+ and Ne^+ can be understood as the chemical sputter component. According to the experimental results in Figure 19(a), this difference agrees well with the measured SiF_4 emission. The formation of SiF_4 at the Si surface is, however, unlikely. F atoms at the fluorinated surface namely get more easily sputtered than Si atoms, due to their lower mass. The F sputter yield by F^+ ions from a SiF_2 surface group at 500 eV is, for instance, beyond 2 atoms per ion (see Figure 19(b)). As such, SiF_3 surface groups, and thus SiF_4 molecules, are not easily formed with F^+ irradiation alone. SiF_4 formation can therefore not explain the chemical component in the sputter yield of F^+.

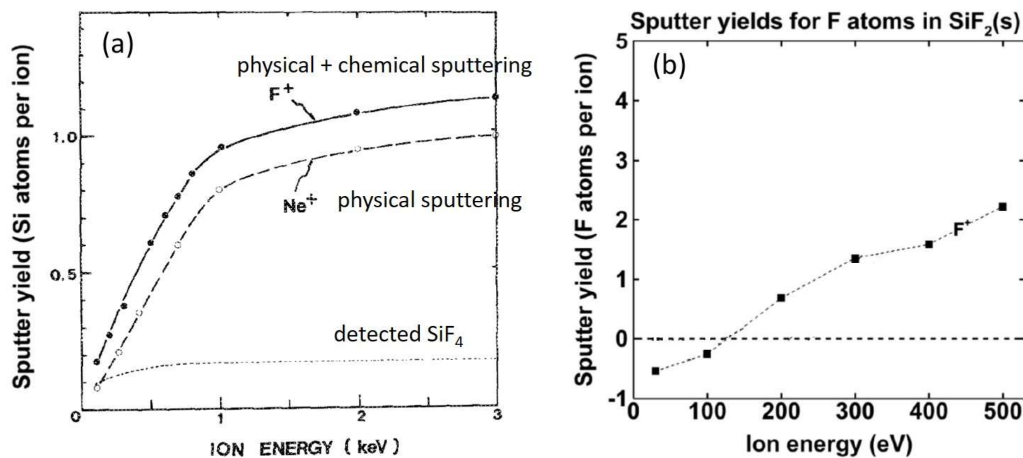

Figure 19. Sputter yield of (a) Si and (b) F atoms from a Si surface irradiated with F^+ ions. In (a), also the sputter yield by Ne^+ and the measured SiF_4 emission are shown. (left) Reprinted with permission from J. Vac. Sci. Technol. B: Microelectron. Process. Phenom. 4, 459 (1986) [250]. Copyright 1986, American Vacuum Society. (right) Adapted with permission from J. Phys. Chem. C 118, 30315 (2014) [258]. Copyright 2014 American Chemical Society.

Instead, the chemical component is due to weakening of bonds between SiF_x groups and the Si lattice during fluorination. As explained in Figure 20, $Si_{(s)}$ and $SiF_{(s)}$ are attached to the surface with approximately an equal bond strength, whereas $SiF_{2\,(s)}$ and $SiF_{3\,(s)}$ experience a weaker attachment. The latter two groups are therefore more easily sputtered from the surface. This explanation is in agreement with the individual sputter yields for each surface group, as obtained in the molecular dynamics study by Tinck et al. [258] (see Figure 21(a)). The sputter yield of $Si_{(s)}$ and $SiF_{(s)}$ approximately coincides with the physical sputter yield by Ne^+ ions, indicating the same etching mechanism, i.e. physical sputtering. The sputter yield of $SiF_{2\,(s)}$ and $SiF_{3\,(s)}$ is roughly twice as high, confirming that their binding strength is a decisive factor. The presence of the latter two surface groups therefore increases the overall sputter yield. This increase depends on the percentage of $SiF_{2\,(s)}$ and $SiF_{3\,(s)}$ groups covering the surface, which can be calculated from the individual sputter yields for each surface group by means

of a deterministic description (see Section 3.2.4). We have performed such calculation, starting with an initial surface coverage percentage of 25% for each group and using incremental surface group changes on the total surface of 10% during each iteration. The results are shown in Figure 21(b) (i.e. the red curve (2)). The calculated overall sputter yield at steady state agrees fairly well with the experimental data for F^+ ions bombarding a Si substrate, which include both the physical and chemical sputter components.

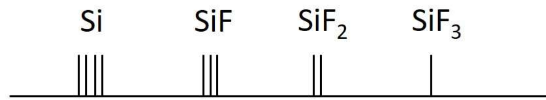

Figure 20. Schematics of the bonds between a Si substrate and (from left to right) a $Si_{(s)}$, $SiF_{(s)}$, $SiF_{2\ (s)}$ and $SiF_{3\ (s)}$ group. The unfluorinated Si atom is attached to the material with three strong Si-Si bonds and a weak one, making its total bond strength approximately equal to the one of the SiF group. The $SiF_{2\ (s)}$ group is attached less strongly to the surface due to its lower number of bonds. The single bond of $SiF_{3\ (s)}$ makes it the most weakly bound surface group of the four.

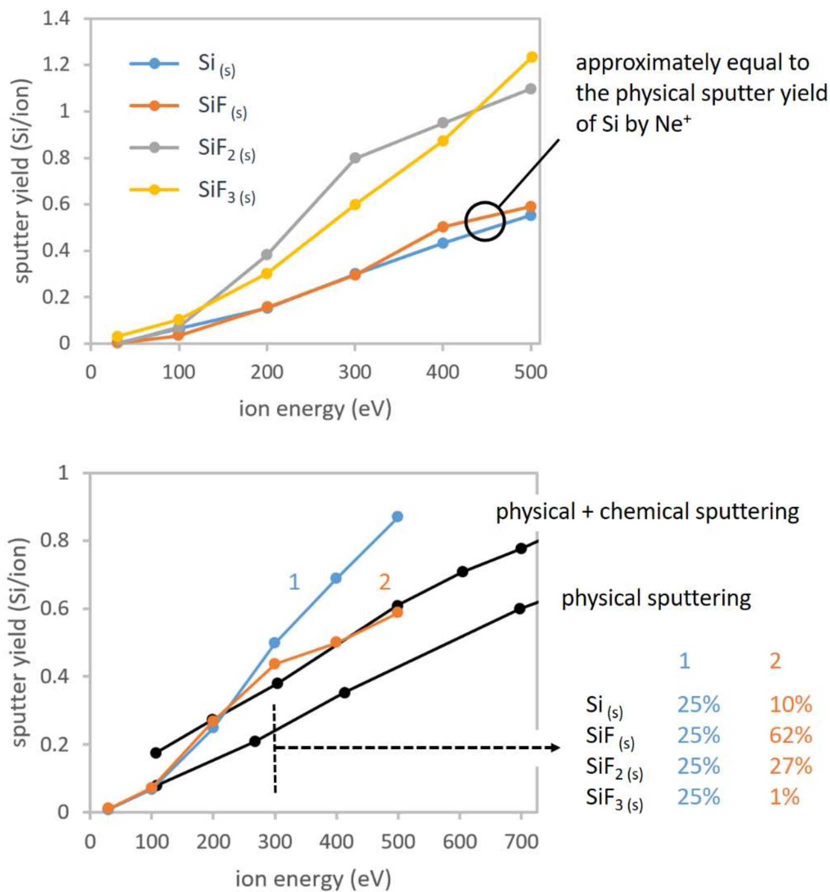

Figure 21. Si sputter yields for F^+ ions incident on a Si substrate. (a) Output data from repeated molecular dynamics simulations, where the initial surface is composed of one surface group type in each simulation, as indicated in the legend. Data taken from [258]. (b) Comparison of (black) the experimental data in Figure 19(a) with (blue and red) the calculated total sputter yield by F^+ ions of a surface composed of the four SiF_x surface groups, each covering the surface with a certain percentage. The blue curve (1) and red curve (2) correspond to the initial conditions and calculated results of the

deterministic description, as explained in the text. The surface fractions at an ion energy of 300 eV are mentioned in the legend.

In other words, the chemical component in the sputter yield of F^+ is due to the weaker Si-Si bonds at the surface caused by the deposited F^+ ions. This mechanism has, to our knowledge, not been explicitly proposed in literature before as the general underlying working principle of direct reactive ion etching. It, however, lies very well in line with the MD simulated output and its interpretation by Tinacba et al. [259] and the MD simulation data by Ohta and Hamaguchi [260], as presented in Figure 22. Its validity over various combinations of incident reactive ions and substrate materials suggests that it is indeed universal in nature. We will apply this insight in Section 4.2.2 for the implementation of radical-emitting ion reactions in a surface chemistry set. In contrast, molecule-emitting ion reactions provide a higher etch yield due to the weaker physisorption strength in comparison to chemisorption.

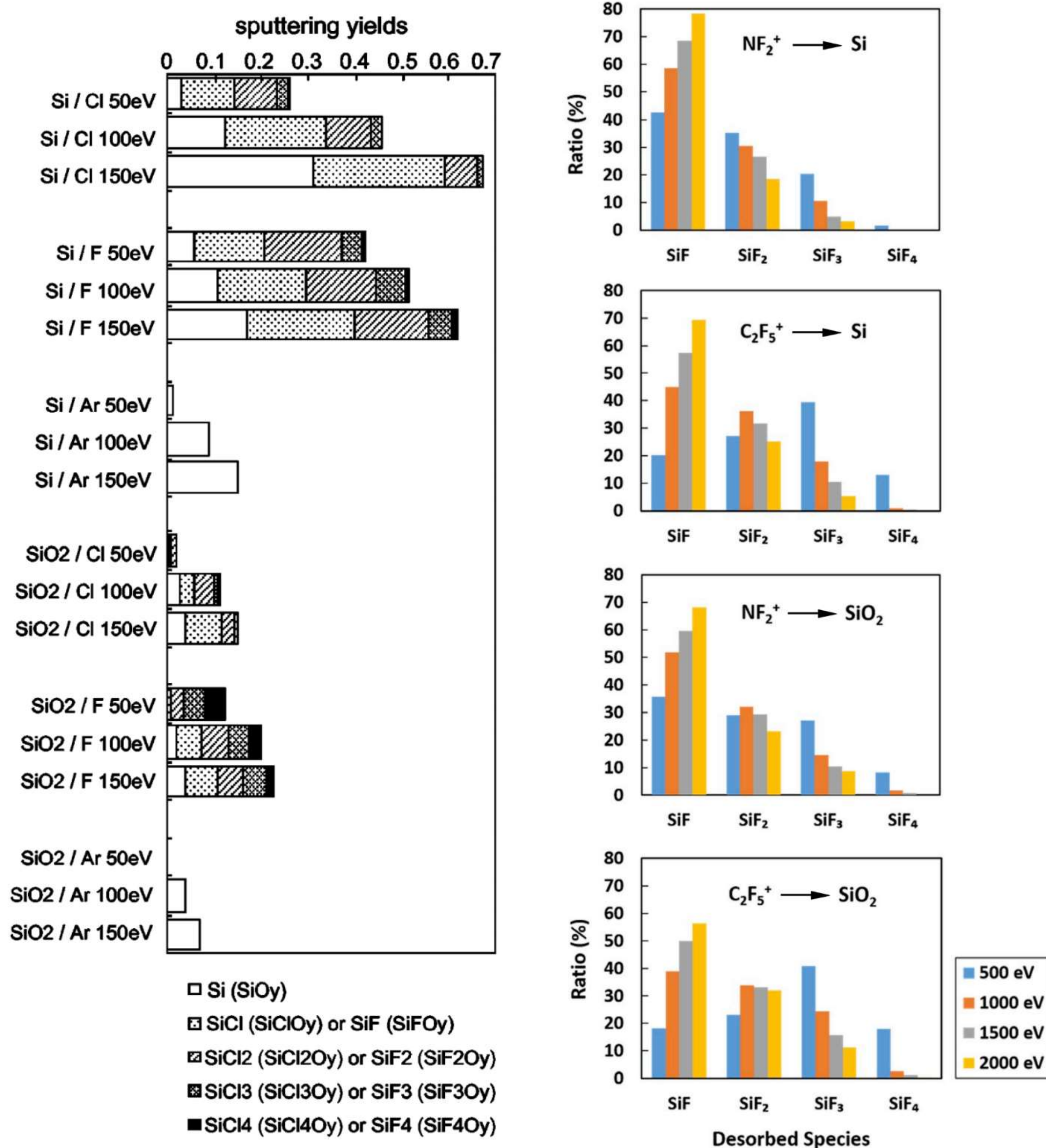

Figure 22. Ratios of the sputtering products in various direct reactive ion etching reactions, according to two MD studies. Before each simulation, the substrate surface was prepared to represent the situation under steady state. The conditions are indicated as (left) Y / X and (right) X → Y, where X stands for the incoming ion and Y for the substrate. (left) Reprinted with permission from J. Vac. Sci. Technol. A: Vac. Surf. Films 19, 2373 (2001) [260]. Copyright 2001, American Vacuum Society. (right) Reprinted from Surf. Coat. Technol. 380, 125032 (2019) [259], Copyright 2019, with permission from Elsevier.

4.2.2 Design of the surface chemistry set – a mosaic of quantum data

In this section, the surface chemistry set design for Si and SiO_2 etching with CF_4/CHF_3/Ar is described in four parts:

1. Si etching with CF_4/Ar
2. SiO_2 etching with CF_4/Ar
3. Introduction of H-containing species
4. Etching of the photoresist

The first part serves as a basis for the construction of the second part. Although both subsets now belong to the same composite set, they can largely be seen as isolated parts, as there are only a few reactions connecting both. The complete surface chemistry set is presented in Table S2 of the Supplementary Material.

Each subset is designed according to the following general principles:

- All material cells in the wafer, including the cells with surface groups, consist of 10 atomic or molecular units each. For instance, a Si cell and a CF_x cell contain 10 Si atoms and 10 CF_x molecules, respectively. This allows the removal of up to 10 atomic or molecular units by an incident species, which is especially necessary for ion-assisted chemical etching reactions with an etch yield larger than 1.
- Plasma species originating from the gas phase or reflecting from a surface consist of only one atomic or molecular unit.
- However, gaseous etch products are made up of 10 units each, as material cells can only be etched in their entirety. This reduces the computational time.
- Accordingly, the physical etch yield of the gaseous species needs to be divided by 10 to obtain the computational reaction probability, unless if they contain 10 units of the species. In the remainder of this review, the mentioned values of the etch yield and reaction probabilities will always refer to the physical ones, in order to avoid confusion.
- Some plasma species with a very low flux relative to the other species are not considered in the surface chemistry. More specifically, the influence of C, CH, CHF, CHF_2, F_2, C^+, H^+, F^+, CHF^+, F_2^+ on the overall surface chemistry can be neglected, as their low fluxes immediately reveal (see Section 4.3), but etch products of the same kind were kept included. In fact, this approximation cannot be avoided, as MCFPM only allows a limited flux range for the incoming particles. Still, a few low flux species, such as C, F_2, F^+ and F_2^+, have not been removed from the chemistry set for educational purposes.
- When an ion reflects at a surface cell, it transforms into a hot neutral, which is considered chemically equivalent to the ion.

- Neutral species react with a fixed reaction probability. Ions, on the other hand, have an angle- and energy-dependent reaction probability, given by the equation

$$p(E_i)f(\theta_i) = p(E_{ref})\frac{(E_i - E_{th})^a}{\left(E_{ref} - E_{th}\right)^a}f(\theta_i)$$

  Here, $f(\theta_i)$ is the angular dependence normalized at incidence perpendicular to the surface, and $p(E)$ is the reaction probability calculated by MCFPM from the incoming ion energy E_i at normal incidence, the threshold energy E_{th} of the reaction, a user-defined reference energy $E_{ref} > E_{th}$, the reaction probability $p(E_{ref})$ at this energy and an exponent a. E_{th}, E_{ref}, $p(E_{ref})$, a and $f(\theta_i)$ can be separately defined for every reaction in MCFPM. Exceptions are deposition reactions, implemented with the linearly decreasing function

$$p(E_i) = p_0\frac{(E_{th} - E_i)}{E_{th}}$$

  where p_0 is the reaction probability at 0 eV. This function can also be applied in ion reactions competing with etching in a certain energy interval.
- Where it was not possible to find exact quantitative data in literature for a reaction, its mechanism and reaction probability has been deduced from a similar reaction, based on the comparison of the dissociation energies of the broken and produced bonds. The values of the dissociation energies mentioned below are based on the list in [261].

The neutral gaseous species have three functions: they can (i) get deposited on the surface, (ii) contribute to ion-assisted chemical etching or direct reactive ion etching, or (iii) chemically etch away a surface group by forming a volatile molecule (e.g. CF_4 or SiF_4). The chemistry set does not distinguish between the functions (i) and (ii), in the sense that ion-assisted chemical etching and direct reactive ion etching are generally preceded by the formation of a surface group through the deposition of a neutral species. Function (iii), however, is implemented in the set with the immediate release of the volatile molecule. As should be noted, this stands in contrast with the often made assumption in literature that ion-assisted etching includes the removal of volatile molecules at the surface. With the neutral species N incident on a surface group $S_{(s)}$, we thus get the following types of surface reactions:

i. Deposition: $S_{(s)} + N \rightarrow S_{(s)} + N_{(s)}$ or $S_{(s)} + N \rightarrow SN_{(s)}$
ii. Ion-related reactive etching: (i) followed by $N_{(s)} + I^+ \rightarrow N + I$ or $SN_{(s)} + I^+ \rightarrow SN + I$
iii. Chemical etching: $S_{(s)} + N \rightarrow SN$

where I^+ represents an ion and the index (s) identifies a surface group.

The incident ions, as well as the hot neutrals, also have three functions: they can (iv) get deposited on the surface, (v) remove radicals from the surface by physical sputtering, or (vi) result in the release of volatile molecules by ion-assisted chemical etching or direct reactive ion etching. In some cases, functions (v) and (vi) occur with the partial deposition of the ion or hot neutral. With the ion I^+ incident on a surface group $S_{(s)}$, we thus get the following types of surface reactions:

iv. Deposition: $S_{(s)} + I^+ \rightarrow S_{(s)} + I_{(s)}$ or $S_{(s)} + I^+ \rightarrow SI_{(s)}$
v. Physical sputtering: $S_{(s)} + I^+ \rightarrow S + I$ or $S_{(s)} + I^+ \rightarrow SI$
vi. Ion-related reactive etching: same as (v), where S or SI represents a molecule instead of a radical

Note that the physical sputtering (v) requires the breaking of a chemical bond with the surface, whereas reaction (vi) produces a volatile molecule, which is emitted by overcoming a much weaker van der Waals interaction. Therefore, the reaction probability of (vi) is readily one order of magnitude higher than the one of (v). For (v) and (vi), the formula mentioned above is used for the reaction probability.

Table II. The plasma species, reactive etch products and surface groups considered in the surface chemistry subset of Si etching with CF_4/Ar. PR $_{(s)}$ stands for the photoresist. Incident species only contain one atomic or molecular unit. The etch products, on the other hand, consist of 10 units, and are therefore treated by the chemistry set in a separate way (see text).

Neutral incident species	Incident ions	Chemically active gaseous etch products	Surface groups
CF_4	Ar^+	CF_4	$CF_{4\,(s)}$
CF_3	CF_3^+	CF_3	$CF_{3\,(s)}$
CF_2	CF_2^+	CF_2	$CF_{2\,(s)}$
CF	CF^+	CF	$CF_{(s)}$
C	F^+	C	$C_{(s)}$
F	F_2^+	SiF_4	$SiF_{4\,(s)}$
F_2		SiF_3	$SiF_{3\,(s)}$
		SiF_2	$SiF_{2\,(s)}$
		SiF	$SiF_{(s)}$
		Si	$Si_{(s)}$
			$PR_{(s)}$

<u>The subset focusing on Si etching with CF_4/Ar</u> considers seven neutral incident species, six ions, ten chemically active gaseous etch products and eleven surface groups (see Table II). Its reaction probabilities were taken from literature or estimated as follows:

Neutral gas species

1. Si deposition on $Si_{(s)}$ takes place with a probability of 1, in agreement with [258, 262].
2. SiF_x deposition on $SiF_{y\,(s)}$ has reaction probabilities based on the data in the MD study of [258]. In many cases, exact values are not available, as the MD simulations only provided a lower limit. MD simulations can namely only access short time scales at which the immediate reaction of a gaseous species can be determined. In practice, however, the species can remain at the surface due to physisorption, for a much longer time than the one accessible in the simulations. Therefore, the reaction probabilities have been estimated from the lower limits and the comparison between the binding energy of the broken and formed bonds. In general, the reaction probability decreases for an increasing number of F atoms (higher x and y), because of the steric hindrance they cause for the reaction site.
3. The values obtained in the previous step were used to estimate the reaction probabilities for SiF_x deposition on $CF_{y\,(s)}$ groups, by comparing the binding energies of the broken and formed bonds. Since the formed C-Si bonds are generally stronger than Si-Si bonds, and the broken C-F bonds weaker than Si-F bonds, the values were estimated higher than the ones of the previous step.

4. Analogously, the probabilities of CF_x deposition on $SiF_{y\,(s)}$ and $CF_{y\,(s)}$ groups were determined from the values in steps 2 and 3, taking into consideration the involved energies of the broken and formed bonds.
5. Exceptions are the reactions with y = 4, whose probabilities were assumed zero. For x = 4, no chemical bonds are broken nor formed, but the molecule can attach to the surface by physisorption. The likeliness of such attachment was estimated based on the desorption energies calculated in [258].
6. The deposition probabilities of F and F_2 on $SiF_{y\,(s)}$ were also taken from [258].
7. In [263], the production probability of SiF_4 per 4 incident F radicals has been estimated to range between 0.02 and 0.1, based on different sources in literature. If we assume a value of 0.06, this implies an overall reaction probability of 0.015 per incident F. Since this process consists of 3 successive deposition events of an F atom, followed by the removal of SiF_4 by a fourth radical, the probability of the latter reaction can be deduced from the probabilities determined in step 6. For F_2, the probability of the corresponding reaction is assumed to be double that value. As should be noted, these SiF_4 emitting reactions do not exclude the independent reaction $SiF_{3\,(s)} + F \rightarrow SiF_{4\,(s)}$ of step 6 where the molecule remains physisorbed at the surface. To retain the analogy between the reactions with incident F and F_2, the counterpart for F_2 was assumed to be $SiF_{3\,(s)} + F_2 \rightarrow SiF_{4\,(s)}$ with a doubled reaction probability.
8. The deposition probabilities of F and F_2 on $CF_{y\,(s)}$ and the emission probability of CF_4 by chemical etching with F and F_2 were deduced from the results of steps 6 and 7. Since Si-C (435 kJ/mol) and C-C (~450 kJ/mol) bonds are on average stronger than a Si-Si bond (327 kJ/mol) and thus harder to break, and since it is energetically less favorable to form a C-F bond (e.g. Si_3C-F: 450 kJ/mol, SiF_2C-F: 500 kJ/mol) in comparison to a Si-F bond (540 kJ/mol), the probabilities needed to be rescaled with a certain factor, which was estimated to be 0.5.

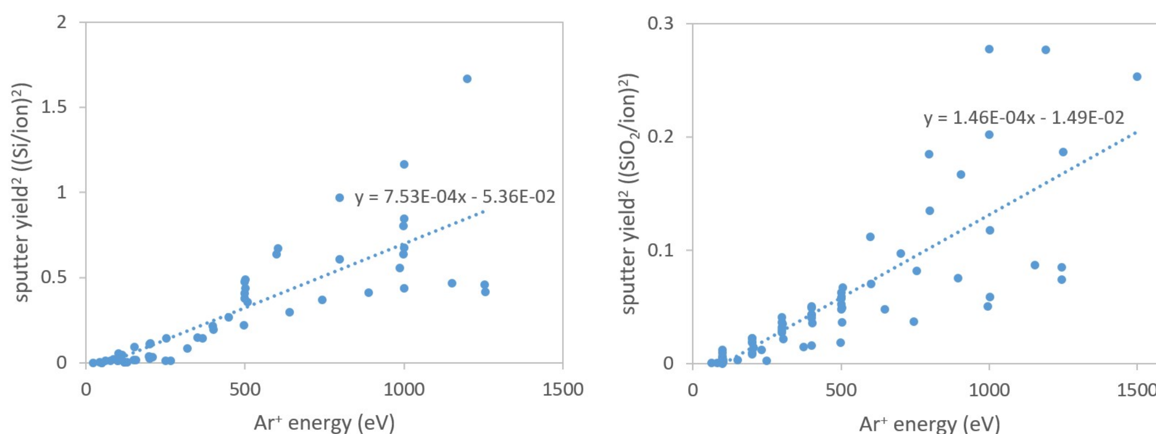

Figure 23. Square of the sputter yield for (left) Si and (right) SiO_2 etching with Ar^+ ions as a function of the ion energy. Data for Si are taken from [264-269] and for SiO_2 from [264-267, 270].

Ions

9. The energy dependency of the physical sputtering etch yield of Ar^+ ions on bare $Si_{(s)}$ was determined from a collection of literature data in the interval of 0 to 500 eV, as shown in Figure 23. The angular dependency is based on the data in [271, 272], shown in Figure 24(a)-(b).
10. The same dependencies were used for the sputtering of $SiF_{(s)}$ by Ar^+, in the assumption that this group is attached to the surface with nearly an identical binding energy as $Si_{(s)}$. The strength of the fourth distorted bond in $Si_{(s)}$ can namely be neglected to the orientationally favorable three other bonds. Sputtering of $SiF_{2\,(s)}$ and $SiF_{3\,(s)}$ requires less energy, since they are bound to the surface with only two and one bond, respectively. Their etch yield was chosen as double the one of step 9, in analogy with the relative etch yield by F^+ ions on the four surface groups, as calculated in [258]. The same angular dependency as in step 9 was assumed for these sputter reactions.
11. Ion-assisted etching by Ar^+ was implemented in the surface chemistry set as the reaction $SiF_{4\,(s)} + Ar^+ \rightarrow SiF_4 + Ar$, with an etch yield directly proportional to the energy based on the insights and data in [250]. Its angular dependency is a monotonically decreasing function of the incident angle relative to the surface normal, based on the dependency for ion-assisted etching of $Si_{(s)}$ with Cl_2 and Ar^+, as depicted in Figure 24(b) from [272].
12. The sputter probabilities of $CF_{y\,(s)}$ surface groups by Ar^+ were estimated from the ones of $SiF_{y\,(s)}$ in steps 9 and 10 and the involved binding energies. Since a Si-C bond (435 kJ/mol) is on average stronger than a Si-Si bond (327 kJ/mol), the etch yield was reduced with a factor 1.24, approximately equal to the ratio. Moreover, the strength of several C-C bonds (e.g. CH_3-CF_3: 423 kJ/mol, CH_2F-CH_2F: 368 kJ/mol, CF_3-CF_3: 406 kJ/mol, CF_2=CF_2: 318 kJ/mol, with H having a similar electronegativity as Si) are generally roughly comparable to the one of a Si-C bond. Therefore, no distinction was made in the subset between $CF_{y\,(s)}$ groups attached to the Si material or to a polymeric layer, as a simplifying assumption.
13. Ion-assisted etching of the deposited polymeric layer by Ar^+ is assumed to be analogous to the one described in step 11, through the reaction $CF_{4\,(s)} + Ar^+ \rightarrow CF_4 + Ar$, with the same angular dependency. As CF_4 and SiF_4 have a similar physisorption strength, the energy dependency is assumed to be identical as well.
14. Direct reactive ion etching of Si by F^+ is a more complicated process, as it simultaneously involves physical sputtering, ion deposition and ion-assisted chemical etching, in agreement with the analysis made in Section 4.2.1. Moreover, the sputtering involves the removal of both Si and F atoms from the intermediate $SiF_{y\,(s)}$ surface groups. Fortunately, the etch yield of both atoms has been calculated individually in [258] for y = 0 to 3. From this data, the energy-dependent reaction probabilities were determined with a primary focus on the sputtering of Si atoms. During a sputter event, the surface group was removed as a whole, implying the simultaneous sputtering of F atoms. In order to match the net sputtering of F atoms to the data in [258], an additional ion deposition reaction has been defined in the chemistry set for each of the $SiF_{y\,(s)}$ surface groups, with an energy dependency complementary to the one of the sputter reaction. All of these sputter reactions were assumed to have the same angular dependency, a monotonically decreasing function of the incident angle relative to the surface normal, as shown in Figure 24(c) from [273].

15. Analogous to step 11 for Ar^+, the ion-assisted etching component by F^+ is given by $SiF_{4\,(s)} + F^+ \rightarrow SiF_4 + F$, with an energy-dependent etching yield identical to the one for Ne^+ ions, which have a similar mass to F. Once more, the angular dependency of Figure 24(c) was selected for this reaction.
16. In analogy with step 12, the sputter probabilities of $CF_{y\,(s)}$ surface groups by F^+ were estimated from the ones of $SiF_{y\,(s)}$ in step 14, again rescaled with the factor 1.24. As an exception, the ion-assisted chemical etching reaction $CF_{4\,(s)} + F^+ \rightarrow CF_4 + F$ was given the same energy dependency as the one used in step 15.
17. The kinetic energy at which molecular ions collide with the wafer in a plasma etching reactor is generally much higher than the binding energy between the atoms in the ion. Therefore, the interaction between the ion and the surface can be approximated as the sum of the individual interactions of the composing atoms with the surface. An incident F_2^+ ion, for instance, can be considered as a combination of two F^+ ions with the same velocity. Obviously, this neglects several effects, such as the charge and the presence of the bond between the F atoms. However, this assumption forms a handy tool to estimate the etching behavior and probability of molecular ions, based on the reactions of the atomic ions. As such, the interactions between F_2^+ and the different surface groups were calculated by doubling the reaction probability and halving the kinetic energy in the formulas for the F^+ ion, which also implies doubling of the threshold energy.
18. The same strategy of step 17 has been applied for the CF_x^+ ions. In order to limit the number of reactions per ion type, the F atoms were assumed to play the central role in these interactions, justified by their higher contribution to the total ion mass. The C atom, on the other hand, was added to the F-based reactions as a side-kick. According to the experimental data in [249], C^+ ions have a stronger tendency to get deposited in comparison to F^+, with a probability around 0.4 at 233 eV, as an example. Hence, the C atom was assumed to be deposited in the energy dependent F-based sputter reactions. To avoid an overestimation of its deposition, the C atom was sent back to the gas phase in the reactions where the F atoms got deposited.

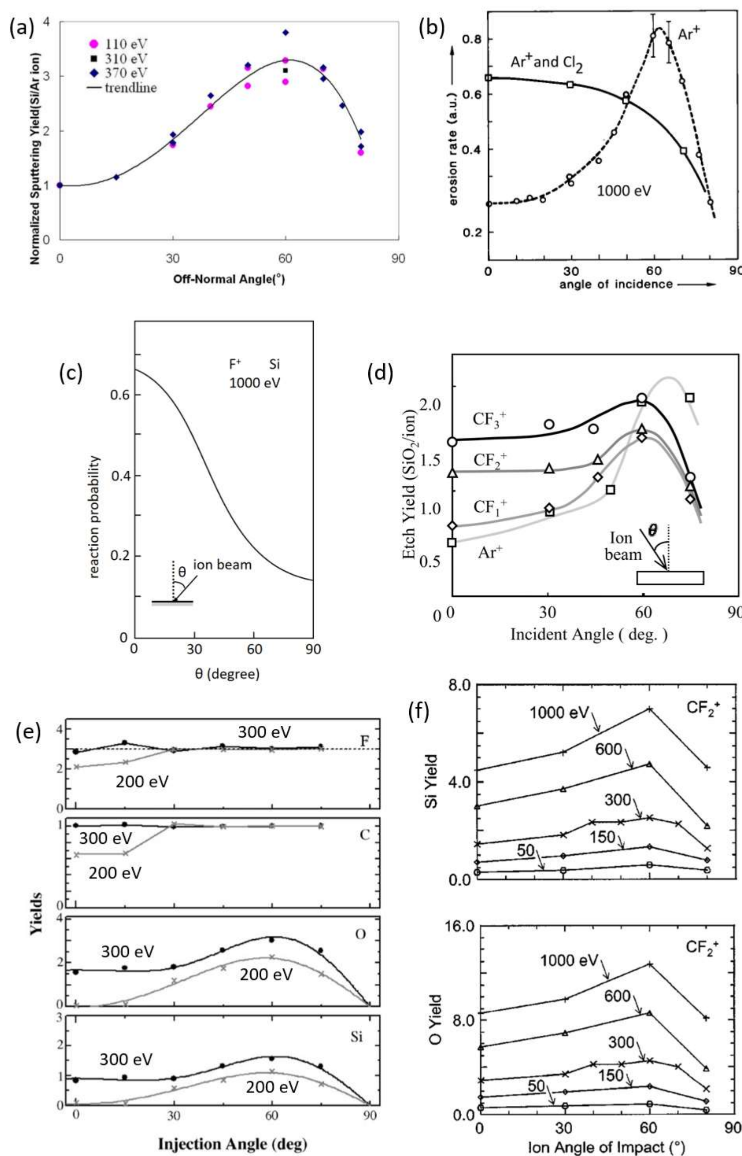

Figure 24. The angular dependencies of the etch yield used in the surface chemistry set, for (a) physical sputtering of Si with Ar^+, (b) physical sputtering and ion-assisted etching of Si with Ar^+ and Cl_2, (c) direct reactive ion etching of Si with F^+, (d) SiO_2 etching with Ar^+ and CF_x^+ with unknown kinetic energy, (e) SiO_2 etching with CF_3^+, and (f) SiO_2 etching with CF_2^+. The ion energies are indicated at the corresponding curves. (a) Reprinted with permission from J. Vac. Sci. Technol. A: Vac. Surf. Films 27, 1326 (2009) [271]. Copyright 2009, American Vacuum Society. (b) Reprinted from Nucl. Instrum. Methods Phys. Res. B: Beam Interact. Mater. At. 19, 1001 (1987) [272], Copyright 1987, with permission from Elsevier. (c) Reprinted from Nucl. Instrum. Methods 182, 241 (1981) [273], Copyright 1981, with permission from Elsevier. (d) Reprinted from [274], Kazuhiro Karahashi, Hyomen Kagaku Vol. 28(2), 2007; licensed under a Creative Commons Attribution (BY-NC 4.0) license. (e) Reprinted from Thin Solid Films 515, 4883 (2007) [275], Copyright 2007, with permission from Elsevier. (f) Reprinted from J. Appl. Phys. 97, 093302 (2005) [232], with the permission of AIP Publishing.

Table III. The reactive etch products and surface groups considered in the surface chemistry subset of SiO_2 etching with CF_4/Ar, in addition to the ones mentioned in Table II. As before, the etch product

SiO_2 consists of 10 molecular units. The non-reactive etch products CO_2 and O_2 were immediately removed from the simulation region after their emission.

Additional neutral incident species	Additional incident ions	Additional chemically active gaseous etch products	Additional surface groups
none	none	SiO_2	$SiO_{2\ (s)}$ $SiO_2C_{(s)}$ $SiO_2CF_{(s)}$ $SiO_2CF_{2\ (s)}$ $SiO_2CF_{3\ (s)}$ $SiO_2CF_{4\ (s)}$

<u>The subset focused on SiO_2 etching with CF_4/Ar</u> considers no additional plasma species, but includes the new chemically active gaseous etch product SiO_2 and six extra surface groups (see Table III). Its reaction probabilities were taken from literature or estimated as follows:

Gaseous SiO_2:

19. The fundamental etching processes on a composite substrate as SiO_2 have a higher level of complexity than on a single element substrate as Si, since the composing elements (Si and O) may be removed and deposited with different yields. As shown in the study [262], however, physical sputtering of SiO_2 leads to redeposition of Si and O_2 with an equal probability of 1 on $SiO_{2\ (s)}$. This also seems in good agreement with the classical MD simulations combined with MC by Taguchi and Hamaguchi, although the incident angle and energy of the redepositing particles can cause some deviations [276, 277]. However, such details are not included in MCFPM, because it assumes the etch products to desorb with thermal energies in a modified Lambertian distribution (see Section 4.1.5), before their redeposition. For this reason, gaseous SiO_2 was chosen as the only sputter product in the subset.
20. The deposition probabilities of SiO_2 on $SiF_{y\ (s)}$ and $CF_{y\ (s)}$ groups were chosen identical to the ones of Si radicals, based on the assumption that the resulting bond is always made with the Si atom of the SiO_2 radical.

Neutral gas species reacting with the new surface groups:

21. According to [278], the chemical etching yield of SiO_2 by F radicals is approximately 10 times lower than for Si. Since no F deposition probabilities are available in literature for individual fluorinated SiO_2 groups, this mechanism was implemented in the subset as $SiO_{2\ (s)} + F \rightarrow SiF_4 + O_2$, with a reaction probability of 0.0015, in agreement with step 7. The conform reaction of F_2 was given twice this probability. These are the only reactions producing gaseous O_2 in the subset, with the exception of the ones for deposition of F^+ ions further discussed in steps 27 and 28.
22. For deposition of CF_x radicals on $SiO_{2\ (s)}$, a formed Si-C bond (435 kJ/mol) is energetically more favorable than an O-C bond (358 kJ/mol). Chemisorption, however, requires breaking of a Si-O bond (452 kJ/mol), which is significantly stronger than a Si-Si bond (327 kJ/mol). This not only explains the 10 times lower fluorination rate discussed in step 21, it also justifies selecting

the same scaling factor for CF_x deposition. Accordingly, the reaction probabilities of these radicals with $SiO_{2\,(s)}$ were determined by dividing the values obtained in step 4 for deposition on $Si_{(s)}$ by a factor 10.

23. Similarly, for deposition of SiF_x radicals on $SiO_{2\,(s)}$, a formed O-Si bond (452 kJ/mol) is energetically more favorable than a Si-Si bond (327 kJ/mol). Moreover, it has a similar strength as the Si-C bond (435 kJ/mol) created during CF_x deposition on $SiO_{2\,(s)}$. Therefore, the same probabilities were taken for chemisorption of SiF_x on $SiO_{2\,(s)}$ as for the CF_x radicals in step 22.
24. For x = 4, physisorption takes place instead of chemisorption, so the reasoning in steps 22 and 23 cannot be used. Instead, the deposition probabilities of CF_4 and SiF_4 on $SiO_{2\,(s)}$ were assumed equal to the ones for attachment on $Si_{(s)}$, as determined in step 5.
25. Reaction probabilities of gaseous neutrals on $SiO_2CF_{y\,(s)}$ are chosen identical to the ones on $CF_{y\,(s)}$ groups.

Ions interacting with the new surface groups:

26. Similar to step 9, the energy dependency of physical sputtering for Ar^+ ions on bare $SiO_{2\,(s)}$ was determined from a collection of literature data in the interval of 0 to 500 eV, as shown in Figure 23(b). The angular dependency, depicted in Figure 24(d), was taken from [274]. Note the difference with the angular dependency of Si sputtering.
27. The energy dependency of direct reactive ion etching of $SiO_{2\,(s)}$ by F^+ ions has been deduced from the experimental data in [279, 280] and compared with the MD simulated relationships in [260, 281]. The same angular dependency was assumed as in step 14 and Figure 24(c) for a Si substrate. Deposition of the F^+ ions was implemented with the reaction $SiO_{2\,(s)} + F^+ \rightarrow SiF_{(s)} + O_2$, using a relative probability to the etch reaction based on the results of step 14, but divided by 10 to account for the lower chance to fluorinate $SiO_{2\,(s)}$ in comparison to $Si_{(s)}$ (see step 21).
28. The result of step 27 served as a base for the interaction of F_2^+ with $SiO_{2\,(s)}$, following the same philosophy as in step 17.
29. The energy dependency of the interaction between CF_x^+ ions and $SiO_{2\,(s)}$ was deduced from the experimental data in [279, 280, 282] and compared with the relationships given in [278]. For the sake of simplicity, the energy at which no net etching occurs was chosen as the threshold energy between the deposition reaction at lower energy and the etching reaction at higher energy. The angular dependency of these reactions was assumed to be the same as the one of F^+ etching of Si of Figure 24(c) (see also the discussion further in step 33).
30. MD calculated etch yields of individual $SiO_2CF_{y\,(s)}$ groups by incident ions are not present yet in literature. Fortunately, sufficient experimental data is available for most ions on the average etch yield, i.e. integrated over the different surface groups with y from 0 to 4. In a first approximation, the reactions were assumed to be independent from y. For Ar^+, the threshold energy of 71.1 eV and the etch yield of 1.3 SiO_2/ion at 130 eV was taken from the atomic layer etching study in [283], corresponding to the reactions $SiO_2CF_{y\,(s)} + Ar^+ \rightarrow SiF_y + CO_2 + Ar$ (for y from 0 to 4). Next to that, the reactions $SiO_2CF_{y\,(s)} + Ar^+ \rightarrow SiF_{y\,(s)} + CO_2 + Ar$ were added with half the probability, to account for the release of CO_2 alone, in agreement with the accepted theory in literature [283, 284]. The threshold energy of 25 eV of the latter reaction was taken from another atomic layer etching investigation [285]. The angular dependence of these reactions was not found in literature. Based on the MD simulation output by Harafuji and Kawamura for ion-assisted chemical etching versus physical sputtering

of GaN with and without a Cl-adsorbed layer by Ar^+ [286-288] (see Figure 25), we assumed this angular dependence to be equal to the one for Ar^+ in Figure 24(d). We will discuss this topic further in Section 4.3.

31. No experimental data could be found for the interaction of F^+ ions with $SiO_2CF_{y\,(s)}$ groups. The reactions were assumed to be identical to the ones of Ar^+.
32. The interaction between F_2^+ ions and $SiO_2CF_{y\,(s)}$ groups was deduced from the reactions of F^+ ions in step 31, according to the same principle as explained in step 17.
33. Each reaction between an CF_x^+ ion and an individual $SiO_2CF_{y\,(s)}$ group forms a part of the overall interaction between this type of CF_x^+ ion and an initially clean $SiO_{2\,(s)}$ substrate. The energy dependencies determined in step 29 can therefore serve as a basis for the reactions on $SiO_2CF_{y\,(s)}$, with y ranging from 1 to 4. Once more, as a first approximation, the probabilities were assumed to be independent of y. The angular dependencies, however, were chosen different for the reactions emitting SiF_4 into the gas phase. More precisely, the latter reactions were given the angular dependency of physical sputtering in Figure 24(d), in contrast to the dependency of Figure 24(c) for the reactions which emit SiF_x radicals. This choice is crucial for obtaining a correct agreement with experimentally etched trench profiles, as further discussed in Section 4.3. In scientific literature, the etch yield for all of these reactions is often assumed to be monotonically decreasing as a function of the incident angle. The experimental angular dependencies of CF_x^+ obtained in [232, 274, 275] and shown in Figure 24(d)-(f) prove this to be incorrect. Rather, the overall angular dependencies of etching with CF_x^+ ions seem to be a combination of the one from Ar^+ in Figure 24(d) for physical sputtering and the one in Figure 24(c) for direct reactive ion etching, justifying the way they have been implemented in the subset.

Table IV. The incident neutral species and ions considered in the surface chemistry subset of SiO_2 etching with CHF_4/CHF_3/Ar, in addition to the ones mentioned in Tables II and III.

Additional neutral incident species	Additional incident ions	Additional chemically active gaseous etch products	Additional surface groups
CHF_3	CHF_2^+ CHF^+	none	none

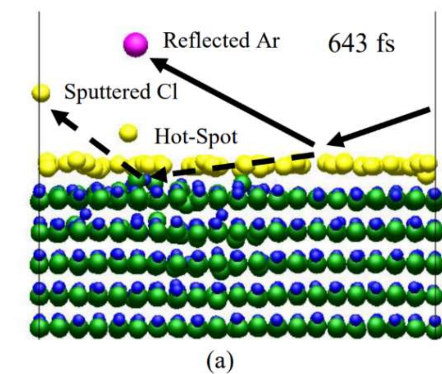

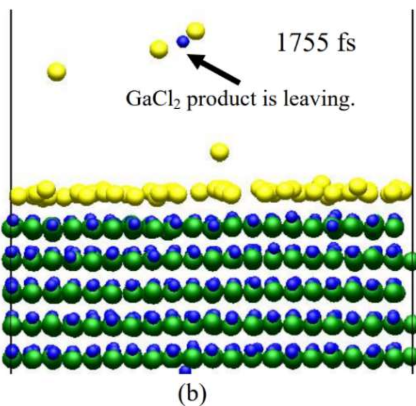

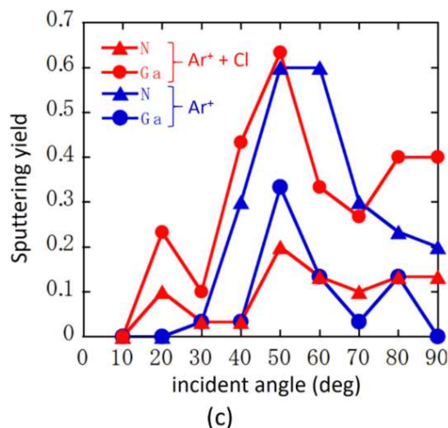

Figure 25. Ion-assisted chemical etching of a GaN substrate with adsorbed Cl atoms and incident Ar^+ under a varying angle with the surface, with (a) the first sputter event upon impact, (b) molecular emission after hot spot formation and (c) the angular dependence of the sputtering yield. The curves are obtained by averaging over 30 incident ions per angle, for a kinetic energy of 250 eV. Note that the incident angle is considered relative to the surface plane, i.e. 90° represents the direction along the surface normal. The angular dependence of ion-assisted etching (red curves) roughly coincides with the one of physical sputtering (blue curves). (a)-(b) Reproduced and (c) adapted from [286], with permission from the authors K. Harafuji and K. Kawamura, as well as the International Plasma Chemistry Society.

The subset focused on the addition of H-containing species in SiO_2 etching with $CF_4/CHF_3/Ar$ considers one additional neutral incident species and two ions, but does not introduce new gaseous etch products or surface groups (see Table IV). Obviously, the absence of hydrogenated surface groups is a simplifying assumption, but can also be justified for the following reasons:

- According to several sources in literature, the main difference in etching between fluorocarbon-based and hydrofluorocarbon-based gas mixtures is related to the gas chemistry, not the surface chemistry. More specifically, the presence of H radicals depletes the density of F radicals in the gas phase, by forming HF as a stable product. This reduces the net flux of reactive F-containing species towards the wafer, as HF has a very low reactivity. Accordingly, the etching process is mainly influenced by a shift in fluxes.
- H radicals are less reactive than F radicals, making the latter not only more dominant in relative density, but also in reaction probability.
- Several other incident H-containing species either have a low reactivity (e.g. HF and H^+) or a low flux (e.g. CH, CHF_2 and CHF) relative to the other particles considered in the surface chemistry set.
- Hydrogenation of polymeric surface groups, $Si_{(s)}$ and $SiO_{2\,(s)}$ plays a similar role in the overall surface chemistry as fluorination. Indeed, both H and F atoms reduce crosslinking between superficial C or Si atoms and can lead to the formation of volatile molecules, such as SiF_4, $SiHF_3$ and SiH_4.

Still, CHF_3, CHF_2^+ and CHF^+ cannot simply be neglected, due to their high relative incident flux. Their reaction probabilities were estimated as follows:

34. In comparison to CF_4, CHF_3 is expected to have a lower physisorption strength due to its smaller size, and a lower reaction probability in ion-assisted chemical etching due to the lower reactivity of the H atom. To take these effects into account, its reactions were obtained from the ones of CF_4 by rescaling them with the factor 0.80, which is the mass ratio of both molecules. Note that these reactions produced the H-free surface groups $CF_{4\,(s)}$ and $SiO_2CF_{4\,(s)}$, as a simplifying approximation.
35. For the ions CHF_2^+ and CHF^+, the H atom was neglected. In other words, their reactions were copied from CF_2^+ and CF^+, respectively. Note that this is in agreement with the low etch yield of the H^+ ion.

The subset focused on the surface chemistry of the photoresist was considered in less detail than the ones of $Si_{(s)}$ and $SiO_{2\,(s)}$. It was implemented as follows:

36. For simplicity, the photoresist was assumed unreactive to neutrals.
37. The interactions between ions and the photoresist were obtained from the ones of the $C_{(s)}$ surface group by multiplying the reaction probabilities with a factor of 2.67. Accordingly, the angular dependency of Figure 24(c) was implemented for all ions, except for Ar^+, where the one of Figure 24(d) was used.

Despite its simplicity, this subset gave a satisfying agreement with the experimentally observed etched profiles of the photoresist (see Section 4.3).

4.3 Benchmarking the simulation model – bringing uncertainties to the surface

In Section 4.2.2, we demonstrated how a surface chemistry set can be designed by means of the bottom-up approach introduced in Section 4.1.1. As such, quantitative experimental and computational data on individual interactions between a plasma species and the surface were used to implement the surface reactions in the set. If such reliable data was not found in scientific literature, estimations were made based on similar interactions and on the involved binding strengths. In this way, we tried to keep the assumptions and approximations in the set to a minimum. Accordingly, the set has already been benchmarked for a significant part on the level of the individual interactions. In the present Section, we experimentally benchmark the set further with a top-down approach, i.e. by comparing the simulation output and experimental data for the plasma-surface interaction as a whole, in the CCP Leybold F2 reactor at the operating conditions presented in Section 4.1.7. Next, we analyze the contribution of the individual surface mechanisms and some of their properties.

Table V and Figure 26 present some details on the output of the macroscale HPEM model that serves as input for the mesoscale MCFPM model, namely the incident species fluxes and the ion energy and angular distributions. Based on this data, the dominant surface mechanisms may already be predicted. The ion energies range over an interval of around 280 to 340 eV, which only varies a little between different ions. This energy range favors etching over deposition, also for the carbon-containing ions CF_3^+, CF_2^+, CF^+, CHF_2^+ and CHF^+, whose threshold energy between the two mechanisms is implemented at 108, 106, 221, 106 and 221 eV in the surface chemistry set, respectively. The fluxes, on the other hand, reveal a clear divergence between the various incident species. Among the ions, Ar^+ and CF_3^+ are most prevalent. CF_2^+, CF^+, CHF_2^+ and CHF^+, bombard the surface with fluxes of one to two orders of magnitude lower. Their similar surface chemistry relative to CF_3^+, allows considering them as a correction on the CF_3^+ flux. Removing them from the MCFPM simulation thus can be compensated by proportionally increasing the CF_3^+ flux. The contribution of H^+, F^+ and F_2^+ is negligible, due to their comparatively low fluxes and the low reactivity of H^+. CHF_3 is the most prevalent neutral species, as expected, followed by the F radical. Since H and HF are neglected in the surface chemistry due to their relatively low reactivity (see Section 4.2.2), the next radicals to be considered are CF, CF_2 and CF_3. Because of their similar chemistry and depositing nature, they can be understood as an equivalent fluorocarbon radical with a flux equal to their fluxes combined, i.e. 3.2×10^{16} $cm^{-2}s^{-1}$. This approximates the F radical flux of 4.3×10^{16} $cm^{-2}s^{-1}$. Their relative reactivity with the surface can, however, not easily be compared, as it strongly depends on the interacting surface group. Therefore, an analysis of the surface fractions of the various groups will give additional insight.

Table V. Fluxes of the plasma species towards the wafer surface in the Leybold F2 reactor at standard settings, averaged over the third wafer segment in Figure 16, i.e. between R = 1 cm and R = 9.5 cm.

Neutral species	**Flux (cm^{-2} s^{-1})**	**Ions**	**Flux (cm^{-2} s^{-1})**
CHF_3	7.8×10^{17}	CF_3^+	1.7×10^{15}
F	4.3×10^{16}	Ar^+	1.4×10^{15}
H	1.9×10^{16}	CHF_2^+	1.9×10^{14}
CF	1.6×10^{16}	CF^+	1.4×10^{14}

CF_2	9.3×10^{15}	CF_2^+	6.7×10^{13}
HF	7.5×10^{15}	CHF^+	2.3×10^{13}
CF_3	7.0×10^{15}	H^+	2.3×10^{13}
H_2	3.4×10^{15}	F^+	7.1×10^{12}
CH	6.6×10^{14}	C^+	5.3×10^{10}
C	6.2×10^{14}	F_2^+	3.0×10^{9}
CHF_2	5.4×10^{14}		
CHF	2.6×10^{14}		
F_2	1.6×10^{13}		

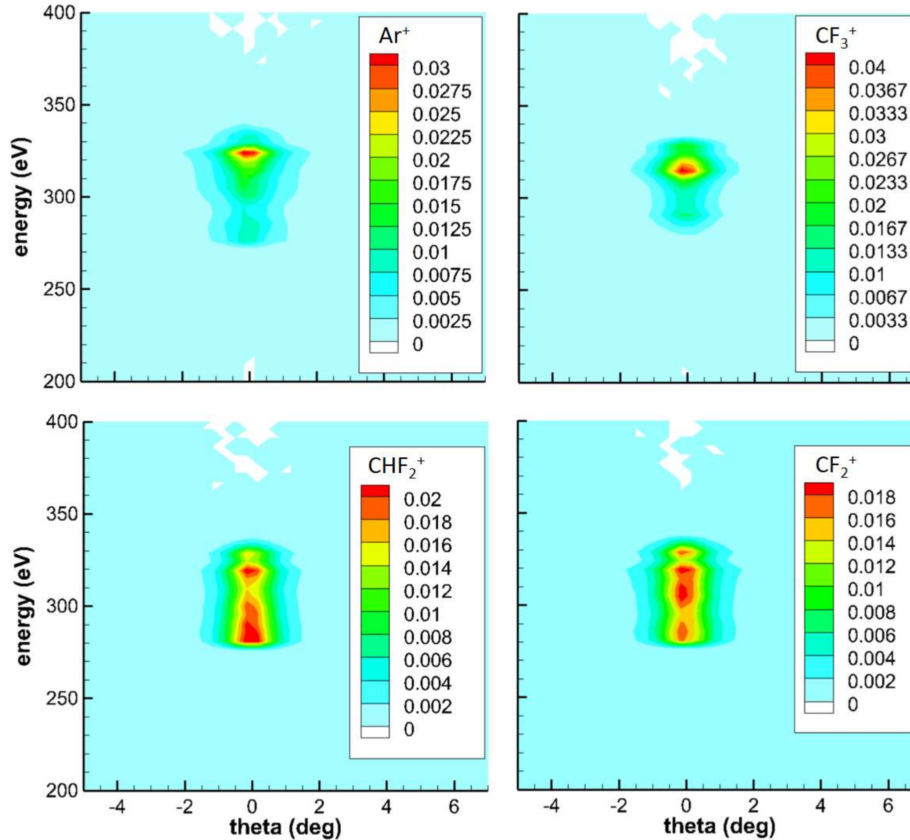

Figure 26. The ion energy and angular distributions of the most prevalent ions over the wafer surface in the Leybold F2 reactor at standard settings, averaged over the third wafer segment in Figure 16, i.e. between R = 1 cm and R = 9.5 cm.

Figure 27 shows the initial photoresist profile for a critical dimension (CD) value of 315 nm and the corresponding etched trench as predicted by the MCFPM simulation after 240 s of plasma etching. In the analysis of the surface group fractions, the trench bottom needs to be distinguished from the trench walls. The surface fractions are namely expected to depend on the average angle that the incident ions make with the surface normal, due to the angular dependency of the ion reaction probabilities (see Figure 24). As seen in Table VI, $SiO_2CHF_{3\,(s)}$ has by far the highest surface fraction from all surface groups, confirming the dominance of CHF_3 deposition by physisorption among the neutral species. The surface is mainly covered with the groups responsible for ion-assisted etching, i.e. $SiO_2CHF_{3\,(s)}$, $CF_{4\,(s)}$ and $SiF_{4\,(s)}$, which are supposed to be unreactive to neutral species. A quarter of the trench bottom remains uncovered, i.e. exposed as $SiO_{2\,(s)}$, implying that physical sputtering and chemical etching may still play a noticeable role. This stands in contrast to the sidewall, which lies

exposed for only 5%. Regarding the other groups, $SiO_2CF_{x\,(s)}$, $CF_{x\,(s)}$ and $SiF_{x\,(s)}$ (with x = 0 to 3) have a higher reactivity towards F radicals than CF_x radicals, according to the surface chemistry set. $SiO_{2\,(s)}$ contrarily reacts more easily with CF_x than F. Both types of radicals are therefore expected to contribute in their own unique way to the etching process.

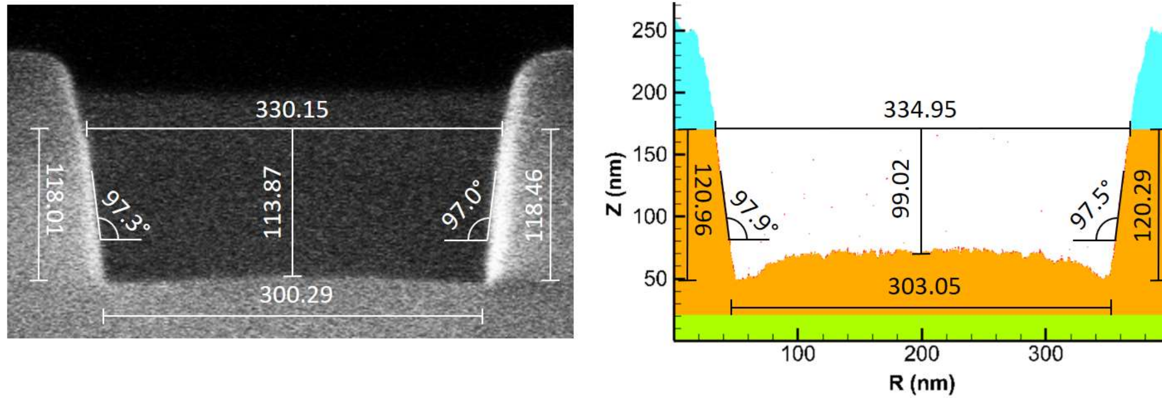

Figure 27. Comparison of (left) the experimental etched trench for initial CD = 315 nm and an etch time of 180 s, with (right) the simulated one using the original surface chemistry set designed in Section 4.2.2, at approximately the same etch depth. The dimensions are indicated in nanometer.

Table VI. The surface fractions of the surface groups located at the trench bottom and sidewall. The groups with x = 0 to 3 are presented together. Note that no difference is made in the surface chemistry set between $SiO_2CHF_{3\,(s)}$ and $SiO_2CF_{4\,(s)}$, and hydrogen is further not considered on the surface as a simplification (see step 34 in Section 4.2.2).

Surface group	Bottom fraction	Wall fraction
$SiO_2CHF_{3\,(s)}$	45.2%	65.1%
$SiO_2CF_{x\,(s)}$	8.6%	6.8%
$CF_{4\,(s)}$	9.7%	12.6%
$CF_{x\,(s)}$	5.0%	2.6%
$SiF_{4\,(s)}$	5.3%	7.6%
$SiF_{x\,(s)}$	1.4%	0.2%
$SiO_{2\,(s)}$	24.8%	5.1%

Note the already remarkable agreement between the simulated and experimentally observed etched profile (see Figure 27). This demonstrates the power of the bottom-up benchmarking approach, and facilitates a further analysis. Especially the trench sidewalls are predicted very well by the surface chemistry set, making angles of 7.9° and 7.5° with the vertical axis at the left and right side, respectively. On the other hand, the model only explains the curved shape of the trench bottom in a qualitative way, overestimating the height difference between the bottom center and the micro-trenches at the sides with a factor of 5. Also the strong bottom roughness in the simulations clearly contrasts with the experimental result. Additional top-down benchmarking is required to resolve the origin of these errors and to remediate them. Based on the surface fractions and incoming fluxes, ion-assisted chemical etching and direct reactive ion etching with CHF_3, Ar^+ and CF_3^+ are expected to be the dominant surface mechanisms in the etching process. This is confirmed by eliminating all other plasma species from the simulation input in MCFPM. As shown in Figure 28 (top center frame), this results in a similar trench profile and etch rate relative to the complete etch chemistry (bottom left

frame). The uncertainties in the surface reactions of Ar^+ and CF_3^+ therefore deserve a great deal of attention, as they affect the simulation results with the highest sensitivity.

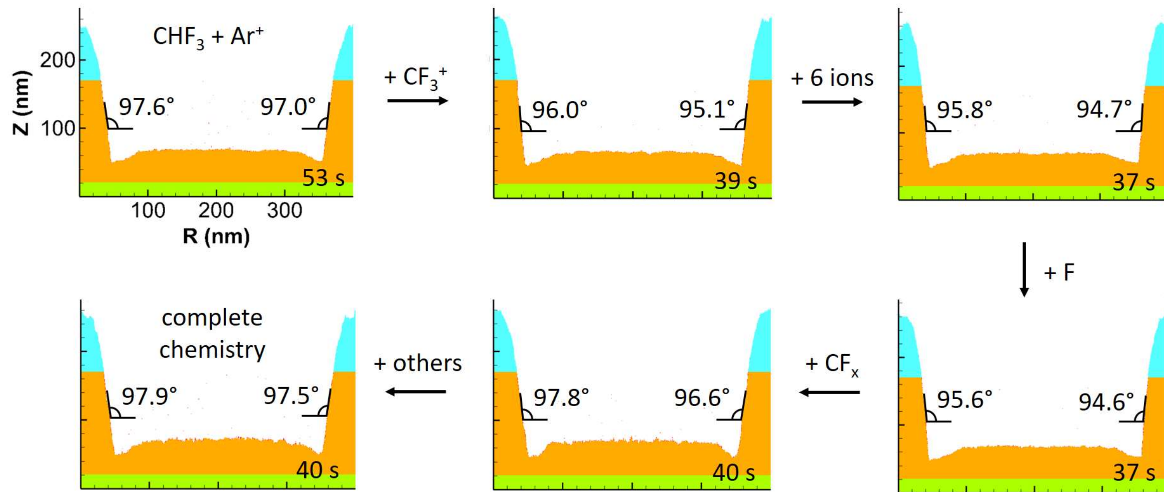

Figure 28. Variation of the etched profile by the stepwise addition of incident species. Starting the exposure of the surface by only CHF_3 and Ar^+, first CF_3^+ is added and then the six other main ions CHF_2^+, CF^+, CF_2^+, CHF^+, F^+ and F_2^+. Next, F radicals join the simulation, followed by CF, CF_2 and CF_3 radicals. Finally, the inclusion of the remaining plasma species gives the complete surface chemistry. The left and right sidewall angles and the etch time are indicated in each frame.

Here, we encounter the first obstacle in the surface chemistry set design: ion-assisted chemical etching and direct reactive ion etching are the least accurately quantified etching mechanisms, despite being the dominant ones. Most likely, this is due to their multi-step nature. That is, ion-assisted chemical etching requires physisorption (e.g. of CHF_3) before the ion-surface interaction, which complicates its investigation. Similarly, direct reactive ion etching leads to the formation of a deposited layer on the substrate surface, of which the composition and thickness varies with the operating conditions. Only carefully designed experiments or atomistic simulations can provide quantitative data on the reaction probabilities between the ion and the involved surface groups, none of which were found in the scientific literature. An exception is the single data point of the etching yield for atomic layer etching of SiO_2 with Ar^+ and physisorbed C_4F_8 from [283], as described in step 30 of Section 4.2.2. However, the ion energy and angular dependencies remain unknown, as well as the exact reaction probabilities for physisorbed CHF_3 and chemisorbed CF_x groups. Hence, in the following we investigate the influence of these dependencies on the feature profiles and etch rate.

The etched profile is strongly sensitive to the angular dependence of the ion reactions. Figure 29 illustrates this for Ar^+ or CF_3^+ bombardment of the SiO_2 wafer in the presence of CHF_3, as well as the complete chemistry. The angular dependencies of the etch yield are chosen based on the limited information that we could find in literature. In general, regardless of the involved plasma species and surface groups, two angular dependencies are often distinguished, referred to as physical and chemical etching [284, 289, 290]. Whereas the physical variant displays a maximum in the etch yield at an off-normal angle around 60-70°, the chemical counterpart is described by a cosine dependence, thus with a maximum at normal incidence. According to the conventional theory, direct reactive ion etching is considered a composite of both cases, in agreement with Figure 24(d)-(f) and the surface chemistry set designed in Section 4.2.2. The situation for ion-assisted chemical etching is less clear, with many sources assuming a monotonously decreasing angular dependence (see e.g. [291-296]),

while Figure 25 suggests otherwise. Perhaps, it can also be considered a composite of the physical and chemical etching counterparts, with variable relative contributions.

The crossover between both regimes may strongly depend on the considered plasma species, the substrate material and its surface conditions, as well as the ion energy. Figure 24(e), for instance, indicates a strong physical etching component of SiO_2 at low energy for CF_3^+, contrary to the less pronounced energy dependence for CF_2^+ in Figure 24(f). This also stands in contrast with several claims in scientific literature, which assume the chemical component to prevail at low energies or simply be dominant overall in direct reactive ion etching (see e.g. [289, 290, 297-299]). Several experimental studies with CF_4 and other pure fluorocarbon plasmas on SiO_2 seem to agree with this assumption, detecting a growing physical component as a function of the ion energy (see e.g. [266, 300-304]). However, a large physical etching component was observed in some of these investigations even at relatively low kinetic energies [300, 302, 304]. The role of the physical component is therefore dependent on the operating conditions. Based on the available data in literature, it is yet unclear which individual reactions are responsible for its contribution. The results in Figure 24(d)-(f) namely only show data at fixed surface conditions for each ion.

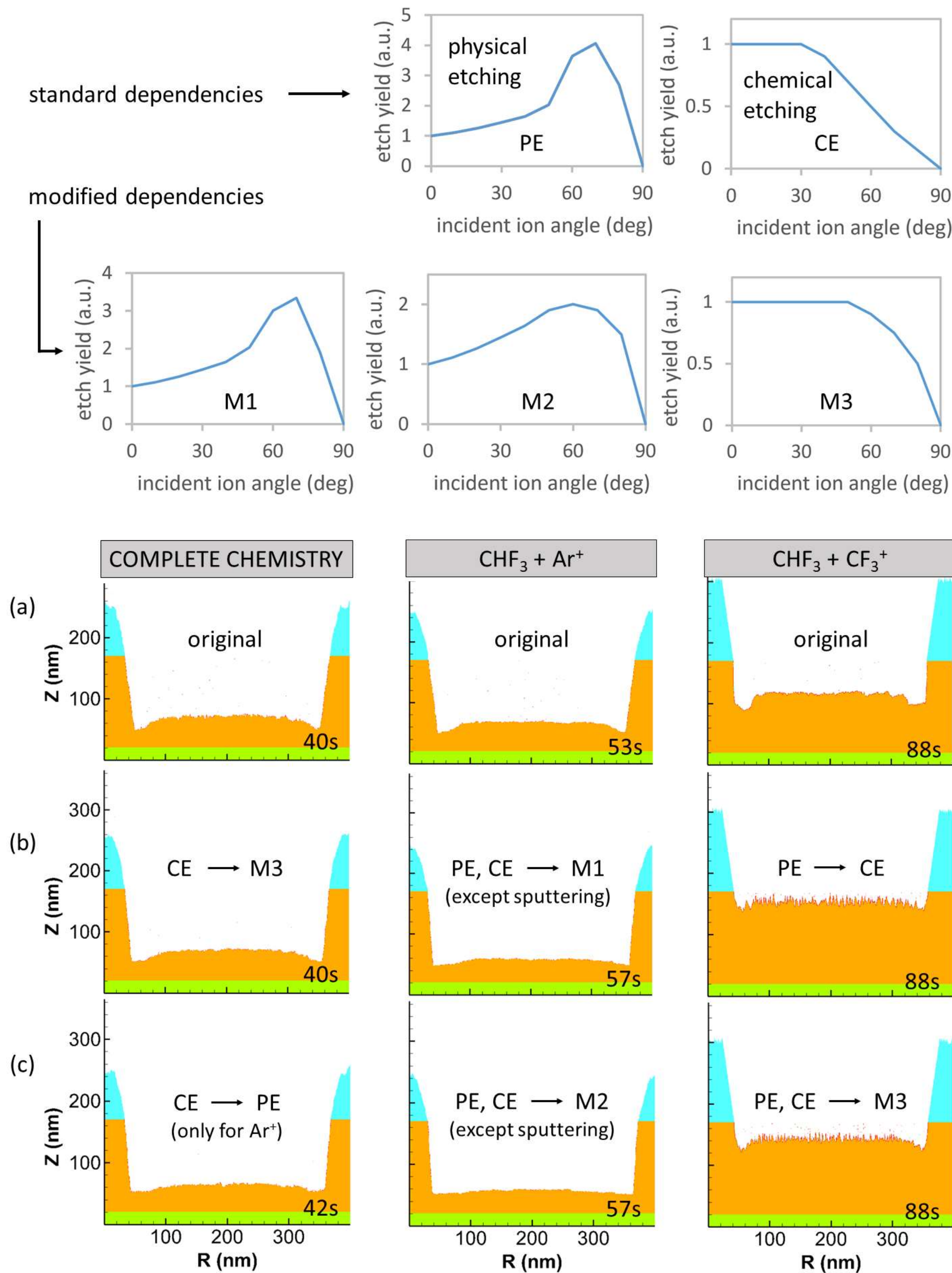

Figure 29. Effect of the etch yield angular dependence on the etched trench profile. (top) The standard and modified angular dependences used for the ion reactions. (bottom) The etched profile produced by the complete chemistry (left), only CHF_3 and Ar^+ (middle), and only CHF_3 and CF_3^+ (right), where the insets X → Y indicate that the angular dependence X was replaced with Y, for all reactions except if mentioned otherwise in parentheses. For each simulation, a frame is shown with an etch depth around 120 nm for the ease of comparison, except for the right column, where the frame with an etch time of 88 s is selected.

The situation for ion-assisted chemical etching of SiO_2 with physisorbed fluorocarbon gas molecules by Ar^+ ions is even less understood. The only data we could find in the scientific literature related to its angular dependence is presented in Figure 30, for a CF_4/Ar plasma [305]. Similar to Figure 24(e), a

physical etching component seems to dominate at low ion energies, while a chemical component becomes more important at higher ones. Unfortunately, Figure 30 only shows the effect of a full CF_4/Ar plasma chemistry under specific operating conditions, as it does not resolve between surface reactions by Ar^+ and CF_x^+ ions. It is thus unclear which factors determine the physical component, and to which extent Ar^+ ions contribute to it. Possibly, the thickness of the formed polymeric CF_x layer plays a decisive role. This aspect is not taken into account in the MCFPM simulations, as the model does not allow to describe a stable surface layer with a thickness of more than one mesh cell during etching. Alternatively, the composition of the polymeric layer, such as the surface groups and the C/F ratio, may regulate the angular dependence of the surface reactions. MCFPM can take such effects into account by resolving the angular dependences between individual surface reactions. This, however, requires accurate quantitative knowledge on these dependences, which is not available yet.

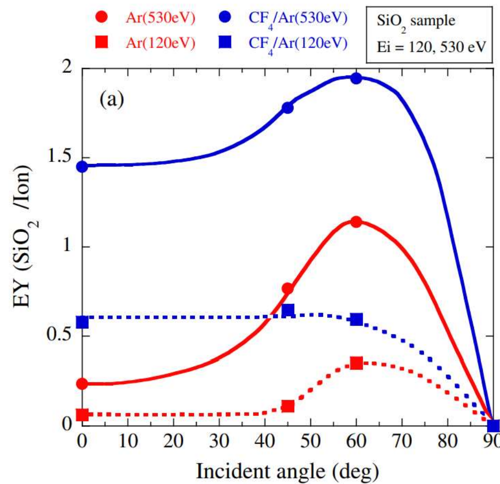

Figure 30. Measured angular dependence of the SiO_2 etch yield by a CF_4/Ar plasma (blue) and an Ar plasma (red), for the ion energies of 120 eV (dotted line) and 530 eV (solid line). The lines serve as guides for the eye. Reprinted with permission of IOP Publishing, Ltd, from Jpn. J. Appl. Phys. 50, 120206 (2011) [305]. Copyright 2011 The Japan Society of Applied Physics.

Returning to Figure 29, one sees that the angular dependence can account for several effects. Replacing the angular dependence of physical etching in the surface chemistry set with the one of chemical etching causes spikes to develop on the trench bottom during etching, thus strongly increasing the bottom roughness, as seen in the right column of Figure 29(a)-(c). This effect took place independent of the identity of the incident ion (Ar^+ or CF_3^+) in the presence of the CHF_3 flux. Remarkably, similar spikes formed when all CF_3^+ reactions were given the experimental angular dependence of CF_3^+ shown in Figure 24(d) (not shown in Figure 29). This may partly be an artifact from the simulations. The surface plane calculation in MCFPM (see Figure 13 and Section 4.1.5) and thus the incident ion angle is namely determined from the adjacent cells, i.e. approaching the atomic scale. This might result in a different angle than the one experienced by an ion in the experiments, which is likely correlated to the size of the generated hot spot (see Section 4.2.1, Figure 18 and Figure 25). Moreover, MCFPM only considers surface reactions of ions with the upper surface group, while underlying layers may play an important role in the experiment.

If only CHF_3 and Ar^+ are released towards the surface, a reduction of the etch yield maximum around 70° in physical etching contracts the height difference between the micro-trenches and the center of the trench bottom (not shown in Figure 29). If additionally the reactions $\mathrm{SiF}_{4\,(s)} + \mathrm{Ar}^+ \rightarrow \mathrm{SiF}_4 + \mathrm{Ar}$

and $CF_{4\,(s)} + Ar^+ \rightarrow CF_4 + Ar$ have their chemical etching angular dependence (see steps 11 and 13 in Section 4.2.2) replaced with the modified ones for physical etching, i.e. M1 and M2, the height difference is further reduced, as shown in the middle column of Figure 29(a)-(c). In this way, the overestimation of this height difference relative to the experiments drops to a factor of about 2 in the simulations for the middle frame of Figure 29(c), a significant improvement from the original value of 5. Simultaneously, the sidewall angles contract significantly, leading to a larger deviation from the experiment in this regard. However, this gives useful information on how to further benchmark the surface chemistry set.

This is illustrated in the left frame of Figure 29(c) for the complete chemistry including all incident plasma species. If the chemical etching dependence of the aforementioned two reactions of Ar^+ is replaced with the one of physical etching, the bottom strongly flattens. In other words, the physical etching angular dependence seems to apply to most ion-assisted chemical etching reactions in the surface chemistry set, in contrast to what is often suggested in literature. Moreover, this demonstrates a decisive contribution of the $SiF_{4\,(s)}$ and $CF_{4\,(s)}$ surface groups to the etching process, despite their relatively low surface fractions (see Table VI). Contrary to the observations for only CHF_3 and Ar^+ as incident species, exchanging the angular dependence of physical etching with M2 in the complete chemistry for Ar^+ alone or for all ion reactions has a negligible or worsening effect on the bottom shape, respectively (not shown in Figure 29). The etching process is therefore not simply the sum of the isolated effects of its sub-processes. Still, fine-tuning the chemical etching angular dependence can further improve the etched trench shape, as exemplified by the smoother trench bottom in the left frame in Figure 29(b) and confirmed in a separate simulation that combines the modifications in the left panels of 29(b) and 29(c) (not shown in the Figure). However, a smoother bottom by adapting the angular dependences generally came at the cost of sidewall contraction in our case study. In a nutshell, this analysis illustrates the crucial need for accurate quantitative data on the angular dependence of each individual reaction, with ion-assisted chemical etching and direct reactive ion etching in particular. Such data can only be reliably obtained with a combination of dedicated fundamental experiments and atomistic time-dependent models.

Note the very small sidewall angles produced by the surface chemistry set with the original settings, when the surface is only subjected to the CHF_3 and CF_3^+ fluxes (right column of Figure 29(a)). This explains the smaller sidewall angles in the case of the three fluxes of CHF_3, Ar^+ and CF_3^+ combined (top center frame in Figure 28), relative to the simulation with all species fluxes enabled and to the experiment (Figure 27). Therefore, the other plasma species and surface mechanisms are required in the model to obtain an accurate result. Further insight into the role of the other surface mechanisms is readily obtained by adding other incident plasma species to the simulation in a stepwise manner, as shown in Figure 28. Including the next six most prevalent ions, as well as F radicals, does not significantly influence the sidewall angle and floor shape. Incorporating the CF_x radicals, on the other hand, increases the bottom roughness and the height difference between the microtrenches and the bottom center, as well as the sidewall angle. Interestingly, including the CF_x radicals without the F radicals prevents any etching, due to dominant deposition (not shown). Every considered step therefore has a noteworthy contribution to the trench shape. The surface chemistry set can thus not simply be reduced to ion-assisted chemical etching and direct reactive ion etching by CHF_3, Ar^+ and CF_3^+, without losing in information and accuracy. The latter three species, however, dominate the etch rate, as seen from the etch times in Figure 28.

Up to now, we only considered top-down experimental benchmarking of the model in terms of the etched feature profile. Another important aspect is the etch rate. In this respect, a stronger deviation with the experiments is found. Table VII compares the experimental etch rate with a few simulation

results. The original surface chemistry set of Section 4.2.2 overestimates the etch rate with a factor 3.9. This discrepancy can have different origins, each related to deviations in either the MCFPM input data or the surface chemistry set. Regarding the latter, the reaction probabilities for ion-assisted chemical etching and direct reactive ion etching may be overestimated in MCFPM. More specifically, such overestimation can be related to the CHF_3 physisorption or the Ar^+ and CF_3^+ etching probabilities, because these interactions determine the dominant etching mechanisms.

Table VII. Etch rate for a few investigated conditions, calculated at the center of the trench floor. Simulations were performed with the original surface chemistry set discussed in Section 4.2.2, with all plasma species and interactions enabled. This corresponds to the experiments, where an etch rate of 0.63 nm s^{-1} was measured. To study the influence of a surface mechanism, the corresponding reaction probabilities were rescaled with the listed multiplication factor.

	Adapted interaction probabilities	**Multiplication factor**	**Etch rate (nm s^{-1})**
Original surface mechanisms			
Original chemistry	none	-	2.48
Modified surface mechanism			
Physisorption	all	× 0.1	1.62
	all	× 0.01	1.38
Radical-emitting ion reactions	Ar^+ with $SiO_2CF_{x\,(s)}$	× 0.1	2.27
	Ar^+ and CF_x^+ with $SiO_2CF_{x\,(s)}$	× 0.1	2.03
Molecule-emitting ion reactions	Ar^+ with $SiO_2CF_{x\,(s)}$	× 0.1	1.05
	Ar^+ and CF_x^+ with $SiO_2CF_{x\,(s)}$	× 0.1	0.68
Radical- and molecule-emitting ion reactions	Ar^+ with $SiO_2CF_{x\,(s)}$	× 0.1	0.94
	Ar^+ and CF_x^+ with $SiO_2CF_{x\,(s)}$	× 0.1	0.50

However, this hypothesis could not be fully confirmed by means of MCFPM. As seen in Table VII and Figure 31, decreasing the physisorption probability with a factor 100 only led to a 1.9 times lower etch rate, while worsening the etched profile with deeper micro-trenching. Similar findings were obtained by reducing the Ar^+ and CF_3^+ etch probabilities for $SiO_2CF_{x\,(s)}$ surface groups (x = 0 to 4). When only the radical-emitting surface reactions are decreased in probability over one order of magnitude, the etch rate decreases only slightly. Lowering the probabilities of both the radical- and molecule-emitting surface reactions with a factor 10, on the other hand, brings the etch rate beneath the experimental value. However, this makes the sidewall angle contract significantly, causing a stronger deviation with the measured trench shape. Considering that the probabilities of the molecule-emitting reactions for Ar^+ and the CF_x^+ ions have been acquired from independent literature sources, a systematic overestimation of all of their values with a factor around 10 or even 5 seems unlikely. Still, a precise determination of the ion-assisted chemical etching yield for Ar^+ in the relevant energy range and for physisorbed CHF_3, instead of C_4F_8 as used in [283] (see step 30 in Section 4.2.2), is required to obtain more clarity.

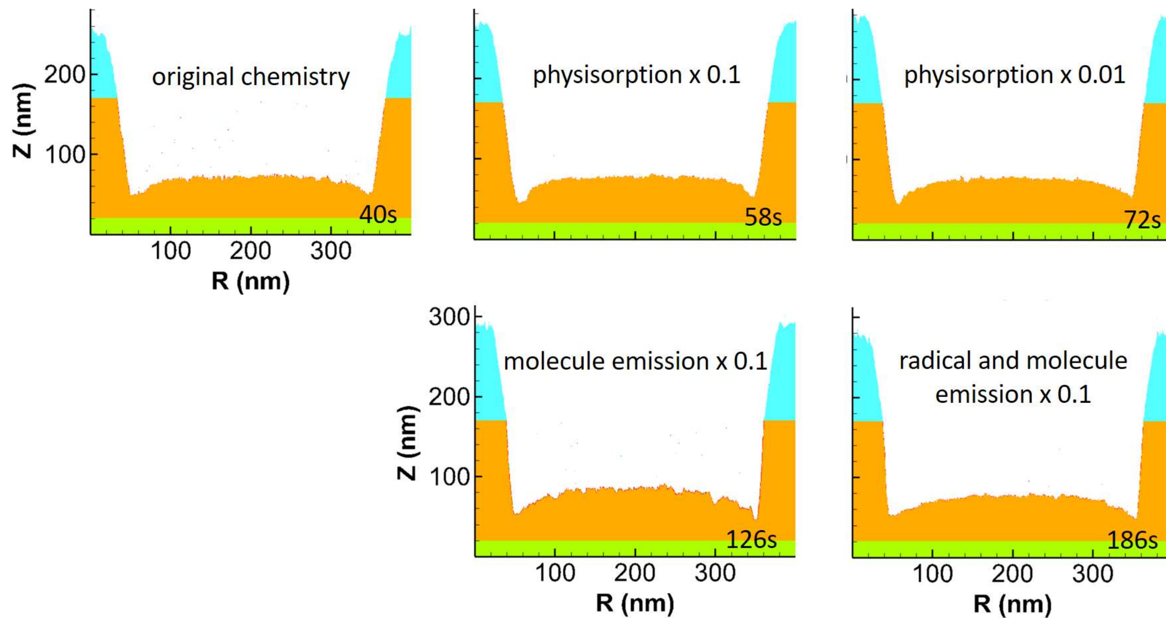

Figure 31. Simulated etched profiles for the original surface chemistry set and for adapted reaction probabilities as described in Table VII. For the bottom frames, the probabilities for both Ar^+ and CF_3^+ reactions were rescaled. The corresponding etch time is indicated in each frame.

As an additional and perhaps more plausible reason for the deviation from the experimental etch rate, inaccuracies may exist in the MCFPM input data. That is, the gas chemistry set in HPEM has not been experimentally benchmarked for the CCP reactor and operating conditions used. Overestimated ion energies or fluxes can, for instance, partly explain why the etch rate is overestimated. Since the ion energy already lies relatively low, it unlikely is the main cause, if it is any at all. According to the energy dependence of ion-assisted chemical etching by Ar^+ on $SiO_2CF_{y\,(s)}$ groups (for y = 0 to 4), as deduced in step 30 of Section 4.2.2, decreasing the ion energy from 320 eV to 130 eV only brings down the etch yield with a factor of 2.1. If the exponent in the relationship is assumed to be 1 instead of 0.5, the reduction factor becomes 4.2. Net deposition of CF_3^+ ions takes place below a threshold energy of 108 eV, in agreement with steps 29 and 33 in Section 4.2.2. An overestimation of the ion energy alone therefore cannot explain the discrepancy between the experimental and simulated etch rates, unless the ion energy is reduced to implausibly low values. This suggests to assume lower fluxes instead for further use of the surface chemistry set. Next to that, the emission of wafer material into the plasma gas was disregarded up to now, for the sake of simplicity. Including this effect into the gas and surface chemistries should lead to an additional decrease of the etch rate, due to redeposition of the wafer material.

Although the surface chemistry of the photoresist is implemented in a strongly simplified way, it performs remarkably well in the case of a more complex initial resist profile. Figure 32 displays the etching process for a resist profile with CD = 36 nm, which naturally exhibits a mushroom shape in a serial arrangement, originating from the lithography step. Also in this case, the original surface chemistry set predicts the final etched profile to a satisfying degree, with sidewall angles of 4.5° and 3.9° at the left and right side, respectively. A straightforward comparison with the experiment could not be made, because of the dissimilarities between neighboring etched trenches (see Figure 32). These dissimilarities are caused by an unidentified stochastic effect, despite the apparent regular initial photoresist structure. Possibly, tiny undetected differences in the initial structure can lead to the observed variation after etching.

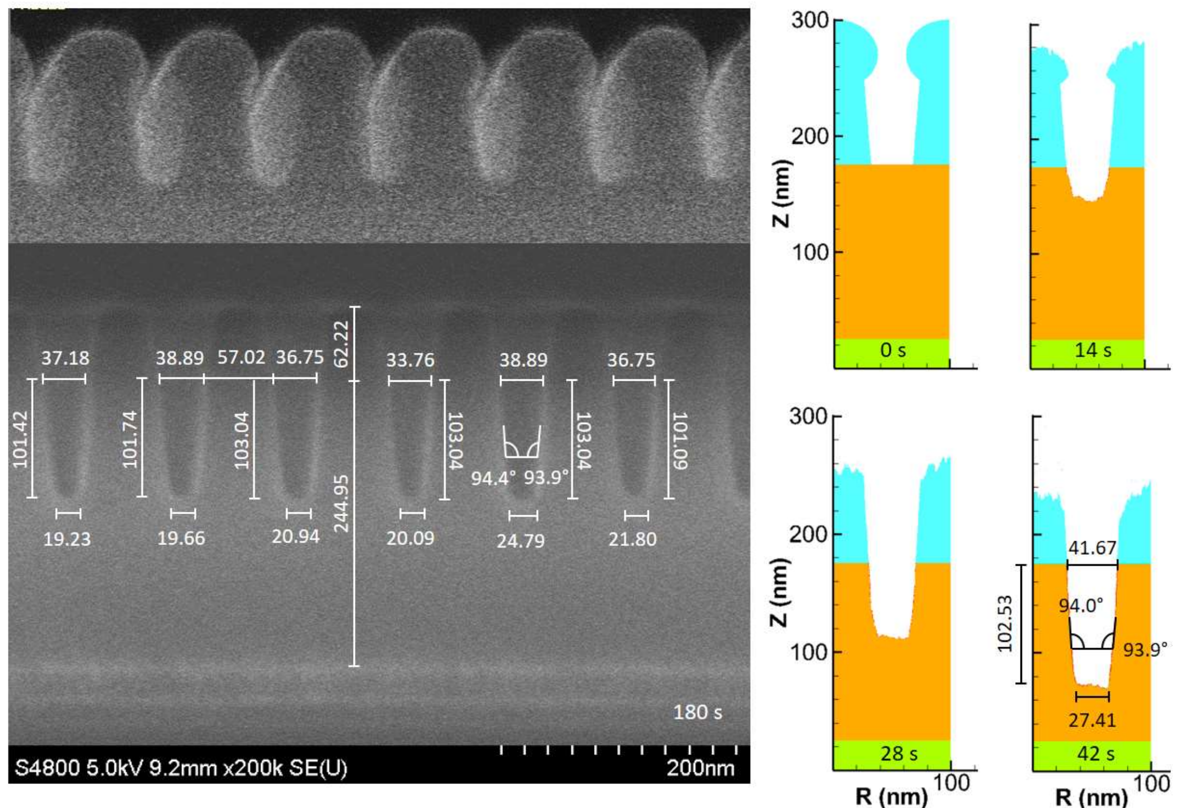

Figure 32. Initial and etched profiles for CD = 36 nm, (left) in the experiment and (right) according to the simulations with the original surface chemistry set. The etch time is indicated in the frames and the dimensions are expressed in nanometer.

Last, but not least, it is useful to compare the surface chemistry set with other sets presented in the scientific literature, dealing with the same plasma species and surface material (see e.g. [284, 306, 307]). As a main qualitative difference, all other sets assume physisorption of molecular species from the plasma to be absent. More specifically, the sets consider polymerization of the surface to originate exclusively from CF_x radicals. This makes an essential difference with the set designed in Section 4.2.2, which integrates molecule physisorption as one of the major mechanisms. Which of the two approaches corresponds best to the experimental surface mechanisms is currently a matter of speculation, and can only be resolved by additional dedicated experiments, probing the fundamentals of plasma-surface interaction. Yet, recent experimental studies and first-principles calculations on atomic layer etching of silicon nitride with CHF_3 indicate that physisorption may be a key mechanism even at room temperature and beyond [251, 252]. In contrast, chemisorption of CHF_3 does not significantly modify the surface and does not yield a stoichiometrically reasonable pathway for the etching [251]. We therefore conjecture that the same may be true for SiO_2 etching and other plasma-surface chemistries. Once more, this underlines the need for more fundamental investigations.

As another qualitative difference, other surface chemistry sets often consider the distinct $SiO_2CF_{x\ (s)}$ groups (with x = 0 to 3) as one and the same surface species and/or attribute them a common reaction probability with incoming ions, independent of the ion and the C/F ratio of the surface group (see e.g. [284, 306]). While this is an understandable simplification, it likely induces notable inaccuracies with regard to the experimental surface mechanisms. According to the set designed in Section 4.2.2, it will at least be useful to distinguish between F-poor and F-rich $SiO_2CF_{x\ (s)}$ groups, because they display considerable dissimilarities in chemistry. On the other hand, the set constructed in Section 4.2.2

disregards certain effects that are accounted for in other surface chemistry sets. Huard et al., for instance, take physisorption into account for the depositing radicals, by including surface diffusion followed by chemisorption in the MCFPM simulations [284]. This setting can prevent dendritic growth as a computational artifact, which is especially relevant in polymerizing plasmas. The absence of this setting in the case study may explain the bottom roughness induced by the CF_x radicals (Figure 28). Next to that, other sets generally include polymer activation by interaction with energetic ions (see e.g. [284, 306, 307]). This effect was omitted in our case study for the sake of simplicity, because the required quantitative data was not found in the literature. Perhaps, this deficiency causes, in part or entirely, some of the observed deviations with the experiments. We hope that this too will motivate plasma scientists and engineers to continue unraveling and quantifying the elementary mechanisms in plasma-surface interaction.

5. SUMMARY AND FUTURE OUTLOOK – LOOKING TOWARDS, BENEATH AND BEYOND THE SURFACE

In this review, we emphasized plasma-surface interaction physics and chemistry as an overarching domain with applications in many scientific areas, for which multiscale modeling serves as a universal simulation strategy. The physical and chemical processes underlying the plasma-surface interaction range over many orders of magnitude both in time and length scales, which cannot be captured with a single standard simulation technique. Instead, several standard simulation methods can be applied for the different decisive time and length scales, and coupled with one another in a multiscale model. The communication between some of the methods may occur by means of cyclic iterations in a single encompassing model, when the corresponding processes strongly influence each other. In other cases, a method functions as an autonomous model, providing input data to other models. Next to the classification of the methods based on the atomistic level, the mesoscale and the macroscale, they can also be distinguished according to the region they describe, i.e. the plasma, the plasma-solid interface and the solid.

Correspondingly, we have considered four classes. The solid phase is generally modeled by means of time-independent atomistic models, such as density functional theory, dynamic mean field theory, quantum Monte Carlo and the Bethe-Salpeter equation approach. The plasma-surface interface can be captured for the highest accuracy by time-dependent atomistic methods, including time-dependent density functional theory, Born-Oppenheimer, Car-Parrinello and classical molecular dynamics, the binary-collision approximation and non-equilibrium Green functions. Larger time and length scales become accessible for the interface through coarse-graining by means of mesoscopic models, like quantum kinetic methods based on the quantum Boltzmann equation, kinetic Monte Carlo and quasiparticle models. The plasma volume is described with macroscopic models, distinguished into fluid and kinetic methods, which can be combined in a hybrid model. These four classes also contain techniques that have not been explored yet for the study of plasma-surface interaction, or only to a limited degree, such as the lattice Boltzmann method and the vortex-in-cell method.

Next to the four classes of universal methods, multiscale modeling can also include application-specific techniques, e.g. simplified geometric procedures to rapidly calculate the surface profile evolution. Plasma sheath models form a special case with a crucial role in coupling the macroscale to the other classes. Despite their analytical or semi-analytical nature, many major developments in their understanding and implementation have only taken place throughout the past three decades. Another promising trend is the synergetic combination of multiscale modeling with data mining and machine learning, resulting from the complementary features of both computational strategies. Regarding the

standard and non-standardized methods, we believe that many opportunities currently present themselves to optimize plasma-surface interaction models and computational techniques. For this reason, we want to motivate astrophysicists, meteorologists, plasma scientists and engineers to explore these opportunities, by further developing, testing and comparing this numerical technology on the various levels of the multiscale modeling. Additionally, a close collaboration with experimentalists will strongly benefit this process, as measured data not only allows to verify the models, but also provides reliable checking points where the distinct methods in a multiscale model are coupled with one another.

As a concrete example, we discussed the design of a multiscale model for Si and SiO_2 wafer etching with fluorocarbon plasmas. The foundation of the multiscale model consists of the Hybrid Plasma Equipment Model (HPEM) combined with the Monte Carlo Feature Profile Model (MCFPM), both developed by the Kushner group. HPEM and MCFPM couple the macroscale and mesoscale processes of the plasma-surface interaction through a hybrid computational methodology, a semi-analytical sheath model and kinetic Monte Carlo simulations. The atomistic processes at the plasma-wafer interface are included by means of a user-defined surface chemistry set. In practice, up to now, such sets have primarily been designed by researchers and engineers in a top-down approach through trial-and-error, treating the surface mechanisms phenomenologically or disregarding them for a major part. While such procedure has been proven helpful and timesaving in the past to obtain approximate results, it reaches a bottleneck stage when a higher accuracy is demanded.

In contrast, we demonstrated the benefits and high potential of a bottom-up design approach, where every unique interaction between a plasma species and a surface group is implemented based on quantitative data from atomistic simulations or experiments. By keeping the number of assumptions, estimations and approximations to a minimum, inaccuracies in the set can more easily be identified, giving a higher transparency in the surface chemistry. Moreover, this design strategy automatically benchmarks the surface chemistry set on a fundamental level. Accordingly, the set immediately produces a satisfactory result, as shown by our simulations. Further fine-tuning of the set is performed subsequently through top-down benchmarking with experimental data for the complete plasma chemistry, in a more straightforward way as compared with the traditional approach. This permits computationally analyzing the plasma-surface interaction on a fundamental level and identifying the most crucial gaps in knowledge.

According to our simulations, the etched profile is strongly sensitive even to certain reactions involving surface groups with a low surface fraction. Each contributing mechanism therefore requires an accurate quantitative description, in order to obtain a trustworthy multiscale model. However, our investigation indicates a substantial lack of qualitative and quantitative data on the dominant plasma-surface interaction mechanisms, i.e. ion-assisted chemical etching and direct reactive ion etching. First of all, the angular and energy dependence of the corresponding etch yields are still largely unknown on the level of individual reactions, to which the simulated etched profiles and the etch rate are very sensitive, respectively. Secondly, many uncertainties especially remain on the mechanism and the reaction probabilities of ion-assisted chemical etching. Closely related to that, the probabilities of deposition (i.e. both physisorption and chemisorption) and chemical etching reactions by neutral species are partly uncertain yet. In this regard, we want to emphasize the importance of physisorption in ion-assisted chemical etching, as suggested by the recent studies in [251, 252]. This mechanism is considered in our surface chemistry set, contrary to sets previously proposed in the scientific literature. In general, most data available on plasma-surface interactions originates from experimental measurements, which did not resolve between individual surface groups, or from atomistic modeling studies, but seldom from both. Physical sputtering seems to be the only exception, on which a large

body of quantitative data can be found in literature. Since Si and SiO_2 etching with fluorocarbon plasmas knows a history of intense investigation, our case study suggests that similar deficiencies exist for most plasma-surface combinations, and for many applications and processes different from plasma etching. We therefore hope to motivate both computational and experimental scientists and engineers to collaborate on scrutinizing the elementary surface mechanisms further. In this way, plasma-surface modeling can progress through the aforementioned bottleneck stage, which we expect to occur for all relevant applications and processes.

AUTHOR'S CONTRIBUTIONS

Patrick Vanraes: Conceptualization, Data curation, Formal analysis, Funding acquisition, Computational and literature investigation, Methodology, Validation, Visualization, Writing - original draft. **Syam Parayil Venugopalan:** Conceptualization, Theoretical and experimental investigation, Methodology, Project administration, Resources, Funding acquisition, Supervision, Validation, Writing - review & editing. **Annemie Bogaerts:** Funding acquisition, Project administration, Resources, Supervision, Writing - review & editing.

SUPPLEMENTARY MATERIAL

See supplementary material for the gas chemistry subset of the Ar-related reactions and the complete surface chemistry set designed in Section 4.2.2.

ACKNOWLEDGMENTS

P. Vanraes acknowledges funding by ASML for the project "Computational simulation of plasma etching of trench structures". P. Vanraes wishes to thank Violeta Georgieva and Stefan Tinck for the fruitful discussions on the HPEM code, Yu-Ru Zhang for an example of the CCP reactor code and Karel Venken for his technical help with the server maintenance and use. P. Vanraes and A. Bogaerts want to express their gratitude to Mark J. Kushner (University of Michigan) for the sharing of the HPEM and MCFPM codes, and for the interesting exchange of views. S.P. Venugopalan wishes to thank Sander Wuister, Coen Verschuren, Michael Kubis, Mohammad Kamali, Katja Viatkina, Neungho Shin, Kuan-Ming Chen, Ruben Maas, Claire van Lare and Huaichen Zhang for the insightful discussions.

ROLE OF THE FUNDING SOURCE

This work was performed as a part of the project "Computational simulation of plasma etching of trench structures" funded by ASML, to investigate the physical principles of etch mechanisms and its impact on metrology marks.

DECLARATION OF COMPETING INTEREST

The authors declare the following financial interests/personal relationships which may be considered as potential competing interests: P. Vanraes is employed by the University of Antwerp, with funding by ASML for the project "Computational simulation of plasma etching of trench structures". S.P.

Venugopalan is employed by the ASML research department working on “physical modeling of plasma etching”.

AIP PUBLISHING DATA SHARING POLICY

The data that support the findings of this study are available from the corresponding author upon reasonable request.

REFERENCES

1. Bonitz, M., et al., *Towards an integrated modeling of the plasma-solid interface.* Frontiers of Chemical Science and Engineering, 2019. **13**(2): p. 201-237.
2. Marian, J., et al., *Recent advances in modeling and simulation of the exposure and response of tungsten to fusion energy conditions.* Nuclear Fusion, 2017. **57**(9): p. 092008.
3. Neyts, E.C. and P. Brault, *Molecular dynamics simulations for plasma-surface interactions.* Plasma Processes and Polymers, 2017. **14**(1-2): p. 1600145.
4. Nordlund, K., et al., *Multiscale modelling of plasma–wall interactions in fusion reactor conditions.* Journal of Physics D: Applied Physics, 2014. **47**(22): p. 224018.
5. Gordillo-Vazquez, F.J., V.J. Herrero, and I. Tanarro, *From Carbon Nanostructures to New Photoluminescence Sources: An Overview of New Perspectives and Emerging Applications of Low-Pressure PECVD.* Chemical Vapor Deposition, 2007. **13**(6-7): p. 267-279.
6. Grace, J.M. and L.J. Gerenser, *Plasma treatment of polymers.* Journal of dispersion science and technology, 2003. **24**(3-4): p. 305-341.
7. Graves, D.B. and P. Brault, *Molecular dynamics for low temperature plasma–surface interaction studies.* Journal of Physics D: Applied Physics, 2009. **42**(19): p. 194011.
8. von Keudell, A. and W. Jacob, *Elementary processes in plasma–surface interaction: H-atom and ion-induced chemisorption of methyl on hydrocarbon film surfaces.* Progress in surface science, 2004. **76**(1-2): p. 21-54.
9. Allain, J.P. and A. Shetty, *Unraveling atomic-level self-organization at the plasma-material interface.* Journal of Physics D: Applied Physics, 2017. **50**(28): p. 283002.
10. Chang, J. and J.P. Chang, *Achieving atomistic control in materials processing by plasma–surface interactions.* Journal of Physics D: Applied Physics, 2017. **50**(25): p. 253001.
11. Oehrlein, G.S. and S. Hamaguchi, *Foundations of low-temperature plasma enhanced materials synthesis and etching.* Plasma Sources Science and Technology, 2018. **27**(2): p. 023001.
12. Gou, F., A. Kleyn, and M. Gleeson, *The application of molecular dynamics to the study of plasma–surface interactions: CF x with silicon.* International Reviews in Physical Chemistry, 2008. **27**(2): p. 229-271.
13. Jones, G.H., et al., *The science of sungrazers, sunskirters, and other near-sun comets.* Space Science Reviews, 2018. **214**(1): p. 20.
14. McClanahan, T., et al., *Evidence for the sequestration of hydrogen-bearing volatiles towards the Moon’s southern pole-facing slopes.* Icarus, 2015. **255**: p. 88-99.
15. Vorburger, A., et al., *First direct observation of sputtered lunar oxygen.* Journal of Geophysical Research: Space Physics, 2014. **119**(2): p. 709-722.
16. Mann, I., N. Meyer-Vernet, and A. Czechowski, *Dust in the planetary system: Dust interactions in space plasmas of the solar system.* Physics reports, 2014. **536**(1): p. 1-39.
17. Izvekova, Y.N. and S. Popel, *Nonlinear Wave Structures and Plasma− Dust Effects in the Earth’s Atmosphere.* Plasma Physics Reports, 2018. **44**(9): p. 835-839.

18. Zalogin, G. and A. Kusov, *The solution of a model problem of the atmospheric entry of a small meteoroid.* Cosmic Research, 2016. **54**(2): p. 96-104.
19. Dimant, Y. and M.M. Oppenheim, *Formation of plasma around a small meteoroid: 1. Kinetic theory.* Journal of Geophysical Research: Space Physics, 2017. **122**(4): p. 4669-4696.
20. Surkov, V. and M. Hayakawa. *Underlying mechanisms of transient luminous events: a review*. in *Annales Geophysicae*. 2012. Copernicus GmbH.
21. Pasko, V.P., Y. Yair, and C.-L. Kuo, *Lightning related transient luminous events at high altitude in the Earth's atmosphere: Phenomenology, mechanisms and effects.* Space science reviews, 2012. **168**(1-4): p. 475-516.
22. Beers, C.J., et al., *Characterization of the helicon plasma flux to the target of Proto-MPEX.* Fusion Engineering and Design, 2019. **138**: p. 282-288.
23. Tolias, P., *On secondary electron emission and its semi-empirical description.* Plasma Physics and Controlled Fusion, 2014. **56**(12): p. 123002.
24. Rapp, J., *The challenges of plasma material interactions in nuclear fusion devices and potential solutions.* Fusion Science and Technology, 2017. **72**(3): p. 211-221.
25. Andruczyk, D., et al., *A Domestic Program for Liquid Metal PFC Research in Fusion.* Journal of Fusion Energy, 2020: p. 1-7.
26. Rezaei, F., et al., *Applications of plasma-liquid systems: A review.* Materials, 2019. **12**(17): p. 2751.
27. Khlyustova, A., et al., *Important parameters in plasma jets for the production of RONS in liquids for plasma medicine: A brief review.* Frontiers of Chemical Science and Engineering, 2019. **13**(2): p. 238-252.
28. Bernhardt, T., et al., *Plasma medicine: Applications of cold atmospheric pressure plasma in dermatology.* Oxidative medicine and cellular longevity, 2019. **2019**.
29. Yan, X., et al., *Plasma medicine for neuroscience—An introduction.* Chinese Neurosurgical Journal, 2019. **5**(1): p. 1-8.
30. Ranieri, P., et al., *Plasma agriculture: Review from the perspective of the plant and its ecosystem.* Plasma Processes and Polymers, 2021. **18**(1): p. 2000162.
31. Vanraes, P. and A. Bogaerts, *Laser-induced excitation mechanisms and phase transitions in spectrochemical analysis–Review of the fundamentals.* Spectrochimica Acta Part B: Atomic Spectroscopy, 2021. **179**: p. 106091.
32. Altieri, N.D., et al., *Plasma–surface interactions at the atomic scale for patterning metals.* Journal of Vacuum Science & Technology A: Vacuum, Surfaces, and Films, 2017. **35**(5): p. 05C203.
33. Boris, D.R., et al., *The role of plasma in plasma-enhanced atomic layer deposition of crystalline films.* Journal of Vacuum Science & Technology A: Vacuum, Surfaces, and Films, 2020. **38**(4): p. 040801.
34. Vesel, A. and M. Mozetic, *New developments in surface functionalization of polymers using controlled plasma treatments.* Journal of Physics D: Applied Physics, 2017. **50**(29): p. 293001.
35. Vandenabeele, C.R. and S. Lucas, *Technological challenges and progress in nanomaterials plasma surface modification–a review.* Materials Science and Engineering: R: Reports, 2020. **139**: p. 100521.
36. Maitre, P.-A., M.S. Bieniek, and P.N. Kechagiopoulos, *Plasma-enhanced catalysis for the upgrading of methane: a review of modelling and simulation methods.* Reaction Chemistry & Engineering, 2020. **5**(5): p. 814-837.
37. Neyts, E. and A. Bogaerts, *Understanding plasma catalysis through modelling and simulation—a review.* Journal of Physics D: Applied Physics, 2014. **47**(22): p. 224010.
38. Barabash, S., et al., *Investigation of the solar wind–Moon interaction onboard Chandrayaan-1 mission with the SARA experiment.* Current Science, 2009: p. 526-532.
39. Farrell, W., et al., *Anticipated electrical environment within permanently shadowed lunar craters.* Journal of Geophysical Research: Planets, 2010. **115**(E3).

40. Killen, R., D. Hurley, and W.M. Farrell, *The effect on the lunar exosphere of a coronal mass ejection passage.* Journal of Geophysical Research: Planets, 2012. **117**(E10).
41. Futaana, Y., et al., *Empirical energy spectra of neutralized solar wind protons from the lunar regolith.* Journal of Geophysical Research: Planets, 2012. **117**(E5).
42. Harada, Y., et al., *Backscattered energetic neutral atoms from the Moon in the Earth's plasma sheet observed by Chandarayaan-1/Sub-keV Atom Reflecting Analyzer instrument.* Journal of Geophysical Research: Space Physics, 2014. **119**(5): p. 3573-3584.
43. Bhardwaj, A., et al., *Interaction of solar wind with Moon: An overview on the results from the SARA experiment aboard Chandrayaan-1.* Advances in Geosciences: Volume 30: Planetary Science (PS) and Solar & Terrestrial Science (ST), 2012: p. 35-55.
44. Saul, L., et al., *Solar wind reflection from the lunar surface: The view from far and near.* Planetary and space science, 2013. **84**: p. 1-4.
45. McComas, D., et al., *Lunar backscatter and neutralization of the solar wind: First observations of neutral atoms from the Moon.* Geophysical Research Letters, 2009. **36**(12).
46. Rodriguez, M.D.F., et al., *IBEX-Lo observations of energetic neutral hydrogen atoms originating from the lunar surface.* Planetary and space science, 2012. **60**(1): p. 297-303.
47. Kushner, M.J., *Hybrid modelling of low temperature plasmas for fundamental investigations and equipment design.* Journal of Physics D: Applied Physics, 2009. **42**(19): p. 194013.
48. Bhoj, A.N. and M.J. Kushner, *Repetitively pulsed atmospheric pressure discharge treatment of rough polymer surfaces: II. Treatment of micro-beads in He/NH3/H2O and He/O2/H2O mixtures.* Plasma Sources Science and Technology, 2008. **17**(3): p. 035025.
49. Bhoj, A.N. and M.J. Kushner, *Repetitively pulsed atmospheric pressure discharge treatment of rough polymer surfaces: I. Humid air discharges.* Plasma sources science and technology, 2008. **17**(3): p. 035024.
50. Xiao, T. and D. Ni, *Multiscale Modeling and Recurrent Neural Network Based Optimization of a Plasma Etch Process.* Processes, 2021. **9**(1): p. 151.
51. Kwon, U.H. and W.J. Lee, *Multiscale Monte Carlo simulation of circular DC magnetron sputtering: influence of magnetron design on target erosion and film deposition.* Japanese journal of applied physics, 2006. **45**(11R): p. 8629.
52. Dybyspayeva, K., et al. *Multiscale simulation of ion beam impacts on a graphene surface*. in *Journal of Physics: Conference Series*. 2016. IOP Publishing.
53. Bali, N., et al., *Modeling of a DBD plasma reactor for porous soil remediation.* Chemical Engineering Journal, 2019. **373**: p. 393-405.
54. Crose, M., et al., *Multiscale three-dimensional CFD modeling for PECVD of amorphous silicon thin films.* Computers & Chemical Engineering, 2018. **113**: p. 184-195.
55. Schneider, R., *Plasma–wall interaction: a multiscale problem.* Physica Scripta, 2006. **2006**(T124): p. 76.
56. Buesser, B. and S.E. Pratsinis, *Design of nanomaterial synthesis by aerosol processes.* Annual review of chemical and biomolecular engineering, 2012. **3**: p. 103-127.
57. Groh, S. and H. Zbib, *Advances in discrete dislocations dynamics and multiscale modeling.* Journal of Engineering Materials and Technology, 2009. **131**(4).
58. Li, S. and S. Urata, *An atomistic-to-continuum molecular dynamics: Theory, algorithm, and applications.* Computer Methods in Applied Mechanics and Engineering, 2016. **306**: p. 452-478.
59. Pereira, S.P., et al., *Multiscale modeling of polymer/clay nanocomposites.* Journal of Multiscale Modelling, 2011. **3**(03): p. 151-176.
60. Neyts, E.C., et al., *Computer simulations of plasma–biomolecule and plasma–tissue interactions for a better insight in plasma medicine.* Journal of Physics D: Applied Physics, 2014. **47**(29): p. 293001.
61. Kryachko, E.S. and E.V. Ludena, *Density functional theory: Foundations reviewed.* Physics Reports, 2014. **544**(2): p. 123-239.

62. Morgante, P. and R. Peverati, *The devil in the details: A tutorial review on some undervalued aspects of density functional theory calculations.* International Journal of Quantum Chemistry, 2020. **120**(18): p. e26332.
63. Capelle, K., *A bird's-eye view of density-functional theory.* Brazilian journal of physics, 2006. **36**(4A): p. 1318-1343.
64. Neyts, E.C., A.C. Van Duin, and A. Bogaerts, *Insights in the plasma-assisted growth of carbon nanotubes through atomic scale simulations: effect of electric field.* Journal of the American Chemical Society, 2012. **134**(2): p. 1256-1260.
65. Jafarzadeh, A., et al., *Activation of CO2 on Copper Surfaces: The Synergy between Electric Field, Surface Morphology, and Excess Electrons.* The Journal of Physical Chemistry C, 2020. **124**(12): p. 6747-6755.
66. Wang, W., et al., *First principles study of Si etching by CHF3 plasma source.* Applied surface science, 2011. **257**(21): p. 8767-8771.
67. Blöchl, P.E., *Projector augmented-wave method.* Physical review B, 1994. **50**(24): p. 17953.
68. Powell, B. and R.H. McKenzie, *Strong electronic correlations in superconducting organic charge transfer salts.* Journal of Physics: Condensed Matter, 2006. **18**(45): p. R827.
69. Georges, A., L.d. Medici, and J. Mravlje, *Strong correlations from Hund's coupling.* Annu. Rev. Condens. Matter Phys., 2013. **4**(1): p. 137-178.
70. Kotliar, G., et al., *Electronic structure calculations with dynamical mean-field theory.* Reviews of Modern Physics, 2006. **78**(3): p. 865.
71. Paul, A. and T. Birol, *Applications of DFT+ DMFT in materials science.* Annual Review of Materials Research, 2019. **49**: p. 31-52.
72. Held, K., *Electronic structure calculations using dynamical mean field theory.* Advances in physics, 2007. **56**(6): p. 829-926.
73. Kuneš, J. and V. Anisimov, *Various scenarios of metal-insulator transition in strongly correlated materials.* Annalen der Physik, 2011. **523**(8-9): p. 682-688.
74. Skornyakov, S. and V. Anisimov, *Computation of electronic structure and magnetic properties of strongly correlated materials with LDA+ DMFT method.* Philosophical Magazine, 2015. **95**(12): p. 1244-1259.
75. Kuchinskii, E.Z., I.A. Nekrasov, and M.V. Sadovskii, *Generalized dynamical mean-field theory in the physics of strongly correlated systems.* Physics-Uspekhi, 2012. **55**(4): p. 325.
76. Schüler, M., et al., *Realistic theory of electronic correlations in nanoscopic systems.* The European Physical Journal Special Topics, 2017. **226**(11): p. 2615-2640.
77. Rohringer, G., et al., *Diagrammatic routes to nonlocal correlations beyond dynamical mean field theory.* Reviews of Modern Physics, 2018. **90**(2): p. 025003.
78. Ceperley, D.M., *Theoretical and Computational Methods in Mineral Physics*, in *6. An Overview of Quantum Monte Carlo Methods*, M.W. Renata and S. Lars, Editors. 2018, De Gruyter. p. 129-136.
79. Foulkes, W., et al., *Quantum Monte Carlo simulations of solids.* Reviews of Modern Physics, 2001. **73**(1): p. 33.
80. Shumway, J. and D. Ceperley, *Quantum Monte Carlo methods in the study of nanostructures.* Quantum, 2004. **1**: p. 605.
81. Nakano, K., et al., *TurboRVB: A many-body toolkit for ab initio electronic simulations by quantum Monte Carlo.* The Journal of Chemical Physics, 2020. **152**(20): p. 204121.
82. Brown, E., et al., *Quantum Monte Carlo techniques and applications for warm dense matter*, in *Frontiers and Challenges in Warm Dense Matter*. 2014, Springer. p. 123-149.
83. Pollet, L., *Recent developments in quantum Monte Carlo simulations with applications for cold gases.* Reports on progress in physics, 2012. **75**(9): p. 094501.
84. Motta, M. and S. Zhang, *Ab initio computations of molecular systems by the auxiliary-field quantum Monte Carlo method.* Wiley Interdisciplinary Reviews: Computational Molecular Science, 2018. **8**(5): p. e1364.

85. Zhang, S., *Ab initio electronic structure calculations by auxiliary-field quantum Monte Carlo.* Handbook of Materials Modeling: Methods: Theory and Modeling, 2020: p. 123-149.
86. Onida, G., L. Reining, and A. Rubio, *Electronic excitations: density-functional versus many-body Green's-function approaches.* Reviews of modern physics, 2002. **74**(2): p. 601.
87. Huang, P. and E.A. Carter, *Advances in correlated electronic structure methods for solids, surfaces, and nanostructures.* Annu. Rev. Phys. Chem., 2008. **59**: p. 261-290.
88. Blase, X., et al., *The Bethe–Salpeter Equation Formalism: From Physics to Chemistry.* The Journal of Physical Chemistry Letters, 2020. **11**(17): p. 7371-7382.
89. Jacquemin, D., I. Duchemin, and X. Blase, *Is the Bethe–Salpeter formalism accurate for excitation energies? Comparisons with TD-DFT, CASPT2, and EOM-CCSD.* The journal of physical chemistry letters, 2017. **8**(7): p. 1524-1529.
90. Li, J., et al., *Ground-state correlation energy of beryllium dimer by the Bethe-Salpeter equation.* SciPost Phys, 2020. **8**: p. 20.
91. Loos, P.-F., et al., *Pros and Cons of the Bethe–Salpeter Formalism for Ground-State Energies.* The journal of physical chemistry letters, 2020. **11**(9): p. 3536-3545.
92. Maitra, N.T., *Perspective: Fundamental aspects of time-dependent density functional theory.* The Journal of Chemical Physics, 2016. **144**(22): p. 220901.
93. Ullrich, C.A. and Z.-h. Yang, *A brief compendium of time-dependent density functional theory.* Brazilian Journal of Physics, 2014. **44**(1): p. 154-188.
94. Adamo, C. and D. Jacquemin, *The calculations of excited-state properties with Time-Dependent Density Functional Theory.* Chemical Society Reviews, 2013. **42**(3): p. 845-856.
95. Byun, Y.-M., J. Sun, and C.A. Ullrich, *Time-dependent density-functional theory for periodic solids: assessment of excitonic exchange–correlation kernels.* Electronic Structure, 2020. **2**(2): p. 023002.
96. Schlünzen, N., et al., *Time-dependent simulation of ion stopping: Charge transfer and electronic excitations.* Contributions to Plasma Physics, 2019. **59**(6): p. e201800184.
97. Thar, J., W. Reckien, and B. Kirchner, *Car–Parrinello molecular dynamics simulations and biological systems*, in *Atomistic Approaches in Modern Biology. Topics in Current Chemistry*, M. Reiher, Editor. 2006, Springer: Berlin, Heidelberg. p. 133-171.
98. Kühne, T.D., *Second generation Car–Parrinello molecular dynamics.* Wiley Interdisciplinary Reviews: Computational Molecular Science, 2014. **4**(4): p. 391-406.
99. Boero, M. and A. Oshiyama, *Car–Parrinello Molecular Dynamics*, in *Encyclopedia of Nanotechnology*, B. Bhushan, Editor. 2014, Springer Netherlands: Dordrecht. p. 1-10.
100. Alves, L., et al., *Foundations of modelling of nonequilibrium low-temperature plasmas.* Plasma Sources Science and Technology, 2018. **27**(2): p. 023002.
101. Fukuhara, S., et al., *Accelerated molecular dynamics simulation of large systems with parallel collective variable-driven hyperdynamics.* Computational Materials Science, 2020. **177**: p. 109581.
102. Bal, K.M. and E.C. Neyts, *Merging metadynamics into hyperdynamics: accelerated molecular simulations reaching time scales from microseconds to seconds.* Journal of chemical theory and computation, 2015. **11**(10): p. 4545-4554.
103. Nakano, A., et al., *De novo ultrascale atomistic simulations on high-end parallel supercomputers.* The International Journal of High Performance Computing Applications, 2008. **22**(1): p. 113-128.
104. Rino, J.P., P.S. Branício, and D.S. Borges. *Classical molecular dynamics simulation of structural and dynamical properties of II-VI and III-V semiconductors*. in *Defect and Diffusion Forum*. 2006. Trans Tech Publ.
105. Brommer, P., et al., *Classical interaction potentials for diverse materials from ab initio data: a review of potfit.* Modelling and Simulation in Materials Science and Engineering, 2015. **23**(7): p. 074002.

106. Gissinger, J.R., B.D. Jensen, and K.E. Wise, *Modeling chemical reactions in classical molecular dynamics simulations.* Polymer, 2017. **128**: p. 211-217.
107. Xie, Q. and R. Tinker, *Molecular dynamics simulations of chemical reactions for use in education.* Journal of Chemical Education, 2006. **83**(1): p. 77.
108. Tan, O.Z., et al., *Physisorption structure of water on the GaN polar surface: force field development and molecular dynamics simulations.* The Journal of Physical Chemistry C, 2011. **115**(23): p. 11684-11693.
109. Michoulier, E., et al., *Adsorption of PAHs on interstellar ice viewed by classical molecular dynamics.* Physical Chemistry Chemical Physics, 2018. **20**(13): p. 8753-8764.
110. Nordlund, K., *Molecular dynamics simulation of ion ranges in the 1–100 keV energy range.* Computational materials science, 1995. **3**(4): p. 448-456.
111. Ziegler, J.F. and J.P. Biersack, *The stopping and range of ions in matter*, in *Treatise on heavy-ion science*. 1985, Springer. p. 93-129.
112. Lorenz, C. and N.L. Doltsinis, *Molecular dynamics simulation: from "ab initio" to "coarse grained".* Handbook of Computational Chemistry, Springer Netherlands, 2012: p. 195-238.
113. Bogaerts, A., et al., *Computer Modeling of Plasmas and Plasma-Surface Interactions.* Plasma Processes and Polymers, 2009. **6**(5): p. 295-307.
114. Smith, R., *Atomic and ion collisions in solids and at surfaces*. 1997.
115. Robinson, M.T. and I.M. Torrens, *Computer simulation of atomic-displacement cascades in solids in the binary-collision approximation.* Physical Review B, 1974. **9**(12): p. 5008.
116. Hirsbrunner, M.R., et al., *A review of modeling interacting transient phenomena with non-equilibrium Green functions.* Reports on Progress in Physics, 2019. **82**(4): p. 046001.
117. Schlünzen, N., et al., *Ultrafast dynamics of strongly correlated fermions—nonequilibrium Green functions and selfenergy approximations.* Journal of Physics: Condensed Matter, 2019. **32**(10): p. 103001.
118. Guerra, V. and D. Marinov, *Dynamical Monte Carlo methods for plasma-surface reactions.* Plasma Sources Science and Technology, 2016. **25**(4): p. 045001.
119. Marinov, D., C. Teixeira, and V. Guerra, *Deterministic and Monte Carlo methods for simulation of plasma-surface interactions.* Plasma Processes and Polymers, 2017. **14**(1-2): p. 1600175.
120. Remsing, R.C. and J.E. Bates, *Effective mass path integral simulations of quasiparticles in condensed phases.* The Journal of Chemical Physics, 2020. **153**(12): p. 121104.
121. Rivera, N. and I. Kaminer, *Light–matter interactions with photonic quasiparticles.* Nature Reviews Physics, 2020. **2**(10): p. 538-561.
122. Wölfle, P., *Quasiparticles in condensed matter systems.* Reports on Progress in Physics, 2018. **81**(3): p. 032501.
123. Laikhtman, B., *Are excitons really bosons?* Journal of Physics: Condensed Matter, 2007. **19**(29): p. 295214.
124. Ramanathan, R., et al., *Criteria for two distinguishable fermions to form a boson.* Physical Review A, 2011. **84**(3): p. 034304.
125. Carpene, E., *Ultrafast laser irradiation of metals: Beyond the two-temperature model.* Physical Review B, 2006. **74**(2): p. 024301.
126. Naldo, S.B., A.V. Bernotas, and B.F. Donovan, *Understanding the sensitivity of the two-temperature model for electron–phonon coupling measurements.* Journal of Applied Physics, 2020. **128**(8): p. 085102.
127. Chen, J., D. Tzou, and J. Beraun, *A semiclassical two-temperature model for ultrafast laser heating.* International journal of heat and mass transfer, 2006. **49**(1-2): p. 307-316.
128. Hull, D. and D.J. Bacon, *Introduction to dislocations*. 2001: Butterworth-Heinemann.
129. Anderson, P.M., J.P. Hirth, and J. Lothe, *Theory of dislocations*. 2017: Cambridge University Press.

130. Po, G., et al., *Recent progress in discrete dislocation dynamics and its applications to micro plasticity.* Jom, 2014. **66**(10): p. 2108-2120.
131. Lavenstein, S. and J.A. El-Awady, *Micro-scale fatigue mechanisms in metals: Insights gained from small-scale experiments and discrete dislocation dynamics simulations.* Current Opinion in Solid State and Materials Science, 2019. **23**(5): p. 100765.
132. Venugopalan, S. and L. Nicola, *Indentation of a plastically deforming metal crystal with a self-affine rigid surface: A dislocation dynamics study.* Acta Materialia, 2019. **165**: p. 709-721.
133. Venugopalan, S., N. Irani, and L. Nicola, *Plastic contact of self-affine surfaces: Persson's theory versus discrete dislocation plasticity.* Journal of the Mechanics and Physics of Solids, 2019. **132**: p. 103676.
134. Kim, H., et al., *Particle and fluid simulations of low-temperature plasma discharges: benchmarks and kinetic effects.* Journal of Physics D: Applied Physics, 2005. **38**(19): p. R283.
135. Jeong, W. and J. Seong, *Comparison of effects on technical variances of computational fluid dynamics (CFD) software based on finite element and finite volume methods.* International Journal of Mechanical Sciences, 2014. **78**: p. 19-26.
136. Zawawi, M.H., et al. *A review: Fundamentals of computational fluid dynamics (CFD)*. in *AIP Conference Proceedings*. 2018. AIP Publishing LLC.
137. Surana, K., et al., *k-version of finite element method in gas dynamics: higher-order global differentiability numerical solutions.* International journal for numerical methods in engineering, 2007. **69**(6): p. 1109-1157.
138. Prasanth, P. and J.K. Kakkassery, *Direct simulation Monte Carlo (DSMC): A numerical method for transition-regime flows-A review.* Journal of the Indian Institute of Science, 2006. **86**(3): p. 169.
139. Oran, E., C. Oh, and B. Cybyk, *Direct simulation Monte Carlo: recent advances and applications.* Annual Review of Fluid Mechanics, 1998. **30**(1): p. 403-441.
140. Vahedi, V. and M. Surendra, *A Monte Carlo collision model for the particle-in-cell method: applications to argon and oxygen discharges.* Computer Physics Communications, 1995. **87**(1-2): p. 179-198.
141. Taccogna, F., *Monte Carlo Collision method for low temperature plasma simulation.* J. Plasma Phys, 2015. **81**(1): p. 305810102.
142. Davidson, P.A., *An Introduction to Magnetohydrodynamics.* American Journal of Physics, 2002. **70**(7): p. 781-781.
143. Wang, C., et al., *Magnetohydrodynamics (MHD) numerical simulations on the interaction of the solar wind with the magnetosphere: A review.* Science China Earth Sciences, 2013. **56**(7): p. 1141-1157.
144. Zheng, L., *Advanced Tokamak Stability Theory*. IOP Concise Physics. 2015, 40 Oak Drive, San Rafael, CA, 94903, USA: Morgan & Claypool Publishers.
145. Fasoli, A., et al., *Computational challenges in magnetic-confinement fusion physics.* Nature Physics, 2016. **12**(5): p. 411-423.
146. Garbet, X., et al., *Gyrokinetic simulations of turbulent transport.* Nuclear Fusion, 2010. **50**(4): p. 043002.
147. Bottino, A. and E. Sonnendrücker, *Monte Carlo particle-in-cell methods for the simulation of the Vlasov–Maxwell gyrokinetic equations.* Journal of Plasma Physics, 2015. **81**(5).
148. Passot, T. and P. Sulem, *Collisionless magnetohydrodynamics with gyrokinetic effects.* Physics of Plasmas, 2007. **14**(8): p. 082502.
149. Wang, X., et al., *An extended hybrid magnetohydrodynamics gyrokinetic model for numerical simulation of shear Alfvén waves in burning plasmas.* Physics of Plasmas, 2011. **18**(5): p. 052504.
150. Lee, W., S. Hudson, and C. Ma, *Gyrokinetic magnetohydrodynamics and the associated equilibria.* Physics of Plasmas, 2017. **24**(12): p. 124508.

151. Sugiyama, T. and K. Kusano, *Multi-scale plasma simulation by the interlocking of magnetohydrodynamic model and particle-in-cell kinetic model.* Journal of Computational Physics, 2007. **227**(2): p. 1340-1352.
152. Brandt, T., et al., *Magnetohydrodynamics and particle-in-cell codes simulation of plasma processes in micro HEMP-Thrusters.* 2013.
153. González, C., et al., *Turbulent electromagnetic fields at sub-proton scales: Two-fluid and full-kinetic plasma simulations.* Physics of Plasmas, 2019. **26**(1): p. 012306.
154. Schneider, R. and R. Kleiber, *Computational plasma physics*, in *Plasma Physics*. 2005, Springer. p. 425-443.
155. Murphy, A.B. and H. Park, *Modeling of Thermal Plasma Processes: The Importance of Two-Way Plasma-Surface Interactions.* Plasma Processes and Polymers, 2017. **14**(1-2): p. 1600177.
156. Echenique, P. and J.L. Alonso, *A mathematical and computational review of Hartree–Fock SCF methods in quantum chemistry.* Molecular Physics, 2007. **105**(23-24): p. 3057-3098.
157. Lonsdale, R., J.N. Harvey, and A.J. Mulholland, *A practical guide to modelling enzyme-catalysed reactions.* Chemical Society Reviews, 2012. **41**(8): p. 3025-3038.
158. Paulus, B., *The method of increments—a wavefunction-based ab initio correlation method for solids.* Physics reports, 2006. **428**(1): p. 1-52.
159. Bouvard, J.-L., et al., *Review of hierarchical multiscale modeling to describe the mechanical behavior of amorphous polymers.* Journal of Engineering Materials and Technology, 2009. **131**(4).
160. Succi, S., R. Benzi, and F. Higuera, *The lattice Boltzmann equation: a new tool for computational fluid-dynamics.* Physica D: Nonlinear Phenomena, 1991. **47**(1-2): p. 219-230.
161. Haenel, D. and O. Filippova, *Lattice-Boltzmann methods—a new tool in CFD*, in *Computational Fluid Dynamics for the 21st Century*. 2001, Springer. p. 117-132.
162. Tran, N.-P., M. Lee, and D.H. Choi. *Memory-efficient parallelization of 3D lattice Boltzmann flow solver on a GPU*. in *2015 IEEE 22nd International Conference on High Performance Computing (HiPC)*. 2015. IEEE.
163. Liu, S., et al. *Accelerating the parallelization of lattice boltzmann method by exploiting the temporal locality*. in *2017 IEEE International Symposium on Parallel and Distributed Processing with Applications and 2017 IEEE International Conference on Ubiquitous Computing and Communications (ISPA/IUCC)*. 2017. IEEE.
164. Zhou, H., et al., *GPU implementation of lattice Boltzmann method for flows with curved boundaries.* Computer Methods in Applied Mechanics and Engineering, 2012. **225**: p. 65-73.
165. Yu, H., et al., *Mass-conserved volumetric lattice Boltzmann method for complex flows with willfully moving boundaries.* Physical Review E, 2014. **89**(6): p. 063304.
166. Kang, S.K. and Y.A. Hassan, *A comparative study of direct-forcing immersed boundary-lattice Boltzmann methods for stationary complex boundaries.* International Journal for Numerical Methods in Fluids, 2011. **66**(9): p. 1132-1158.
167. Tiwari, A. and S.P. Vanka, *A ghost fluid Lattice Boltzmann method for complex geometries.* International Journal for Numerical Methods in Fluids, 2012. **69**(2): p. 481-498.
168. Chen, Z., et al., *Simplified multiphase lattice Boltzmann method for simulating multiphase flows with large density ratios and complex interfaces.* Physical Review E, 2018. **98**(6): p. 063314.
169. Zhang, J., *Lattice Boltzmann method for microfluidics: models and applications.* Microfluidics and Nanofluidics, 2011. **10**(1): p. 1-28.
170. He, X. and G.D. Doolen, *Thermodynamic foundations of kinetic theory and lattice Boltzmann models for multiphase flows.* Journal of Statistical Physics, 2002. **107**(1): p. 309-328.
171. Wang, H., et al., *A brief review of the phase-field-based lattice Boltzmann method for multiphase flows.* Capillarity, 2019. **2**(3): p. 33-52.

172. Li, Z., M. Yang, and Y. Zhang, *A hybrid lattice Boltzmann and Monte Carlo method for natural convection simulation.* International Journal for Multiscale Computational Engineering, 2015. **13**(4).
173. Di Staso, G., et al., *Lattice Boltzmann accelerated direct simulation Monte Carlo for dilute gas flow simulations.* Philosophical Transactions of the Royal Society A: Mathematical, Physical and Engineering Sciences, 2016. **374**(2080): p. 20160226.
174. Di Staso, G., et al., *Hybrid lattice Boltzmann-direct simulation Monte Carlo approach for flows in three-dimensional geometries.* Computers & Fluids, 2018. **172**: p. 492-509.
175. Di Staso, G., et al. *Hybrid lattice Boltzmann-Direct Simulation Monte Carlo approach for non-equilibrium flows in complex geometries*. in *3rd European Conference on Non-Equilibrium Gas Flows (NEGF18)*. 2018.
176. Nabovati, A., D.P. Sellan, and C.H. Amon, *On the lattice Boltzmann method for phonon transport.* Journal of Computational Physics, 2011. **230**(15): p. 5864-5876.
177. Zhang, H., et al., *Modeling and simulation of plasma jet by lattice Boltzmann method.* Applied Mathematical Modelling, 2007. **31**(6): p. 1124-1132.
178. Zhang, X., Y. Deguchi, and J. Liu, *Numerical simulation of laser induced weakly ionized helium plasma process by lattice Boltzmann method.* Japanese Journal of Applied Physics, 2012. **51**(1S): p. 01AA04.
179. Wang, H., *Numerical simulation of the ion-acoustic solitary waves in plasma based on lattice Boltzmann method.* Advances in Space Research, 2015. **56**(6): p. 1161-1168.
180. Kono, M., et al., *Vortex dynamics in magnetized plasmas.* Physica Scripta, 1998. **58**(3): p. 238.
181. Hosain, M.L. and R.B. Fdhila, *Literature review of accelerated CFD simulation methods towards online application.* Energy Procedia, 2015. **75**: p. 3307-3314.
182. Matouš, K., et al., *A review of predictive nonlinear theories for multiscale modeling of heterogeneous materials.* Journal of Computational Physics, 2017. **330**: p. 192-220.
183. Schleder, G.R., et al., *From DFT to machine learning: recent approaches to materials science–a review.* Journal of Physics: Materials, 2019. **2**(3): p. 032001.
184. Alber, M., et al., *Integrating machine learning and multiscale modeling—perspectives, challenges, and opportunities in the biological, biomedical, and behavioral sciences.* NPJ digital medicine, 2019. **2**(1): p. 1-11.
185. Verkhivker, G.M., et al., *Allosteric regulation at the crossroads of new technologies: multiscale modeling, networks, and machine learning.* Frontiers in Molecular Biosciences, 2020. **7**.
186. Peng, G.C., et al., *Multiscale modeling meets machine learning: What can we learn?* Archives of Computational Methods in Engineering, 2021. **28**(3): p. 1017-1037.
187. Haghighatlari, M. and J. Hachmann, *Advances of machine learning in molecular modeling and simulation.* Current Opinion in Chemical Engineering, 2019. **23**: p. 51-57.
188. Wang, Y., J.M.L. Ribeiro, and P. Tiwary, *Machine learning approaches for analyzing and enhancing molecular dynamics simulations.* Current opinion in structural biology, 2020. **61**: p. 139-145.
189. Krüger, F., T. Gergs, and J. Trieschmann, *Machine learning plasma-surface interface for coupling sputtering and gas-phase transport simulations.* Plasma Sources Science and Technology, 2019. **28**(3): p. 035002.
190. Baalrud, S.D., et al., *Interaction of biased electrodes and plasmas: sheaths, double layers, and fireballs.* Plasma Sources Science and Technology, 2020. **29**(5): p. 053001.
191. Baalrud, S., N. Hershkowitz, and B. Longmier, *Global nonambipolar flow: Plasma confinement where all electrons are lost to one boundary and all positive ions to another boundary.* Physics of plasmas, 2007. **14**(4): p. 042109.

192. Derzsi, A., et al., *Effects of fast atoms and energy-dependent secondary electron emission yields in PIC/MCC simulations of capacitively coupled plasmas.* Plasma Sources Science and Technology, 2015. **24**(3): p. 034002.
193. Phelps, A. and Z.L. Petrovic, *Cold-cathode discharges and breakdown in argon: surface and gas phase production of secondary electrons.* Plasma Sources Science and Technology, 1999. **8**(3): p. R21.
194. Sun, J.-Y., et al., *Realistic treatment for secondary electron emission in hybrid DC/DF capacitively coupled discharge.* Plasma Sources Science and Technology, 2020. **29**(2): p. 024001.
195. Daksha, M., et al., *The effect of realistic heavy particle induced secondary electron emission coefficients on the electron power absorption dynamics in single-and dual-frequency capacitively coupled plasmas.* Plasma Sources Science and Technology, 2017. **26**(8): p. 085006.
196. Li, Y. and D.B. Go, *Using field emission to control the electron energy distribution in high-pressure microdischarges at microscale dimensions.* Applied Physics Letters, 2013. **103**(23): p. 234104.
197. Brayfield, R.S., et al., *The impact of cathode surface roughness and multiple breakdown events on microscale gas breakdown at atmospheric pressure.* Journal of Applied Physics, 2019. **125**(20): p. 203302.
198. Ciampi, S., et al., *Harnessing electrostatic catalysis in single molecule, electrochemical and chemical systems: a rapidly growing experimental tool box.* Chemical Society Reviews, 2018. **47**(14): p. 5146-5164.
199. Shaik, S., et al., *Structure and reactivity/selectivity control by oriented-external electric fields.* Chemical Society Reviews, 2018. **47**(14): p. 5125-5145.
200. Liu, D.-X., et al., *Wall fluxes of reactive oxygen species of an rf atmospheric-pressure plasma and their dependence on sheath dynamics.* Journal of Physics D: Applied Physics, 2012. **45**(30): p. 305205.
201. Robertson, S., *Sheaths in laboratory and space plasmas.* Plasma Physics and Controlled Fusion, 2013. **55**(9): p. 093001.
202. Benilov, M., *The Child–Langmuir law and analytical theory of collisionless to collision-dominated sheaths.* Plasma Sources Science and Technology, 2008. **18**(1): p. 014005.
203. Grapperhaus, M.J. and M.J. Kushner, *A semianalytic radio frequency sheath model integrated into a two-dimensional hybrid model for plasma processing reactors.* Journal of applied physics, 1997. **81**(2): p. 569-577.
204. Li, H.-P. and X. Chen, *Three-dimensional modelling of a dc non-transferred arc plasma torch.* Journal of Physics D: Applied Physics, 2001. **34**(17): p. L99.
205. Hsu, K., K. Etemadi, and E. Pfender, *Study of the free-burning high-intensity argon arc.* Journal of applied physics, 1983. **54**(3): p. 1293-1301.
206. Freton, P., et al., *Magnetic field approaches in dc thermal plasma modelling.* Journal of Physics D: Applied Physics, 2011. **44**(34): p. 345202.
207. Li, H.-P., K.K. Ostrikov, and W. Sun, *The energy tree: Non-equilibrium energy transfer in collision-dominated plasmas.* Physics Reports, 2018. **770**: p. 1-45.
208. Sternberg, N. *Plasma-Sheath Revisited*. in *APS Annual Gaseous Electronics Meeting Abstracts*. 2012.
209. Sternberg, N. and V. Godyak, *Patching collisionless plasma and sheath solutions to approximate the plasma-wall problem.* IEEE transactions on plasma science, 2003. **31**(6): p. 1395-1401.
210. Sternberg, N. and V. Godyak, *On asymptotic matching and the sheath edge.* IEEE transactions on plasma science, 2003. **31**(4): p. 665-677.
211. Sternberg, N. and V. Godyak, *The Bohm plasma-sheath model and the Bohm criterion revisited.* IEEE transactions on plasma science, 2007. **35**(5): p. 1341-1349.

212. Riemann, K.-U., *Comments on" On asymptotic matching and the sheath Edge".* IEEE Transactions on Plasma Science, 2004. **32**(6): p. 2265-2270.
213. Sternberg, N. and V. Godyak, *Reply to comments on" On asymptotic matching and the sheath Edge".* IEEE Transactions on Plasma Science, 2004. **32**(6): p. 2271-2276.
214. Riemann, K., *Plasma and sheath.* Plasma Sources Science and Technology, 2008. **18**(1): p. 014006.
215. Riemann, K., et al., *The plasma–sheath matching problem.* Plasma physics and controlled fusion, 2005. **47**(11): p. 1949.
216. Riemann, K.-U., *Plasma-sheath transition in the kinetic Tonks-Langmuir model.* Physics of plasmas, 2006. **13**(6): p. 063508.
217. Charles, C., *A review of recent laboratory double layer experiments.* Plasma sources science and technology, 2007. **16**(4): p. R1.
218. George, S.M., *Atomic layer deposition: an overview.* Chemical reviews, 2010. **110**(1): p. 111-131.
219. Johnson, R.W., A. Hultqvist, and S.F. Bent, *A brief review of atomic layer deposition: from fundamentals to applications.* Materials today, 2014. **17**(5): p. 236-246.
220. Oehrlein, G., D. Metzler, and C. Li, *Atomic layer etching at the tipping point: an overview.* ECS Journal of Solid State Science and Technology, 2015. **4**(6): p. N5041.
221. Faraz, T., et al., *Atomic layer etching: what can we learn from atomic layer deposition?* ECS Journal of Solid State Science and Technology, 2015. **4**(6): p. N5023.
222. Shirafuji, T., H. Motomura, and K. Tachibana, *Fourier transform infrared phase-modulated ellipsometry for in situ diagnostics of plasma–surface interactions.* Journal of Physics D: Applied Physics, 2004. **37**(6): p. R49.
223. Bogaerts, A., et al., *The 2020 plasma catalysis roadmap.* Journal of Physics D: Applied Physics, 2020. **53**(44): p. 443001.
224. Darnon, M., *Plasma Etching in Microelectronics*, in *Plasma Etching Processes for CMOS Devices Realization*. 2017, Elsevier. p. 23-58.
225. Ishikawa, K., et al., *Rethinking surface reactions in nanoscale dry processes toward atomic precision and beyond: a physics and chemistry perspective.* Japanese Journal of Applied Physics, 2019. **58**(SE): p. SE0801.
226. Nojiri, K., *Dry etching technology for semiconductors*. 2015: Springer.
227. Kawamura, E., et al., *Ion energy distributions in rf sheaths; review, analysis and simulation.* Plasma Sources Science and Technology, 1999. **8**(3): p. R45.
228. Riemann, K., *Kinetic analysis of the collisional plasma–sheath transition.* Journal of Physics D: Applied Physics, 2003. **36**(22): p. 2811.
229. Zhang, D. and M.J. Kushner, *Investigations of surface reactions during C 2 F 6 plasma etching of SiO 2 with equipment and feature scale models.* Journal of Vacuum Science & Technology A: Vacuum, Surfaces, and Films, 2001. **19**(2): p. 524-538.
230. Müller, K., U. Weigmann, and H. Burghause, *Simulation of focused ion beam milling.* Microelectronic Engineering, 1986. **5**(1-4): p. 481-489.
231. Abrams, C.F. and D.B. Graves, *Energetic ion bombardment of SiO 2 surfaces: Molecular dynamics simulations.* Journal of Vacuum Science & Technology A: Vacuum, Surfaces, and Films, 1998. **16**(5): p. 3006-3019.
232. Smirnov, V., et al., *Molecular-dynamics model of energetic fluorocarbon-ion bombardment on SiO 2 I. Basic model and CF 2+-ion etch characterization.* Journal of applied physics, 2005. **97**(9): p. 093302.
233. Karahashi, K. and S. Hamaguchi, *Ion beam experiments for the study of plasma–surface interactions.* Journal of Physics D: Applied Physics, 2014. **47**(22): p. 224008.
234. Ventzek, P.L., et al., *Two-dimensional hybrid model of inductively coupled plasma sources for etching.* Applied physics letters, 1993. **63**(5): p. 605-607.

235. Hoekstra, R.J., *A model of energy and angular distributions of fluxes to the substrate and resulting surface topology for plasma etching systems*. 1998, University of Illinois at Urbana-Champaign.
236. Sankaran, A., *Surface reaction mechanisms for plasma processing of semiconductors*. 2003, University of Illinois at Urbana-Champaign.
237. Zhang, Y., et al., *Investigation of feature orientation and consequences of ion tilting during plasma etching with a three-dimensional feature profile simulator.* Journal of Vacuum Science & Technology A: Vacuum, Surfaces, and Films, 2017. **35**(2): p. 021303.
238. Schuengel, E., et al., *Ion distribution functions at the electrodes of capacitively coupled high-pressure hydrogen discharges.* Plasma Sources Science and Technology, 2013. **23**(1): p. 015001.
239. Zhang, Y., *Low Temperature Plasma Etching Control through Ion Energy Angular Distribution and 3-Dimensional Profile Simulation*. 2015, University of Michigan.
240. Coumou, D.J., et al., *Ion energy distribution skew control using phase-locked harmonic RF bias drive.* IEEE Transactions on Plasma Science, 2014. **42**(7): p. 1880-1893.
241. Georgieva, V., et al., *Understanding microwave surface-wave sustained plasmas at intermediate pressure by 2D modeling and experiments.* Plasma processes and polymers, 2017. **14**(4-5): p. 1600185.
242. Tinck, S. and A. Bogaerts, *Computational study of the CF4/CHF3/H2/Cl2/O2/HBr gas phase plasma chemistry.* Journal of Physics D: Applied Physics, 2016. **49**(19): p. 195203.
243. Choi, J.-G., D. Do, and H. Do, *Surface diffusion of adsorbed molecules in porous media: Monolayer, multilayer, and capillary condensation regimes.* Industrial & engineering chemistry research, 2001. **40**(19): p. 4005-4031.
244. Medveď, I. and R. Černý, *Surface diffusion in porous media: A critical review.* Microporous and Mesoporous Materials, 2011. **142**(2-3): p. 405-422.
245. Fu, E.S., et al., *The effective charge in surface electromigration.* Surface science, 1997. **385**(2-3): p. 259-269.
246. Barna, A., B. Pécz, and M. Menyhard, *TEM sample preparation by ion milling/amorphization.* Micron, 1999. **30**(3): p. 267-276.
247. Blauw, M., et al., *Kinetics and crystal orientation dependence in high aspect ratio silicon dry etching.* Journal of Vacuum Science & Technology B: Microelectronics and Nanometer Structures Processing, Measurement, and Phenomena, 2000. **18**(6): p. 3453-3461.
248. Harper, J., J. Cuomo, and H. Kaufman, *Technology and applications of broad-beam ion sources used in sputtering. Part II. Applications.* Journal of Vacuum Science and Technology, 1982. **21**(3): p. 737-756.
249. Tachi, S.i., K. Miyake, and T. Tokuyama, *Chemical and physical roles of individual reactive ions in Si dry etching.* Japanese Journal of Applied Physics, 1982. **21**(S1): p. 141.
250. Tachi, S.i. and S. Okudaira, *Chemical sputtering of silicon by F+, Cl+, and Br+ ions: reactive spot model for reactive ion etching.* Journal of Vacuum Science & Technology B: Microelectronics Processing and Phenomena, 1986. **4**(2): p. 459-467.
251. Cheng, E. and G.S. Hwang, *Dissociative chemisorption of methyl fluoride and its implications for atomic layer etching of silicon nitride.* Applied Surface Science, 2021. **543**: p. 148557.
252. Sridhar, S., P.L. Ventzek, and A. Ranjan, *Role of physisorption in atomic layer etching of silicon nitride.* Journal of Vacuum Science & Technology A: Vacuum, Surfaces, and Films, 2020. **38**(4): p. 043007.
253. Harafuji, K. and K. Kawamura, *Chemical Sputtering of GaN Crystal with a Chlorine-Adsorbed Layer.* Japanese Journal of Applied Physics, 2010. **49**(8S1): p. 08JE03.
254. Harafuji, K. and K. Kawamura, *Point defects induced by physical sputtering in wurtzite-type GaN crystal.* Japanese Journal of Applied Physics, 2010. **49**(1R): p. 011001.
255. Harafuji, K. and K. Kawamura, *Dry Etching Induced Damage in Wurtzite-Type GaN Crystal*, in *19th International Symposium on Plasma Chemistry*. 2009: Bochum.

256. Harafuji, K. and K. Kawamura, *Sputtering yield as a function of incident ion energy and angle in wurtzite-type GaN crystal.* Japanese journal of applied physics, 2008. **47**(3R): p. 1536.
257. Harafuji, K. and K. Kawamura, *Energy and angular dependence of incident Ar ion in dryetching of wurtzite-type GaN crystal*, in *28th International Conference on Phenomena in Ionized Gases*, J. Schmidt, et al., Editors. 2007, Institute of Plasma Physics AS CR: Prague, Czech Republic. p. 642-644.
258. Tinck, S., E.C. Neyts, and A. Bogaerts, *Fluorine–Silicon Surface Reactions during Cryogenic and Near Room Temperature Etching.* The Journal of Physical Chemistry C, 2014. **118**(51): p. 30315-30324.
259. Tinacba, E.J.C., et al., *Molecular dynamics simulation of Si and SiO2 reactive ion etching by fluorine-rich ion species.* Surface and Coatings Technology, 2019. **380**: p. 125032.
260. Ohta, H. and S. Hamaguchi, *Molecular dynamics simulation of silicon and silicon dioxide etching by energetic halogen beams.* Journal of Vacuum Science & Technology A: Vacuum, Surfaces, and Films, 2001. **19**(5): p. 2373-2381.
261. Dean, J.A. and N.A. Lange, *Table 4.11 Bond Dissociation Energies*, in *Lange's Handbook of Chemistry*. 1999, McGraw-Hill. p. 4.41-4.53.
262. Gray, D.C., V. Mohindra, and H.H. Sawin, *Redeposition kinetics in fluorocarbon plasma etching.* Journal of Vacuum Science & Technology A: Vacuum, Surfaces, and Films, 1994. **12**(2): p. 354-364.
263. Chevolleau, T., et al., *Etching of Si at low temperatures using a SF 6 reactive ion beam: effect of the ion energy and current density.* Journal of Vacuum Science & Technology A: Vacuum, Surfaces, and Films, 1997. **15**(5): p. 2661-2669.
264. Harper, J., et al., *Low energy ion beam etching.* Journal of the Electrochemical Society, 1981. **128**(5): p. 1077-1083.
265. Heath, B.A., *Selective reactive ion beam etching of SiO2 over polycrystalline Si.* Journal of the Electrochemical Society, 1982. **129**(2): p. 396-402.
266. Mayer, T., R. Barker, and L. Whitman, *Investigation of plasma etching mechanisms using beams of reactive gas ions.* Journal of Vacuum Science and Technology, 1981. **18**(2): p. 349-352.
267. Oostra, D., et al., *Near threshold sputtering of Si and SiO2 in a Cl2 environment.* Applied physics letters, 1987. **50**(21): p. 1506-1508.
268. Chinn, J., et al., *Ion beam etching of silicon, refractory metals, and refractory metal silicides using a chemistry assisted technique.* Journal of The Electrochemical Society, 1984. **131**(2): p. 375-380.
269. Balooch, M., et al., *Low-energy Ar ion-induced and chlorine ion etching of silicon.* Journal of Vacuum Science & Technology A: Vacuum, Surfaces, and Films, 1996. **14**(1): p. 229-233.
270. Chae, H., S.A. Vitale, and H.H. Sawin, *Silicon dioxide etching yield measurements with inductively coupled fluorocarbon plasmas.* Journal of Vacuum Science & Technology A: Vacuum, Surfaces, and Films, 2003. **21**(2): p. 381-387.
271. Guo, W. and H.H. Sawin, *Modeling of the angular dependence of plasma etching.* Journal of Vacuum Science & Technology A: Vacuum, Surfaces, and Films, 2009. **27**(6): p. 1326-1336.
272. Kolfschoten, A., *The role of noble gas ion bombardment in etching reactions.* Nuclear Instruments and Methods in Physics Research Section B: Beam Interactions with Materials and Atoms, 1987. **19**: p. 1001-1008.
273. Tokuyama, T., et al., *Low-energy mass-separated ion beam deposition of materials.* Nuclear Instruments and Methods, 1981. **182**: p. 241-250.
274. Karahashi, K., *Study of the Etching Reactions on SiO2 Caused by CFx＋(x＝1, 2, 3) Ion Irradiation.* 表面科学, 2007. **28**(2): p. 60-66.
275. Kawase, T. and S. Hamaguchi, *Molecular dynamics simulation analyses on injection angle dependence of SiO2 sputtering yields by fluorocarbon beams.* Thin Solid Films, 2007. **515**(12): p. 4883-4886.

276. Taguchi, M. and S. Hamaguchi, *MD simulations of amorphous SiO2 thin film formation in reactive sputtering deposition processes.* Thin Solid Films, 2007. **515**(12): p. 4879-4882.
277. Taguchi, M. and S. Hamaguchi, *Molecular dynamics study on Ar ion bombardment effects in amorphous Si O 2 deposition processes.* Journal of applied physics, 2006. **100**(12): p. 123305.
278. Gogolides, E., et al., *Etching of SiO 2 and Si in fluorocarbon plasmas: A detailed surface model accounting for etching and deposition.* Journal of Applied Physics, 2000. **88**(10): p. 5570-5584.
279. Karahashi, K., et al., *Etching yield of SiO 2 irradiated by F+, CF x+(x= 1, 2, 3) ion with energies from 250 to 2000 eV.* Journal of Vacuum Science & Technology A: Vacuum, Surfaces, and Films, 2004. **22**(4): p. 1166-1168.
280. Shibano, T., et al., *Etching yields of SiO2 by low energy CF x+ and F+ ions.* Applied physics letters, 1993. **63**(17): p. 2336-2338.
281. Hamaguchi, S. and H. Ohta, *Surface molecular dynamics of Si/SiO2 reactive ion etching.* Vacuum, 2002. **66**(3-4): p. 189-195.
282. Yanai, K.-i., et al., *Mass-analyzed CF x+(x= 1, 2, 3) ion beam study on selectivity of Si O 2-to-SiN etching and a-C: F film deposition.* Journal of applied physics, 2005. **97**(5): p. 053302.
283. Kaler, S.S., et al., *Atomic layer etching of silicon dioxide using alternating C4F8 and energetic Ar+ plasma beams.* Journal of Physics D: Applied Physics, 2017. **50**(23): p. 234001.
284. Huard, C.M., et al., *Transient behavior in quasi-atomic layer etching of silicon dioxide and silicon nitride in fluorocarbon plasmas.* Journal of Vacuum Science & Technology A: Vacuum, Surfaces, and Films, 2018. **36**(6): p. 06B101.
285. Gasvoda, R.J., et al., *Surface phenomena during plasma-assisted atomic layer etching of SiO2.* ACS applied materials & interfaces, 2017. **9**(36): p. 31067-31075.
286. Harafuji, K. and K. Kawamura, *Molecular Dynamics of Sputtering Yield as a Function of Ion Incident Angle in Chlorine-Adsorbed GaN Crystal*, in *21st International Symposium on Plasma Chemistry*. 2013.
287. Harafuji, K. and K. Kawamura, *Molecular Dynamics of Ion Incident Angle Dependence of Sputtering Yield in Chlorine-Adsorbed GaN Crystal.* Japanese Journal of Applied Physics, 2011. **50**(8S1): p. 08JG03.
288. Harafuji, K. and K. Kawamura, *Molecular Dynamics of Sputtering Yield as a Function of Ion Incident Angle in GaN Crystal*, in *20th International Symposium on Plasma Chemistry*. 2011. p. 4.
289. Hamblen, D.P. and A. Cha-Lin, *Angular etching correlations from RIE: application to VLSI fabrication and process modeling.* Journal of the Electrochemical Society, 1988. **135**(7): p. 1816.
290. Cho, B.-O., et al., *More vertical etch profile using a Faraday cage in plasma etching.* Review of scientific instruments, 1999. **70**(5): p. 2458-2461.
291. Abraham-Shrauner, B. and N. Jagannathan, *Modification of plasma-etched profiles by sputtering.* IEEE transactions on plasma science, 1999. **27**(3): p. 668-675.
292. Park, C.H., et al. *Etching of poly-Si with atomic scale accuracy in inductively coupled Ar and He plasmas*. in *2006 8th International Conference on Solid-State and Integrated Circuit Technology Proceedings*. 2006. IEEE.
293. Dai, Z.-L., S.-Q. Zhang, and Y.-N. Wang, *Study on feature profile evolution for chlorine etching of silicon in an RF biased sheath.* Vacuum, 2013. **89**: p. 197-202.
294. Chang, J.P., et al., *Kinetic study of low energy argon ion-enhanced plasma etching of polysilicon with atomic/molecular chlorine.* Journal of Vacuum Science & Technology A: Vacuum, Surfaces, and Films, 1997. **15**(4): p. 1853-1863.
295. Kim, J.-H., J.-S. Park, and C.-K. Kim, *Angular dependence of SiO2 etching in plasmas containing heptafluoropropyl methyl ether.* Thin Solid Films, 2019. **669**: p. 262-268.

296. Levinson, J.A., et al., *Ion-assisted etching and profile development of silicon in molecular and atomic chlorine.* Journal of Vacuum Science & Technology B: Microelectronics and Nanometer Structures Processing, Measurement, and Phenomena, 2000. **18**(1): p. 172-190.
297. Chang, J. and J. Coburn, *Plasma–surface interactions.* Journal of Vacuum Science & Technology A: Vacuum, Surfaces, and Films, 2003. **21**(5): p. S145-S151.
298. Kim, J.-H. and C.-K. Kim, *Mechanism for Plasma Etching of SiO2 Using Low Global Warming Potential Materials.* International Journal of Chemistry and Chemical Engineering Systems, 2019. **4**.
299. Lee, G.-R., et al., *Characteristics of secondary etching of SiO 2 by ions reflected from a primary SiO 2 target in a CHF 3 plasma.* Journal of Vacuum Science & Technology A: Vacuum, Surfaces, and Films, 2003. **21**(2): p. 404-410.
300. Kim, J.-H., et al., *Angular dependences of SiO2 etch rates at different bias voltages in CF4, C2F6, and C4F8 plasmas.* Thin Solid Films, 2017. **637**: p. 43-48.
301. Cho, B.-O., et al., *Angular dependence of the redeposition rates during SiO 2 etching in a CF 4 plasma.* Journal of Vacuum Science & Technology A: Vacuum, Surfaces, and Films, 2001. **19**(3): p. 730-735.
302. Cho, B.-O., et al., *Angular dependence of SiO 2 etching in a fluorocarbon plasma.* Journal of Vacuum Science & Technology A: Vacuum, Surfaces, and Films, 2000. **18**(6): p. 2791-2798.
303. Lee, G.-R., et al., *Dependence of Si O 2 etch rate on sidewall angle as affected by bottom materials in a high-density CHF 3 plasma.* Journal of Vacuum Science & Technology B: Microelectronics and Nanometer Structures Processing, Measurement, and Phenomena, 2006. **24**(1): p. 298-303.
304. Lee, G.-R., et al., *Angular dependence of SiO 2 etch rate at various bias voltages in a high density CHF 3 plasma.* Journal of Vacuum Science & Technology A: Vacuum, Surfaces, and Films, 2002. **20**(5): p. 1808-1814.
305. Kurihara, K., *Measurements of SiO2, Polycrystalline Silicon, and Si3N4 Etching Yields Depending on Ion Incident Angle.* Japanese Journal of Applied Physics, 2011. **50**(12R): p. 120206.
306. Huang, S., et al., *Plasma etching of high aspect ratio features in SiO2 using Ar/C4F8/O2 mixtures: A computational investigation.* Journal of Vacuum Science & Technology A: Vacuum, Surfaces, and Films, 2019. **37**(3): p. 031304.
307. Sankaran, A. and M.J. Kushner, *Integrated feature scale modeling of plasma processing of porous and solid SiO 2. I. Fluorocarbon etching.* Journal of Vacuum Science & Technology A: Vacuum, Surfaces, and Films, 2004. **22**(4): p. 1242-1259.